ISAS - INTERNATIONAL SCHOOL
FOR ADVANCED STUDIES

A STUDY OF PHYSICAL PROPERTIES OF IONIC SYSTEMS

ATTESTATO DI RICERCA

"DOCTOR PHILOSOPHIAE"

CANDIDATO:

Eduardo Roman

RELATORE:

Prof. M. Tosi

Anno Accademico 1982/83   **TRIESTE**

A STUDY OF PHYSICAL PROPERTIES OF IONIC SYSTEMS

(Surface energy of ionic crystals and states of extra electrons in molten salts)

Thesis submitted for the degree of "Doctor Philosophiae" at
the International School for Advanced Studies, Trieste,Italy

To my parents

ACKNOWLEDGMENTS

Appendices.

Bibliography.

INTRODUCTION

The present work is concerned with a study of two particular problems in the theory of ionic systems : the surface energy of ionic crystals and the states of extra electrons in molten alkali halides . The basic knowledge on ionic systems , for the crystalline and liquid phases ,which is relevant to these problems is summarized in Chapter I .

Surface energies of ionic crystals are known experimentally for relatively few ionic materials [54,55,56] . The difficulties of experimental determinations [54] involve a number of uncertainties in the measured values . Theoretical estimations of the surface energy of ionic crystals , involving full lattice calculations [2,55] through the use of semiempirical models for the interionic potentials [1] , have on the whole failed to clarify this important problem .

In this context , relations between surface and bulk properties of materials are useful in surface physics and acquire deeper content when they are seen to apply to classes of materials even with different types of cohesive forces . In this spirit a "universal" model has been proposed for the surface energy of solids [63] , that has been succesfully tested against experiment for a number of metals ranging from the alkali metals to transition metals such as niobium and tantalum . The same approach has been used [73] to relate the surface tension of electron-hole drops in semiconductors to their bulk properties . In this "universal model" [63] the surface energy is regarded as the work done in reversibly cleaving the crystal along a crystallographic plane , and a scaling hypothesis is introduced to construct the cleavage force from its limiting values for small

and large relative displacements of the two crystal halves .

In the present work , this simple approach is examined for ionic crystals in the families of the alkali halides and alkaline-earth fluorides and oxides . A rather drastically different physical model is clearly involved for these materials as opposed to metals since (1) optic as well as acoustic phonons enter the problem and (2) the van der Waals interactions arise from closed electron shells . A similar universal relation , as that found for metals , is obtained for ionic crystals [65] in which the surface energy is given in terms of the elastic constants , the electronic dielectric constant, the optical band gap and the interplanar spacing .

Solutions of alkali metals and molten alkali halides show a number of physical properties which are in general characterized by a continuous variation with concentration . The determination of the phase diagrams for these systems [74] shows that the liquid metal (M) and the molten salt (MX) are miscible in all proportions above a certain critical temperature . Measurements of the electrical conductance in K-K halide and Na-Na halide melts [74] give evidence for the presence of electronic transport superimposed on ionic conduction . Near the salt-rich side of the phase diagram , broad absorption bands have been found in optical studies of metal-molten salt solutions [82-90] . Measurements have been made of the electron spin resonance [91] , magnetic susceptibility [91-93,108] , metal partial vapor pressure [94] and freezing point depression [95] . The magnetic susceptibility studies [92,93,108] indicate that the molar electron susceptibility of M-MX solutions is paramagnetic and rapidly decreasing with increasing metal concentration .

These solutions have recently received increasing experimental attention . At low metal concentration , in particular , attention has focused

on the properties of excess electrons in the molten salt and on their evolution with increasing concentration towards the nonmetal-to-metal transition . It has been known for a long time from the optical absorption studies [85,87,100] that the excess electrons at high dilution become localized in traps inside the liquid structure . Localization is believed to involve solvation of the electron by alkali ions in the molten salt , the nearest analogue in the crystal being [104] the formation of F centers by trapping of electrons into anion vacancies in additively coloured or irradiated alkali halide crystals [22,24] . In order to avoid discussing molten salt structure in terms of point defects , one may visualize instead favourable fluctuations of the Madelung potential and cooperative rearrengements of the mobile ions as leading to electron trapping in the liquid . The recent experimental work on optical absorption in liquid CsCl at various concentrations of excess electrons in a high dilution range [109] , has provided further support to this picture and added considerable detail to it . Relevant evidence for electron localization due to the surrounding positive ions has also been obtained in NMR studies on Cs-CsI [115,116] and Cs-CsCl [116] solutions . It is found that the solvated electrons , at low metal concentration (less than 5% excess metal) , are localized for times on the order of the ionic diffusion times ($\sim 10^{-12}$ sec) . The further addition of metal leads , however , to rapid delocalization . In this respect , interesting observations indicative of aggregation phenomena between solvated electrons , have also been reported [109,110,112] with increasing concentration . Further relevant evidence has been provided by ESR and magnetic susceptibility studies [120,121] .

The solvation process at high dilution has been treated theoretically in a model , hereafter referred to as I , schematizing an excess electron as bound to a bubble inside a liquid of charged hard spheres [122] .

This model , though crude , allows a selfconsistent determination of the electronic ground state and of the surrounding liquid structure , self-consistency being of crucial importance in allowing the electron to dig its own trap in a favourable local arrangement of alkali and halogen ions. A bound state was found in molten KCl by treating the electron-ion interactions in a polarizable-point-ion approximation . Contact with optical absorption data could then be established by treating the transition to the 2p excited state as a Franck-Condon process and by allowing for liquid-state fluctuations in the ground state .

The present work is concerned with the high dilution limit of excess electrons in a molten salt . The main aim of this study is to confront the same basic model I with the newly available experimental results . A critique of model I is presented which suggests an empirical modification aimed at weakening the role of Coulombic interactions and loosening the local structure [126] . Results for various properties of electronic states in the equilibrium potential well are reported , contact with experimental data being made for ground state properties . The main test of the model is still the calculation of optical absorption by the solvated electron , and is extended to (a) systems other than KCl and (b) transitions to higher excited states . Ionic relaxation in the excited states and lifetime of the bound state are also discussed . A calculation of the perturbation of the fundamental absorption of the molten salt induced by the solvated electron is performed in connection with a near-ultraviolet absorption band observed in electrolytically injected samples [109] . Finally , some concluding remarks are given at the end of Chapter III .

CHAPTER I

IONIC SYSTEMS IN THE CRYSTALLINE AND LIQUID PHASES

The aim of this chapter is to give an introductory survey of solid and liquid ionic systems, introducing a series of facts that will be needed in later chapters.

Section 1 is dedicated to the description of the Born model of ionic materials, in order to establish the different interactions between the ions in the system. The importance of the repulsive and van der Waals interaction in connection with the surface energy problem, to be treated in Chapter II, is stressed. To this end, Section 2 points out the role of the elastic constants in this problem. Section 3 is dedicated to defects in ionic crystals, in particular to the F – center problem, and constitutes an introduction to the subject treated in Chapter III.

Section 4 introduces the main feature of the ionic systems at the melting point, regarding the structural and electronic properties of the liquid phase. These concepts and the study of the liquid structure in Section 5 constitute the basic tools in building up the theory of Chapter III.

I.1 Born model of ionic materials and cohesion of ionic crystals

A real ionic crystal can be well described by the Born model of ionic materials [1,2] . Apart from the calculation of the cohesive energy, for which the model was initially proposed, a variety of physical properties of ionic crystals have been studied within this theory.

The fundamental assumption of Born's model is that the crystals under consideration are built up of positive and negative ions. These ions are considered to bear net charges determined by chemical valence and are regarded as essentially spherical and non overlapping. These theoretical considerations are consistent with the results of x-ray diffraction measurements for the electronic charge distribution in ionic crystals [3] . A plot of the electron density and a map showing lines of constant density around the ions of a NaCl crystal are shown in Fig. (I.1-1). A numerical integration of the electronic density around each ion in Fig. (I.1-1) gives a total electronic charge of $+e$ around the sodium and $-0.7e$ around the chlorine. Notice also, from Fig. (I.1-1), that a minimum in the electron density occurs at a distance of $1.17 \, \text{Å}$ from the Na^+ and $1.64 \, \text{Å}$ from the Cl^- ion. These distances are taken as the crystal radii of the ions. This assignment is only approximate because, in fact, the ions are not spheres in the solid but are somewhat distorted according to cubic symmetry.

On the other hand, this determination of the crystal radii is less justified in cases of a not negligible overlap between the ions, e.g. in LiF.

The assumption of spherical ions implies that the interactions between them are given by central forces operating between pairs of ions.
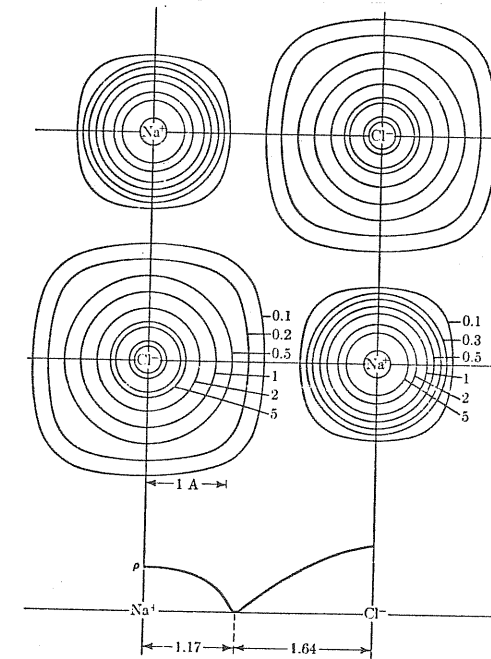
FIGURE I.1-1:   Electron density in the (100) plane of a NaCl crystal as determined by x-ray scattering experiments. The numbers represent the electron density per cubic angstrom. From ref. [3] .

The sum over all the ions, taken to be at rest in their average positions in the crystal, of these pairwise interactions gives rise to the so called

lattice energy. The main contribution to the lattice energy comes from the electrostatic interactions of these point-charge like ions, which give rise to a net binding (Madelung energy). The Coulomb force, in fact, induces the charge alternation shown in Fig. (I.1-1). Preventing the collapse of the crystal structure under the Coulomb attraction, there are short-range repulsive forces which oppose the interpenetration of the ions. These repulsive interactions decrease the binding energy by an amount of typically about 10%. The other binding contribution to the lattice energy comes from the van der Waals interactions which are of the order of a few percent of the total lattice energy. In Table (I.1-1) are given the values of the lattice energy for some alkali halides, together with the partial contributions to it due to the Coulomb, repulsive and van der Waals interactions.

	LiF	NaCl	CsI
Coulomb	-12.49	-8.92	-6.36
Repulsive	1.99	1.17	0.61
van der Waals	-0.03	-0.05	-0.17
Total lattice energy	-10.53	-7.80	-5.92
Experimental	-10.70	-8.08	-6.33

Table I.1-1:   Lattice energy values for some alkali halides. The partial contributions to the lattice energy due to the Coulomb, repulsive and van der Waals interactions are displayed. All values are in ev. From ref. [2] .

(a)   Born theory of the lattice energy

The evaluation of the Madelung energy (i.e. the total electro= static potential energy per molecule in the crystal) cannot be done in an elementary way due to the slow decay of the Coulomb interaction. To evaluate the lattice sums, very accurate and rapidly convergent methods have been developed [4,5] . The Madelung energy is commonly written as

$$E_m = - (ze)^2 \frac{\alpha_R}{R} , \qquad (I.1-1)$$

where z is the largest common factor of the ionic valences ($z = 1$ for the alkali halides), R is a characteristic length of the crystal structure (e.g. the nearest neighbor distance) and α_R is the Madelung constant referred to the length R . The values of the Madelung constant for some ionic crystal structures are given in Table (I.1-2).

	NaCl	CsCl	Zincblende	CaF$_2$	CuO
α_a	3.49513	2.03536	3.78293	11.63657	10.25946
α_R	1.75756	1.76267	1.63805	5.03878	4.44248

Table I.1-2:   Madelung constants for some ionic crystal structures. The constants

α_R and α_a are referred to the nearest neighbor distance R_0 and to the lattice parameter a. From ref. [2].

The short range repulsive forces have a quantum mechanical origin and no simple expression for them, as for the Coulomb interaction, follows from theoretical considerations. The Born model makes recourse to certain simple representations of the repulsive interaction, which involve the use of two unknown parameters to be fitted to crystal data. A simple representation for this interaction is given by the following form,

$$ E_{REP} = \frac{A}{R^n} . \qquad (I.1-2) $$

At the simplest level of approximation the lattice energy E_L is given by the sum of Eq. (I.1-1) and Eq. (I.1-2). The determination of the parameters A and n in the latter is done by noticing that $dE_L / dR \big|_{R = R_0} = 0$ (at zero pressure, where R_0 is the equilibrium lattice spacing), and by using the value of the isothermal compressibility K given by

$$ K^{-1} = \aleph_0 \; d^2 E_L / d\sigma^2 \big|_{R = R_0} \qquad \text{where} \quad \aleph_0 $$

is the volume per molecule. The final expression for $E_L(R)$ reads as follows,

$$ E_L(R) = - (ze)^2 \frac{\alpha_R}{R} \left[1 - \frac{1}{n} \left(\frac{R_0}{R} \right)^{n-1} \right] \qquad (I.1-3) $$

Here,

$$ n = 1 + \frac{9 \aleph_0 R_0}{(ze)^2 \, \alpha_R} K^{-1} . \qquad (I.1-4) $$

We can immediately conclude from Eq. (I.1-3) that the repulsive interactions contribute to $E_L(R_0)$ only $\Theta(1/n)$ compared with the Coulomb interactions. The calculated values of n ($\sim 8 - 10$) for some ionic crystals shown in Table (I.1-3) are consistent with the values of the repulsive terms given in Table (I.1-1).

	LiF	NaCl	CsI
n	6	8	14

Table I.1-3: Born repulsive exponent n for some alkali halides. Data from ref. [2] with n given by Eq. (I.1-4).

A second important conclusion refers to the compressibility. Because

the second derivative $d^2 E_L / d\varpi^2$ is involved
in the determination of the compressibility, it follows that the main
contribution to it comes from the repulsive term, which is now
$\Theta\left(\frac{1}{2}(m+1)\right)$ compared with the Coulomb part. It can also
be shown (see section (I.2)) that the elastic constants
$(C_{11}, C_{12}$ and $C_{44})$ are essentially determined by the
repulsive interactions (note also that $K^{-1} \propto C_{11} + 2 C_{12}$).
The elastic constants are in turn important in the problem of the
surface energy of ionic crystals as we shall see in Chapter II.

(b)   Born-Mayer exponential terms and ionic radii

The expression for the repulsive term given in Eq. (I.1-2)
can be refined by describing the repulsive interactions through the
Born-Mayer exponential form as follows,

$$E_{REP} = B \, e^{-R/\rho} . \qquad (I.1-5)$$

Here B and ρ are the strength and hardness parameters, respecti=
vely. Eq. (I.1-5) is suggested by quantum-mechanical overlap arguments
and allows for important considerations regarding the ionic radii in

the crystal. The approximate constancy displayed by the differences
in nearest-neighbor distance in the various halides of the two
corresponding alkalis, shown in Table (1.1-4), suggests that one can
associate a crystal radius to each ion in the solid. From Table (I.1-
4) we can interpret the observed differences in nearest-neighbor
distance as differences between the crystal radii of K^+ and Na^+
i.e., $R(K^+) - R(Na^+) \approx 0.32$ Å .

	F	Cl	Br	I
Na				
	0.357	0.327	0.309	0.296
K				

Table I.1-4:   Differences in nearest-neighbor distance in the various halides of the
two alkalis,   Na   and   K . Data from ref. [2] . All values are in Å .

A systematic determination of the crystal radii can be performed
using the Born-Mayer exponential form written explicitly in terms of the
ionic radii (basic radii), which are constant within the whole family of
salts, to be fitted by a least-squares procedure [6] . For nearest-
neighbor interactions only, Eq. (I.1-5) can be rewritten as follows,

$$E_{REP} = M b \, \exp\left[(r_+ + r_- - R)/\rho\right], \qquad (I.1-6)$$

where M is the number of first neighbors and $r_{\pm}$ are the basic radii. The nearest neighbor distance R_o can now be written as follows: $R_o = r_+ + r_- + \Delta$ where Δ is found to vary slightly from crystal to crystal. The crystal radii $R_{\pm}$ are defined such that $R_o = R_+ + R_-$, by splitting Δ in equal parts between the two ions. The values for the crystal radii obtained in this way are given in Table (I.1-5).

In the surface energy problem, on the other hand, the repulsive interaction plays a relatively more important role than it does in the determination of the lattice energy. Surface energy calculations [7] based on Eq. (I.1-6) show, in fact, that the electrostatic term is only about (30-40) % larger (in absolute value) than the repulsive term. In this context, the inclusion of the van der Waals interaction is essential in accounting for the surface energy of an ionic crystal.

	Li		Na		K		Rb		Cs	
F	1.19	0.83	1.16	1.15	1.19	1.48	1.20	1.61	1.23	1.77
Cl	1.67	0.90	1.62	1.20	1.63	1.51	1.64	1.65	1.67	1.80
Br	1.83	0.93	1.77	1.22	1.78	1.52	1.79	1.66	1.81	1.81
I	2.05	0.95	1.99	1.25	1.99	1.54	2.00	1.68	2.01	1.82

Table I.1-5: Crystal radii for alkali and halogen ions in the NaCl – type alkali

halides. Data from ref. [6] . All values are in Å . For each alkali halide the number to the right gives the radius of the halogen ion and the number to the left gives the radius of the alkali ion.

(c)   van der Waals interaction

The van der Waals interaction is responsible for the cohesion in the liquid and solid phases of rare gases. This attractive interaction between closed-shell atoms has its origin in the correlations of the electronic motions in different atoms. The van der Waals forces are present also between ions with rare gas electron configuration, e.g. the alkali and halogen ions. A classical explanation of this interaction is possible, by noting that the instantaneous dipole moment μ of a closed-shell atom induces on a similar atom at a distance r a dipole moment $\alpha \mu / r^3$ (α is the atomic polarizability), and reciprocally a field of the order of $\alpha \mu / r^6$ is produced on the first atom. The resulting value for the interaction energy is thus proportional to $-\alpha \bar{\mu}^2 / r^6$ ($\bar{\mu}^2$ is the mean square dipole moment of the first atom). Higher moments of the charge distribution of the atoms yield the dipole-quadrupole term ($\sim 1 / r^8$), the quadrupole-quadrupole term ($\sim 1 / r^{10}$), etc.

A quantum-mechanical calculation of the van der Waals interaction

is usually performed by perturbation theory. In the second order of perturbation theory, the dipole-dipole interaction energy of two atoms (or ions), can be written as follows,

$$\emptyset_{ij}(R) = - \frac{C_{ij}}{R_{ij}^6} \, ,$$
(I.1-7)

where C_{ij} are the van der Waals coefficients for the dipole-dipole interaction energy between the atoms i and j. An approxi= mate formula for C_{ij} [8] reads

$$C_{ij} = \frac{3}{2} \alpha_i \alpha_j \frac{E_i E_j}{E_i + E_j} \, ,$$
(I.1-8)

where α_i are the electronic polarizabilities of the atoms and E_i are average excitation energies of the atoms.

Values of the dipole-dipole coefficient C_{ij} for different ions in some ionic crystals are displayed in Table (I.1-6).

The contribution of the van der Waals interaction to the lattice energy can be calculated from Eq. (I.1-7) by performing the corresponding lattice sums. The resulting expression can be written as $E_{vw} = -C/R^6$. Analogous terms follow from the higher order interactions. While the value E_{vw} is only about a few percent of the total lattice energy, the corresponding contribution to the surface energy increases to about a 40% of the total value. In Table (I.1-7) are given the calculated values

of the specific energy of the (100) face for some alkali halide crystals. The table clearly shows that the repulsive and van der Waals contributions to the surface energy are relatively more important than the corresponding contributions to the lattice energy; this is because the surface energy represents the energy necessary to divide a crystal into neutral parts, while the lattice energy is the energy required to divide it into oppositely charged ions.

Salt	C++	C--	C+-
LiF	0.073	14.5	8
NaCl	1.68	116	14.2
KCl	24.3	124.5	48
KBr	24.3	206	60
KI	24.3	403	82
MgO	0.7	30	2.9
CaF$_2$	44.23	9.51	18.06
BaF$_2$	188.6	9.51	40.12

Table I.1-6: van der Waals dipole-dipole coefficients for some ionic crystals. All values are in 10^{-60} erg $\times$ cm^6 . Data for the alkali halides are from [9] . Data for MgO from [10] . Data for the fluorite-type from [11] .

In Chapter II we shall develop a simple model for the surface

energy of an ionic crystal in which the van der Waals interaction between ions is taken as in Eq. (I.1-7).

So far we have described how to calculate the lattice energy within the Born model. Then, the cohesive energy of an ionic crystal, at $T = 0\,^\circ K$, can be calculated by adding the zero point vibration energy.

	LiF	NaCl	KCl
Coulomb	921.1	335.5	241.4
Repulsive	-687.4	-200.2	-137.6
van der Waals	128.8	78.3	67.2
Total	363	214	171.
Experiment	340	276-300	252 - 110

Table I.1-7:   Specific energy of the (100) face of some alkali halide crystals. All values are in erg/cm^2 . Data from ref. [2] .

I.2   Lattice vibrations in ionic crystals

The interaction energy between the ions in a crystal is described in a simple way by the Born model. In a preliminary qualitative analysis we can write the potential $\emptyset$ between the ions as follows,

$$\emptyset_{++} = \emptyset_{--} = \frac{e^2}{R} \qquad (I.2-1)$$

and

$$\emptyset_{+-} = -\frac{e^2}{R} + \frac{1}{M}\,\frac{A}{R^n} , \qquad (I.2-2)$$

where M is the number of nearest neighbors and A is given in Eq. (I.1-2). A schematic picture of the potential $\emptyset_{+-}$ is shown in Fig. (I.2-1).

In the crystal, the ions oscillate around the equilibrium distance R_0 , and for sufficiently small departures ΔR from their equilibrium positions, an effective potential $U_{eff} \propto \Delta R^2$ is found to be appropriate in the description of the lattice vibrations. This constitutes the harmonic approximation which we shall follow in this section.

The lattice vibrations are characterized by their dispersion curves, a typical example being shown in Fig. (I.2-2) for KBr.
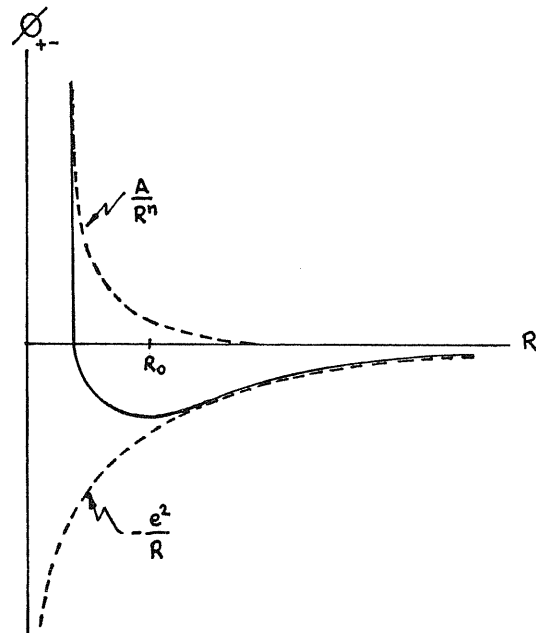
Fig. I.2-1:   Schematic representation of the potential energy of two oppositely charged
ions.

Fig. I.2-2:   Phonon dispersion curves of   KBr   determined experimentally by inelastic

neutron scattering   [12]   , and their fit by a rigid-ion model and a polarizable-ion

model.

Superposed to the experimental points in the figure, the calculated curves

within the rigid-ion model (Born model) and the shell-model (including

electronic polarizabilities of the ions) are also shown. Considering the

simplicity of the Born model, the agreement is surprisingly good although

the longitudinal modes are generally too high, particularly for the optic

branches. A major effect of the Coulomb forces is the splitting between

$\nu_{LO}(0)$ and $\nu_{TO}(0)$, which satisfy the Lyddane-Sachs-Teller relation: $\nu_{LO}^2(0) / \nu_{TO}^2(0) = \varepsilon_0 / \varepsilon_\infty$ where ε_0 , ε_∞ are the static and high frequency dielectric constants, respectively. From Fig. (I.2-2) we find: $\nu_{LO}^2(0) / \nu_{TO}^2(0) \simeq 2.04$ while from ref. [17] we obtain $\varepsilon_0 / \varepsilon_\infty = 2.08$ in good agreement.

(a)   The Hamiltonian of the crystal and the dynamical matrix

The equation of motion of the ions in the crystal can be derived from the corresponding Hamilton function. Within the harmonic approximation, the potential energy of the crystal is written as a quadratic form in the ionic displacements from the equilibrium positions (plus a constant term which is just the static potential energy of the crystal, i.e. the lattice energy). The Hamiltonian $\mathcal{H}$ can be written as follows,

$$\mathcal{H} = \frac{1}{2} \sum_{\ell,j} m_j \sum_\alpha \dot{u}_\alpha^2(\ell,j) + \frac{1}{2} \sum_{\ell,j} \sum_{\ell',j'} \sum_{\alpha,\beta} V_{\alpha\beta}\binom{\ell\ell'}{jj'} u_\alpha(\ell,j) u_\beta(\ell',j'), \qquad (I.2-2)$$

where ℓ denotes the ℓth unit cell and j denotes the jth ion within the unit cell. In Eq. (I.2-2), the first term represents the total kinetic energy of the crystal, where m_j is the mass of the jth ion in the ℓth unit cell, and $\dot{u}_\alpha(\ell,j)$, $u_\alpha(\ell,j)$ are the velocity

and the displacement of the ion along the direction α . The coefficients $V_{\alpha\beta}\binom{\ell\ell'}{jj'}$ in Eq. (I.2-2) are the ionic force constants which can be derived from the expression of the potential between the ions (e.g. from Eq. I.2-1). If we call V the total potential energy of the crystal, the quantities $V_{\alpha\beta}$ are defined by,
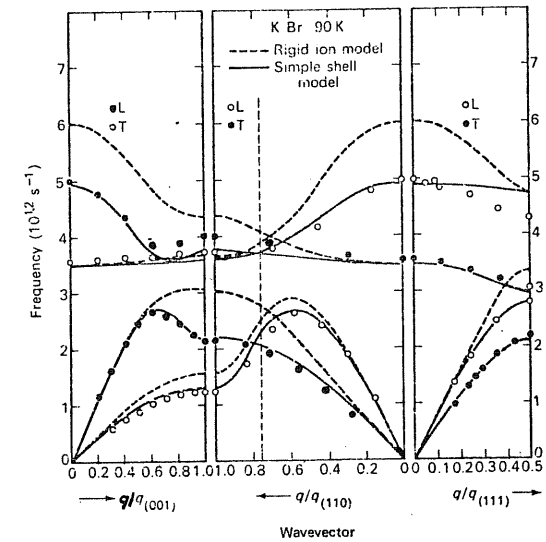
$$V_{\alpha\beta}\binom{\ell \ell'}{j j'} = \left. \frac{\partial^2 V}{\partial u_\alpha(\ell,j) \, \partial u_\beta(\ell',j')} \right|_0 . \qquad (I.2-3)$$

From this definition immediately follows that: $V_{\alpha\beta}\binom{\ell\ell'}{jj'} = V_{\beta\alpha}\binom{\ell'\ell}{j'j}$. For the particular case of radial interactions, the force constants $V_{\alpha\beta}$ can be obtained from the potential $\phi(R)$ between ions as follows [16] ,

$$V_{\alpha\beta}\binom{\ell\ell'}{jj'} = -F(R) R_\alpha R_\beta - \delta_{\alpha\beta} G(R) ,$$

where R is the distance between the ions at the equilibrium positions $\underset{\sim}{R}(\ell,j)$ and $\underset{\sim}{R}(\ell',j')$, respectively; $F(R) = \frac{1}{R}\left(\phi'' - \frac{1}{R}\phi'\right)$ and $G(R) = \frac{1}{R}\phi'$; $\phi' = d\phi/dR$, $\phi'' = d^2\phi/dR^2$.

The equation of motion of the ions in the crystal can be obtained directly from Eq. (I.2-2); there, assuming a plane wave solution of frequency ω and wavevector $\bar{q}$ for the ionic displacements, the resulting system of the equation is found:

$$\sum_{\beta,j'} \left[D_{\alpha\beta} \left(\begin{smallmatrix} \bar{q} \\ jj' \end{smallmatrix} \right) - m_j \, \omega^2 \, \delta_{jj'} \, \delta_{\alpha\beta} \right] A_{\beta j'} = 0, \qquad (I.2-4)$$

where $D_{\alpha\beta}(\bar{q})$ is the dynamical matrix and $\bar{A}_j$ is the amplitude of the $j^{\underline{th}}$ ion in the reference unit cell for the corresponding phonom mode. The expression of the dynamical matrix is

$$D_{\alpha\beta} \left(\begin{smallmatrix} \bar{q} \\ jj' \end{smallmatrix} \right) = \sum_{\ell'} V_{\alpha\beta} \left(\begin{smallmatrix} 0 & \ell' \\ j & j' \end{smallmatrix} \right) e^{-i\,\bar{q}\cdot\left[\bar{R}(\ell',j') - \bar{R}(0,j) \right]}, \qquad (I.2-5)$$

The $D_{\alpha\beta}$ is a $3S \times 3S$ matrix, where S is the number of ions in the unit cell. Finally, the phonom dispersion relations are obtained by solving the determinantal equation

$$\left[D_{\alpha\beta} \left(\begin{smallmatrix} \bar{q} \\ jj' \end{smallmatrix} \right) - m_j \, \omega^2 \, \delta_{jj'} \, \delta_{\alpha\beta} \right] = 0. \qquad (I.2-6)$$

Here, the $3S$ roots give the $3S$ frequencies $\omega_m(\bar{q})$ $(n = 1, 2, \dots 3S)$ of which there are the acoustic modes (one longitudinal (L) and two transverse (T) modes if $\bar{q}$ is along high-symmetry directions).

(b)   The acoustic modes and the elastic constants

For the case of the acoustic modes in the long wavelength limit, the ions in a unit cell move in phase. These low frequency vibrations correspond to sound waves, and satisfy a linear relation given by $\omega = \sigma q$ where σ is the corresponding sound velocity. The sound velocity is determined by the elastic constants ; these are commonly indicated by C_{11}, C_{12} and C_{44} for a cubic crystal. In particular, for the (100) direction $\sigma_L^2 = C_{11}/\rho$ and $\sigma_T^2 = C_{44}/\rho$ where ρ is the density of the crystal. Values of the elastic constants for some ionic crystals are given in Table (I.2-1).

Salt	C_{11}	C_{12}	C_{44}
LiF	11.2	4.5	6.32
NaCl	4.85	1.25	1.27
KCl	4.05	0.66	0.63
KBr	3.46	0.56	0.52
KI	2.75	0.45	0.37
MgO	29.2	9.1	15.4
CaO	20.0	6.1	7.65
CaF_2	16.49	4.46	3.38
BaF_2	8.9	4.0	2.53

Table I.2-1:   Elastic constants for some ionic crystals. All values are in 10^{11} dynes/cm^2 . Data for the alkali halides and MgO from [13] . Data for CaO from [14] . For the fluorites from [15] .

The Cauchy relation for an ideal cubic crystal require that $C_{12} = C_{44}$. This last condition is only moderately satisfied for the alkali halides (Table (I.2-1)), but it is not fulfilled by the other crystals like the oxides and fluorites.

As mentioned in the previous section, the elastic constants are determined mainly by the repulsive interaction between ions. This can be understood if we notice that for cubic crystals the elastic constants $C_{\alpha\beta, \gamma\lambda}$ (according to the general nomenclature) are given in terms of the force constants by the following expression:

$$C_{\alpha\beta, \gamma\lambda} = -\frac{1}{2v} \sum_{jj'} \sum_{\varrho'} V_{\alpha\beta}\begin{pmatrix} 0 & \varrho' \\ j & j' \end{pmatrix} R_{\gamma}\begin{pmatrix} 0\varrho' \\ jj' \end{pmatrix} R_{\lambda}\begin{pmatrix} 0\varrho' \\ jj' \end{pmatrix}, \quad (I.2-7)$$

where v is the volume per unit cell, $R_{\gamma}\begin{pmatrix} 0 & \varrho' \\ j & j' \end{pmatrix}$ is the γ component of the vector leading from ion $\begin{pmatrix} 0 \\ j \end{pmatrix}$ to ion $\begin{pmatrix} \varrho \\ j' \end{pmatrix}$ and $V_{\alpha\beta}\begin{pmatrix} 0 & \varrho' \\ j & j' \end{pmatrix}$ is the corresponding force constant. The calculated values of the elastic constants C_{11}, C_{12} and C_{44} for some alkali halides within the Born model (with only Coulombic and exponential repulsive terms) are displayed in Table (I.2-2).

The calculated values shown in Table (I.2-2) are correct within about 10% for C_{11} and 20% for C_{12} and C_{44} , with respect to the experimental values given in Table (I.2-1). The Born model obviously predicts that the Cauchy relation $C_{12} = C_{44}$ holds, this being clearly only approximately true.

	C_{11}	$C_{12} = C_{44}$
LiF	10.38	6.29
NaCl	4.68	1.27
KCl	3.61	0.82
KBr	3.10	0.68
KI	2.49	0.51

Table I.2-2: Calculated elastic constants with the Born model. All values are in 10^{11} dynes/cm^2 . Data from ref. [13] and [2] .

The partial contributions to C_{44} in Table (I.2-2) of the Coulomb and repulsive forces are given in Table (I.2-3).

C_{44}	LiF	NaCl	– KCl	KBr	KI
W_E	-17.94	-4.66	-3.00	-2.49	-1.89
W_R	28.32	9.34	6.61	5.51	4.38

Table I.2-3: Partial contributions from the Coulomb interaction W_E and the repulsive interaction W_R to the elastic constant C_{44} in some alkali halides. All values are in 10^{11} dynes/cm^2 . Data from [13] and [2] .

Finally, in the cleavage force theory for the surface energy of an ionic crystal, developed in Chapter II, we will show that the elastic constants play an important role.

I.3   Defects in ionic crystals

The presence of defects in ionic crystals is manifested strikingly by several physical properties of these materials. The large ionic conductivities observed at high temperature in crystals with the fluorite structure is a typical example [18] . On the other hand, the customary harmonic treatment of lattice vibrations developed in the preceding section, does not account for the presence of defects. However, information regarding phonom-phonom interactions together with properties associated with the equilibrium defect assembly, can be obtained from inelastic neutron scattering experiments.

In ionic crystals two kind of defects are particularly important, i.e. Schottky and Frenkel defects. A third kind of defect, known as a color center, will be briefly considered here and more extensively studied in Chapter III for the molten salt case.

(a)   Schottky and Frenkel defects

These two types of defects are illustrated in Fig. (I.3-1): a pair of vacancies of cation and anion is called a Schottky defect, while an interstitial ion and the corresponding vacancy is known as a Frenkel defect. Again here we find another example of the effects of the Coulomb forces; they prevent the presence of those defects which do not keep the overall electrical neutrality of the bulk crystal.
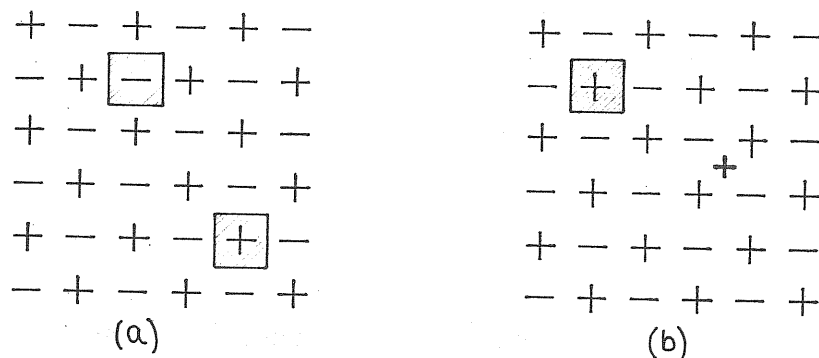
(a)

(b)

Figure I.3-1:   Schottky defect (a) and Frenkel defect (b) in an ionic crystal .

These defects have a different   Gibbs   free energy of formation. In NaCl, for instance, the Schottky defect has the smallest free energy of formation and is therefore the dominant defect in thermal equilibrium conditions. Some values of Schottky defect energies, in the alkali halide crystals are given in Table (I.3-1).

$\emptyset$	Li	Na	K	Rb
F	2.68	–	2.64	–
Cl	2.12	2.02-2.12	2.22-2.30	2.0
Br	1.80	1.68-1.74	1.99-2.53	–
I	1.34	–	1.56-1.60	–

Table I.3-1:   Schottky defect energies in the alkali halide crystals. All values are in ev. Data from [19] .

In the fluorite structure in particular in CaF_2 , the lowest formation free energy corresponds to the anion Frenkel defect. In this structure, in fact, very large ionic conductivities are found in the high temperature solid phase to be associated with a large dynamic concentration of defects in the anion sublattice.

The equilibrium number of Schottky defects in an alkali halide can be approximated by: $n_s = C N \exp(-\emptyset/2K_BT)$ where N is the number of ions (positive or negative) per cubic centimeter, C is a number which depends on the salt (for $NaCl$ $C \simeq 2.7$ [20]   ), $\emptyset$ is the Schottky defect energy and T is the absolute temperature. Close to the melting point this equation gives for $NaCl$ $n_s \approx 10^{18} \, cm^{-3}$, i.e., about one vacancy per 10^4 ions. At room temperature $n_s \approx 10^6 \, cm^{-3}$. The diffusion coefficient $\mathcal{D}_v$ of the vacancies may be evaluated from the measured mobilities μ with use of the Einstein-Nerst relation,

$$\mathcal{D}_v = \left(\frac{e}{K_B T}\right)^{-1} \mu \, ,\qquad (I.3-1)$$

which is usually found to be different from the diffusion coefficient $\mathcal{D}_t$ determined in a tracer diffusion experiment. The ratio $\mathcal{D}_t/\mathcal{D}_v$ is known as the Haven ratio H_r . In silver compounds $H_r \approx 0.5$, while in molten alkali halides $H_r > 1$. For small concentration of lattice defects $(n/N < 10^{-4}$, say $)$, the motion of defects (and

the corresponding ionic motion which lead to charge transport) are
not correlated, and one can write for D_{ν} the expression,

$$D_{\nu} = \frac{1}{6} \nu_{\nu} d_{\nu}^{2} \quad , \qquad (I.3\text{-}2)$$

where d_{ν} and ν_{ν} are the defect jump distance and frequency,
respectively. A similar expression for D_{t} can be written as
follows, $\quad D_{t} = \frac{1}{6} \nu_{t} d_{t}^{2} f_{t} \quad [21] \quad , \qquad$ where f_{t}
is the correlation factor which takes account of the non-random nature
of the tracer jumps. The quantity ν_{ν} in Eq. (I.3-2) can be
regarded, on the other hand, as the inverse of an ionic self-diffusion
time $\quad \tau = 1 / \nu_{\nu} \quad$. In the case of NaCl
containing CaCl_{2} [22], it is found that the mobility of the positive-
ion vacancies may be expressed in the form,

$$\mu_{\nu+} \simeq \frac{6.3 \times 10^{5}}{T} e^{-\epsilon_{+}/k_{B}T} \frac{cm^{2}}{Volt\text{-}sec} , \qquad (I.3\text{-}3)$$

where $\quad \epsilon_{+} \simeq (0.78 \pm 0.02) \; eV.$ in the range
from $823°K$ to $953°K$. If we roughly estimate $d_{\nu} \sim n_{s}^{-1/3}$
we can calculate ν_{ν} in Eq. (I.3-2) using Eq. (I.3-1) and Eq.
(I.3-3); the result at $\quad T = 953 \; °K \quad$ (the melting
temperature for NaCl is Tm = 1074°K) is: $\nu_{\nu+} \simeq 1. \; 10^{10} \; sec^{-1}$,
therefore, the associated cation self-diffusion time results: $\tau \simeq 10^{-10} sec.$

The ionic diffusion times in pure molten salts are of the
order of $\quad 10^{-12} \quad$ sec. near the freezing point.

b) Color centers in ionic crystals containing excess metal

When an alkali halide crystal is heated in the vapor of its
metallic constituent, an excess of metal is incorporated in the crystal.
The new system shows absorption bands in the visible and ultraviolet,
which were absent in the original (pure) crystal. Figure (I.3-2) shows
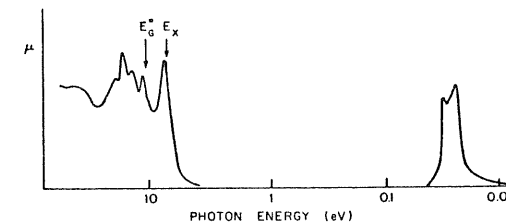an absorption spectrum of a typical (pure) alkali halide crystal.

Figure I.3-2:   Absorption spectrum of a typical alkali halide crystal.

The spectrum in the high frequency region is due to electronic excitations in the crystals, the lower of which correspond to the first exciton peak and first interband transition to the conduction band (E°_G). The spectrum in the far infrared corresponds to optical phonoms.

The alkali halide crystals containing excess metal, on the other hand, show new absorption bands as can be seen in Fig. (I.3-3) for KBr at 10%. The trapped electron in an anion vacancy, added
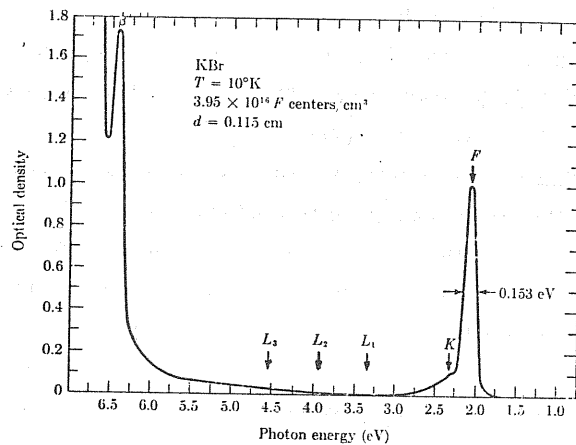
Figure I.3-3:   Absorption bands presented in   KBr   containing excess potassium. The new bands are designated by the F, K, L, and ρ bands. Data from [23] .

through the excess metal in the crystal, is responsible for the F- band.

It corresponds to the transition from the ground state to the first excited state ($1S \longrightarrow 2p$). The F-absorption energy E_F satisfies the simple relation (Mollow law):

$$E_F \sim \pi \hbar R^{-2} ,$$ (I.3-4)

where R is the nearest neighbor distance. For KBr , R = 3.298 $\mathring{A}$ and from Eq. (I.3-4), $E_F \sim 1.9$ ev.   . The number of F   centers per cm^3 , n_F , on the other hand, can be calculated with the Smakula's equation [24]:

$$n_F = \frac{q}{4\pi} \frac{mc}{e^2 \hbar} \frac{n_0}{(n_0^2 + 2)^2} \frac{1}{f_F} \mu_{max} \Gamma ,$$ (I.3-5)

where n_0 is the crystal refractive index, f_F is the oscillator strength, μ_{max} is the maximum absorption coefficient and Γ is the full width at half maximum of the F-band. Eq. (I.3-5) is valid for a Lorenzian-shape band   [25]   .

The absorption of alkali metal from the vapor by the alkali halide crystal can be described by a diffusion phenomenon. For a given temperature and a given number of metal atoms (in the vapour phase) per cm^3 , m_N , a certain saturation number density, n_F , of F-centers is obtained. In Fig. (I.3-4) the ratio n_F/m_N is plotted versus the reciprocal absolute temperature.
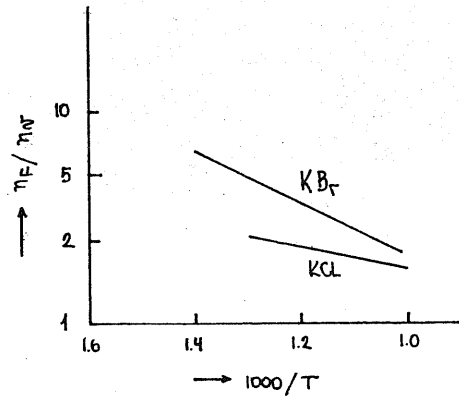
Figure I.3-4:   The ratio n_F/n_{av} in equilibrium for   KBr,   KCl   [26].

n_F , n_{av} are the numbers / cm^3 of   F centers in the crystal and alkali

atoms in the vapor phase, respectively.

According to the law of mass action, we have: $n_F/n_{av} \sim e^{-\phi/k_oT}$

where ϕ is the energy required to take an atom from the

vapor and incorporate it as an   F center   in the crystal. From Fig.

(I.3-4) we obtain: $\phi(K-KBr)= -0.25$ eV and

$\phi(K-KCl) = -0.10$ eV .

From the fact that ϕ is negative we conclude that energy

is released by taking an atom from the vapor into the crystal. The

incorporation of a metal atom by the crystal may be pictured as follows:

first, the atom is absorbed at the crystal surface; then, the atom may

split into a positive ion and an electron, and a negative ion from the

crystal may jump into a position near the absorbed ion. The electron

and the anion vacancy produced may diffuse into the crystal; at the end

the electron will become trapped at an anion vacancy [26] .

(c)   Absorption bands in alkali halides containing F centers

Figure (I.3-3) shows a number of bands other than the F - band.

We can briefly discuss the origin:

i)   K - band: there is general agreement that the K - band is

associated with the higher energy transitions of the F center, i.e.,

$1s \rightarrow np$ (n = 3,4,5...)   [27] .

ii)   L - bands: it is believed that L - bands arise from transitions

to states that are degenerate with conduction states [28] .

iii) β - band: this band lies in the low-energy side of the fundamental

absorption edge of the pure alkali halide. It is thought to involve the

excitation of a halogen ion near the F center [29] . This band can

be regarded also as due to the perturbation of the free exciton in

the pure crystal by the presence of the F center, giving rise to a

bound exciton. An estimation of the position of the β - band respect

to the absorption edge can be performed using the charge transfer model

[30] . The model for the β - band in which an electron from a

halogen ion is transferred into the nearby F - center, giving rise to

an   F - center (two electrons bounded in the cavity), allows an estimation

of the oscillator strength for this process [31] .

A somewhat different picture from that shown in Fig. (I.3-3) is
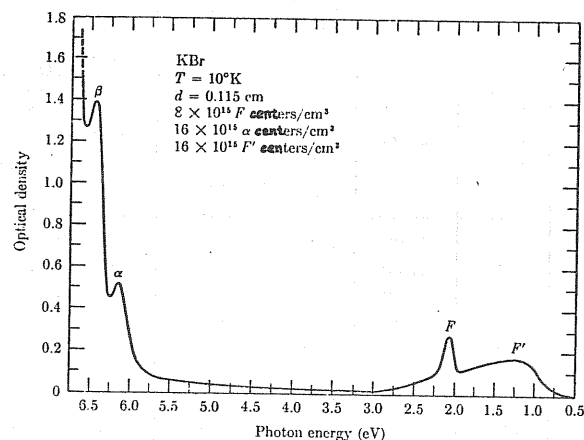
Figure I.3-5:   Absorption spectrum in KBr after illumination in the F - band.
The F - centers are converted to F¹ centers and the α - band appear. [23] .

obtained if the crystal is illuminated with F - light, Fig. (I.3- 5).
The result of the treatment is the conversion of F- centers to F¹
centers. That is, some of the F - center electrons are liberated
by the photons and are successively captured by other F - centers. This
process produces anion vacancies (left behind by the excited electrons).
These vacancies are then responsible for the α band shown in Fig.
(I.3-5): this band corresponds to the perturbation of the free exciton
by the presence of a negative ion vacancy. Similar calculations of the
β - band treatment have been applied to the α - band [30,31] .

I.4   Melting of ionic crystals

(a)   Structural aspects

From a phenomenological point of view, attempts have been made
in order to correlate the melting temperature with the interionic
pair potentials in the alkali halides. To be more precise, we can take
the simple interionic potentials given by Eq. (I.2-1), which are
consistent with the Born repulsive term in Eq. (I.1-2).

These potentials are:

$$\emptyset_{+-}(R) = -\frac{e^2}{R} + \frac{a}{R^n}$$

$$\emptyset_{++}(R) = \emptyset_{--}(R) = \frac{e^2}{R} \tag{I.4-1}$$

Here,   a   =   A/M   , where   A   is defined in Eq.
(I.1-2) and   M   is the coordination number in the structure
(we suppose the nearest-neighbor ions dominate in the repulsive term;
note that $n \sim 10$).

A scale of lengths (and energies) can be introduced

by defining:

$$\lambda = \left(n\, a\, / e^2 \right)^{1/n-1} = \left(\frac{\alpha_R}{M} \right)^{1/n-1} R_o , \qquad (I.4-2)$$

where R_o is the equilibrium lattice spacing and α_R is the corresponding Madelung constant. The corresponding scale of energies simply is e^2/λ .

The extent to which a rule of corresponding states can be developed is indicated by calculations for melts of inert gas ions [32] . Within the context of ionic crystals, this kind of treatement leads to an equation of state that takes the corresponding-states form [33] ,

$$P = \frac{e^2}{\lambda^4}\ f\left(N/\lambda^3 ,\ \lambda K_B T/e \right) . \qquad (I.4-3)$$

Here, P is the pressure and f is a 'universal' function of the variables indicated in parenthesis. If this approach is correct, the value of $\lambda K_B T / e^2$ at the melting point should be the same for all the alkali halides. As Table (I.4-1) shows, one obtains a good correlation between the melting temperature of these systems, which can be expressed simply as

$$T_m \sim \left(3 \times 10^{-5}/\lambda \right)\ ^\circ K . \qquad (I.4-4)$$

	$R_o(\text{Å})$	$T_m(K)$	λT_m (10^{-5} cm deg)	$\Delta V/V_s$ (%)	ΔS (cal deg^{-1})
LiF	2.014	1121	2.25	29.4	5.77
LiCl	2.570	887	2.27	26.2	5.39
LiBr	2.751	823	2.27	24.3	5.13
LiI	3.000	718	2.21	–	4.72
NaF	2.317	1265	2.92	27.4	6.2
NaCl	2.820	1074	3.02	25.0	6.23
NaBr	2.989	1023	3.04	22.4	6.12
NaI	3.237	933	3.01	18.6	6.04
KF	2.674	1129	3.02	17.2	5.97
KCl	3.147	1045	3.28	17.3	6.08
KBr	3.298	1013	3.34	16.6	6.06
KI	3.533	958	3.39	15.9	6.02
RbF	2.815	1048	2.96	–	5.76
RbCl	3.291	988	3.26	14.3	5.70
RbBr	3.445	953	3.27	13.5	5.77
RbI	3.671	913	3.34	–	5.73
CsF	3.004	955	2.88	–	5.32
CsCl	3.571	918	3.18	10.0	5.27
CsBr	3.720	909	3.29	26.8	6.20
CsI	3.956	894	3.42	28.5	6.27

Table I.4-1:   Lattice spacing and melting parameters in the alkali halides. Data from [33] .

This relation is not valid for the lithium salts where the neglect of

short-range repulsions between the relatively large anions is less justified.

On the other hand, the small but systematic variation of the quantity λT_m with the negative ion suggests that the ratio of the ionic radii should be considered as a new relevant parameter in a more refined equation of state. The ionic radii ratio, in fact, is found to correlate with the melting temperature [34] as shown in Fig. (I.4-1).
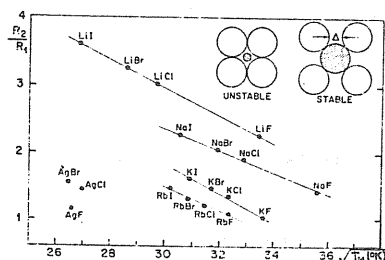
Figure I.4-1:   Ratio of the ionic radii versus the square root of the melting temperature in the alkali halides. R_2 is the radio of the larger ion and R_1 the radius of the smaller. $\Delta = \sqrt{2}\, R_1 - (2-\sqrt{2})\, R_2$. Data from [34] .

The last two columns of Table (I.4-1) report the values of the

fractional volume change $\Delta V / V_{solid}$ and of the entropy change ΔS on melting of the alkali halides. The volume change is related to the coordination numbers in the liquid and in the solid through the relation [35]

$$M_L = M_S \frac{V_S}{V_L} \left(\frac{R_o^L}{R_o^S} \right)^3 , \qquad (I.4-5)$$

where $M_{L,S}$ are the coordination numbers in the liquid (L) and in the solid (S) (see next section) $V_{L/S}$ are the corresponding molar volumes, R_o^L is the position of the peak in $g_{+-}(r)$ (i.e., the unlike ions radial distribution function; see next section) and R_o^S is the nearest-neighbor distance in the crystal. Neutron diffraction data for molten NaCl [36] give for the 'close-contact' coordination number in the liquid, $M_L \sim 4$ the decrease from $M_S = 6$ to $M_L = 4$ reflects the large increase of the molar volume on melting (25% for NaCl, see Table (I.4-1).

It is worth noticing that, despite the appreciable decrease in the coordination number at melting, the cohesive energy of the ionic liquid (which is mainly due to the Madelung term) is not considerably different from that of the solid. It is found for NaCl at 1073 K° an internal energy of $711. \, 10^3 \, J/mol$, to be compared with the value of $764. \, 10^3 \, J/mol$ for the solid at 298°K. THis relatively small reduction in the cohesive energy is a consequence of the good charge ordering existing in the liquid near

freezing. This is shown in Fig. (I.4-2), which clearly demonstrates the existence of a well defined first-neighbor shell of anions (cations) around a cation (anion). The presence of a second shell of like ions is also evident. This alternation of charge is the most remarkable feature of the short-range order in the ionic liquid.
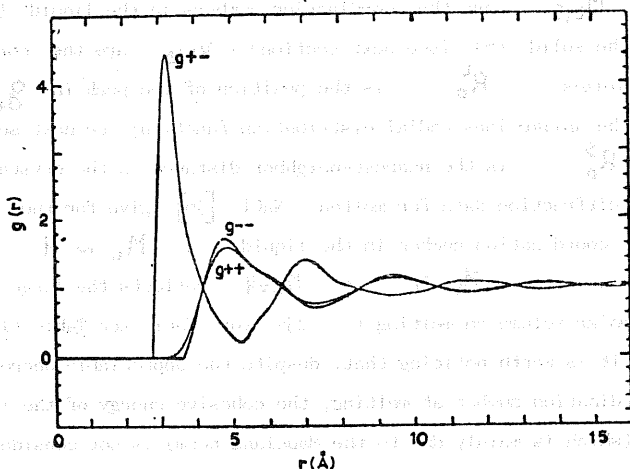
Figure I.4-2:   Pair distribution functions in molten RbCl from neutron diffraction experiments. Data from [37] .

Finally, of the total entropy change found at melting (see Table I.4-1), $\Delta S \sim 6$ cal $/^\circ$K   , roughly one third arises from random distribution of 'defects' in the liquid [38] and the rest from changes in the vibrational entropy.

The possible extension of the rigid-ion model (Born model) for the alkali halides described in Section I, to both the solid and the liquid phases near the melting temperatures, has been studied by Monte Carlo simulations [39] . It is found that the exponential form for the repulsive interaction is superior to the power-law form. The results for the total internal energy are in good agreement with experimental data. For NaCl at freezing a value of $717 \; 10^3$ J/mol is found for the cohesive energy.

(b)   Electronic aspects

The absorption bands observed in the alkali halides containing F centers (an example of which is given in Fig. (I.3-3) for KBr) are also found in the molten phase but shifted to lower energies. The theoretical aspects of the latter case will be discussed in Chapter III.

Here, we want to discuss about the shift of the absorption edge (first exciton line) of the pure crystal on melting. The optical absorption spectra in the ultraviolet have been obtained for the alkali halides [40] . Figure (I.4-3) shows the corresponding spectra
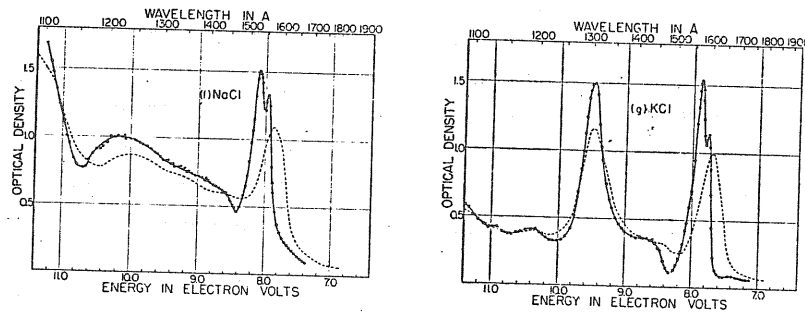
Figure I.4-3:   Optical absorption spectra in the ultraviolet for NaCl and KCl at 80° K. The dashed curves are room temperature data. From ref. 40 .

for NaCl and KCl.   Experiments on some alkali halides have also been performed in the liquid phase near freezing [41] . The spectra are found to be well described by the empirical Urbach rule:

$$\mu(E) = \mu_o \, exp\left[\, \sigma \, (E-E_o)/k_BT\right]$$, where μ_o, E_o and σ are fitting parameters. In Table (I.4-2) are given the values of these parameters for some alkali halides. From Table (I.4-2) it is clear that an abrupt shift of the first exciton line of 1.1 - 1.8 ev

	E_o (cryst)	σ(cryst)	E_o(melt)	σ(melt)
KI	5.890	0.830	4.71	0.65
KBr	6.841	0.774	5.51	0.53
KCl	7.834	0.745	6.22	0.63
NaCl	8.025	0.741	6.25	0.59
RbCl	7.510	–	6.05	0.51

Table I.4-2:   First exciton absorption peak energies E_o in the crystal and liquid phases. All values are in ev. Data from ref. [41] . σ is a fitting parameter appearing in the Urbach rule.

occurs on melting. It is then suggested that the loss in long range order on melting is primarily responsible for the reduction in the energy, ΔE_o , of the first exciton peak, through the change in electrostatic energy of the system. An approximate equation for ΔE_o can be written in terms of the difference of Madelung energies, E_{mad} in the solid and in the liquid, as follows,

$$\Delta E_o \simeq 2 \, E_{mad}(Crystal) - E_{mad}^{+}(melt) - E_{mad}^{-}(melt),\quad (I.4-6)$$

where the sign $+$ (−) refers to the cation (anion). In Table (I.4-3) are reported the calculated values of the electrostatic energies for the melt from the optical data and are compared with some theoretical

calculations. Experimental (second column) and theoretical results
(last three columns) compare very favourably for all the salts
investigated as shown in Table (I.4-3).

	ΔE_o	From Optical Data	Huggins Mayer Potential (a)	Pauling Potential (a)	Dixon and Sangster
KBr	1.33	6.95	7.06	7.01	
KI	1.18	6.52	–	–	6.67
KCL	1.61	7.18	7.44	7.33	–
NaCL	1.78	8.02	8.30	8.34	–
RbCl	1.46	6.91	7.08	7.04	6.97
NaI	–	–	–	–	7.23

Table I.4-3:   Electrostatic energies for some alkali halides at
freezing.. All values are in ev. Data from ref. [41] . (a) from ref.
[39] .

We can conclude that Eq. (I.4-6) can be used to obtain a rather
accurate value for the shift of the first exciton peak in the alkali
halides on melting. This result will be used in connection with the
β band in the molten phase in Chapter III.

I.5   Structure of molten alkali halides

In the study of the optical properties of metal-molten salt
solutions, to be presented in Chapter III, the knowledge of the liquid
structure results essential. In fact, it will be found that the short-
range ionic order present in the liquid (near the freezing point),
is responsible for the localization of the extra electron in a F -
like center in the molten salt. Evidence for this short-range order
was reported in Fig. (I.4-2) for   RbCl. The way in which this
information is extracted from the diffraction experiments (x-ray
neutrons) is reviewed   immediately below.

(a)   Liquid structure factors and radial distribution functions

In a typical (x-ray or neutron) diffraction experiment, the
measured quantity is the scattered intensity $I(\theta)$ through an angle
2θ of the incident radiation of wave length λ .
For a monatomic liquid (like argon, say), it can be written as follows,

$$I(\theta) = N\, f^2(K)\, S(K) ,$$ (I.5-1)

where $K = 4\pi \sin\theta / \lambda$, N is the number

of atoms in the liquid sample, $f(K)$ is the atomic scattering factor
and $S(K)$ is the liquid structure factor. The Fourier transform
of $S(K)$ is essentially the pair radial distribution function
$g(r)$, already found in the preceding section (see Fig. (I. 4-2)):

$$S(K) = 1 + n \int [g(r) - 1] e^{i K \cdot r} dr , \qquad (I.5-2)$$

where n is the number density of atoms. On the other hand, $g(r)$
is defined such that $4\pi n \, g(r) \, r^2 \, dr$ equals the
number of atoms in a spherical shell at a distance r from a given
atom.

For a two-component liquid, such as RbCl , there are three
pair distribution functions, g_{Rb-Rb} , g_{Cl-Cl} and g_{Rb-Cl} .
The experimental values for these functions are plotted in Fig. (I.4-2). The corresponding partial structure factors, S_{Rb-Rb} , S_{Cl-Cl}
S_{Rb-Cl} are shown in Fig. (I.5-1).

As is clearly shown in Fig. (I.4-2), there is an evident
alternation of charge (ions surrounded by opposite charged ions) in
an ionic liquid, giving rise to a net short-range order. This feature
is appropriately expressed in K space by a linear combination
of the alone partial structure factors, denoted by $S_{QQ}(K)$
and defined as

$$S_{QQ}(K) = \frac{1}{2} \left[S_{++}(K) + S_{--}(K) - 2 S_{+-}(K) \right] , \quad (I.5-3)$$
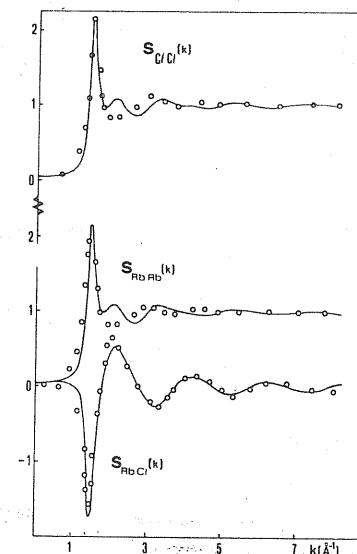
Figure I.5-1:   Partial structure factors in molten   RbCl   at   1023°K . The full
lines are   MSA   results. The circles neutron diffraction data [37] .

for a 1:1 system like RbCl . The plot of $S_{QQ}(K)$ for RbCl
is shown in Fig. (I.5-2). $S_{QQ}(K)$ expresses the correlations
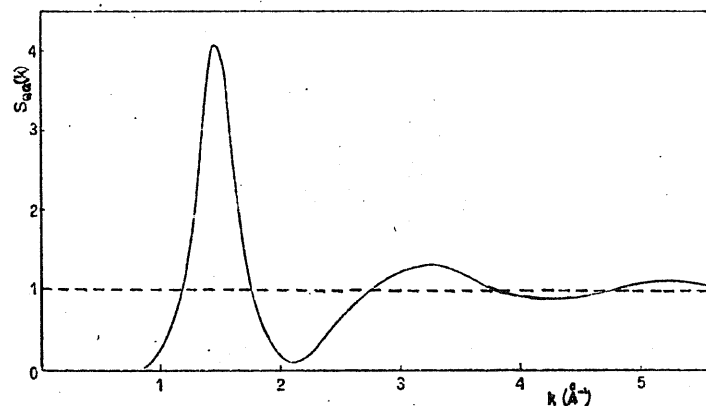
Figure I.5-2:   Charge-charge structure factor for molten   RbCl   constructed from neutron diffraction data on partial structure factors. Data from $\begin{bmatrix} 37 \end{bmatrix}$.

between charge density fluctuations in the ionic liquid; this is made evident when one notices that the corresponding radial distribution function is given by $\frac{1}{2} \left[g_{++}(r) + g_{--}(r) - 2 g_{+-}(r) \right]$, which measures the probability of finding a charge of the same sign at a distance r from a given charge.

Another important point to mention here is the relation of $S_{QQ}(K)$ to the static-screening properties of an ionic liquid. It can be shown $\begin{bmatrix} 33 \end{bmatrix}$ that for a fluid of rigid ions obeying classical

statistical mechanics, the following relation between the static dielectric constant $\varepsilon(K)$ of the ionic system and $S_{QQ}(K)$ is found:

$$ 1/\varepsilon(K) \;=\; 1 \;-\; \frac{4\pi n\, e^2}{K^2\, K_B T} \; S_{QQ}(K). \qquad (\text{I.5-4}) $$

The coordination numbers mentioned in the preceding section can be obtained from the experiments through the functions $g_{+-}(r)$

The required information to this respect is contained in the main peak of $g_{+-}(r)$. The determination of the coordination numbers is, however, not unambiguous because this peak is not sharply defined on its large $r-$ side. These are two kinds of coordination numbers which can be extracted from $r^2\, g_{+-}(r)$ by integration:

i) the 'close contact' coordination number, obtained by assuming the function $r^2\, g_{+-}(r)$ to be symmetric around the maximum of the peak and thus using only the data on its short $r-$ side;

and ii) the 'near neighbor' coordination number, obtained by integrating the full $g_{+-}(r)$ up to the first minimum of $r^2\, g_{+-}(r)$

These numbers for molten   NaCl   are $4.0 \;\pm\; 0.2$ and 5.2 ± 0.4 $\begin{bmatrix} 36 \end{bmatrix}$.

(b)   Theoretical aspects: the mean spherical approximation (MSA)

The starting point in the calculation of the pair distribution functions are the Ornstein - Zernike equations, which can be considered as the defining equations of the direct correlation functions $C_{ij}(r)$.

For a two-component system, such as a molten salt, those equations can be written [42] as follows:

$$h_{ij}(r) = C_{ij}(r) + \sum_K n_K \int d\underset{\sim}{r}' \, C_{iK}(|\underset{\sim}{r}-\underset{\sim}{r}'|) \, h_{Kj}(r'), \quad (I.5-5)$$
$$i,j,K = 1,2 ,$$

where $h_{ij}(r) = g_{ij}(r) - 1$, and n_K are the partial number densities of the components. The function $C_{ij}(r)$ is taken to go, at large r , to the bare pair potential $\phi_{ij}(r)$,

$$\lim_{r \to \infty} C_{ij}(r) = - \phi_{ij}(r) / K_B T , \quad (I.5-6)$$

provided that the system is far from the critical point. For a system of positive and negative ions, as in a molten salt, the potential ϕ_{ij} is given by: $\phi_{ij}(r) = z_i z_j \, e^2 / \epsilon_e \, r.$

An approximate solution for this problem is given by the MSA. Essentially, the MSA is a Debye - Hückel theory with hard-spheres boundary conditions.

The approximations involved in the MSA are easily visualized if we consider a system of equisized ions, of diameters $\sigma_+ = \sigma_-$ ($= \sigma$, say) and valences $z_+ = -z_-$. We then define,

$$g_{NN}(r) = \frac{1}{2} \left[g_{++}(r) + g_{+-}(r) \right] \quad (I.5-7)$$

and

$$g_{QQ}(r) = \frac{1}{2} \left[g_{++}(r) - g_{+-}(r) \right] . \quad (I.5-8)$$

The corresponding partial structure factor $S_{QQ}(K)$ to the function $g_{QQ}(r)$ was already introduced in the preceding paragraph. Here, the Ornstein - Zernike equations split in the following two integral equations:

$$h_{NN}^{(r)} = C_{NN}(r) + 2n \int d\underset{\sim}{r}' \, C_{NN}(|\underset{\sim}{r}-\underset{\sim}{r}'|) \, h_{NN}(r'), \quad (I.5-9)$$

and

$$h_{QQ}^{(r)} = C_{QQ}(r) + 2n \int d\underset{\sim}{r}' \, C_{QQ}(|\underset{\sim}{r}-\underset{\sim}{r}'|) \, h_{QQ}(r'), \quad (I.5-10)$$

while the MSA conditions become:

$$C_{NN} = 0 \quad \text{for} \quad r > \sigma \, ,$$

$$g_{NN} = 0 \quad \text{for} \quad r < \sigma \, , \qquad \text{(I.5-11)}$$

and

$$C_{QQ} = -z^2 e^2 / \varepsilon_e r \, k_B T \quad \text{for} \quad r > \sigma$$

$$\qquad \text{(I.5-12)}$$

$$g_{QQ} = 0 \qquad \text{for} \quad r < \sigma \, .$$

Equation (I. 5 - 9 - 11) coincide with the Percus - Yevick equations for a fluid of neutral hard spheres of density $2n$ and diameter σ , whose solution [43] is:

$$C_{NN}(r) = A_0 + A_1 (r/\sigma) + A_2 (r/\sigma)^2 \, , \qquad \text{(I.5-13)}$$

where the constants A_i are written in terms of the packing fraction $\eta = \frac{\pi}{3} n \sigma^3$ [43] . The solution of Eqs. (I. 5 - 10 - 12) is given by [44] ,

$$C_{QQ}(r) = \frac{x^2}{12\eta} \left[2B + B^2 r/\sigma \right] \, , \qquad \text{(I.5-14)}$$

where $x = k_0 \sigma$ (k_0 is the Debye - Huckel value of the inverse screening length) and $B = -[1 + x - (1+2x)^{1/2}]/x$.

The comparison of the MSA results for the functions $h_{NN}(r)$ and $h_{QQ}(r)$ with the Monte Carlo simulations is shown in Fig. (I.5-3). Values at contact are overestimated by approximately 10% . At distances $r \sim 1.4 \, \sigma$ the MSA fails to predict the structure present in h_{NN} . The situation is somewhat worse for $h_{QQ}(r)$, for which the MSA predicts oscillations that are both weaker and out of the phase relative to the Monte Carlo data. This situation is sensibly improved by using the self-consistent Ornstein-Zernike approximation (SCOZA) [45] .

Finally it should be noted that within the MSA for equized ions a simple analytic expression for the $S_{QQ}(k)$ function [46] is obtained:

$$S_{QQ}(k) = (k\sigma)^4 \left[(k\sigma)^4 + 8q^4 - 4q^2(2q^2 - k^2\sigma^2) \cos k\sigma + 8q^3 k\sigma \sin k\sigma \right]^{-1} \, ,$$

$$\qquad \text{(I.5-15)}$$

where $q = \frac{1}{2}(1-B) x$.
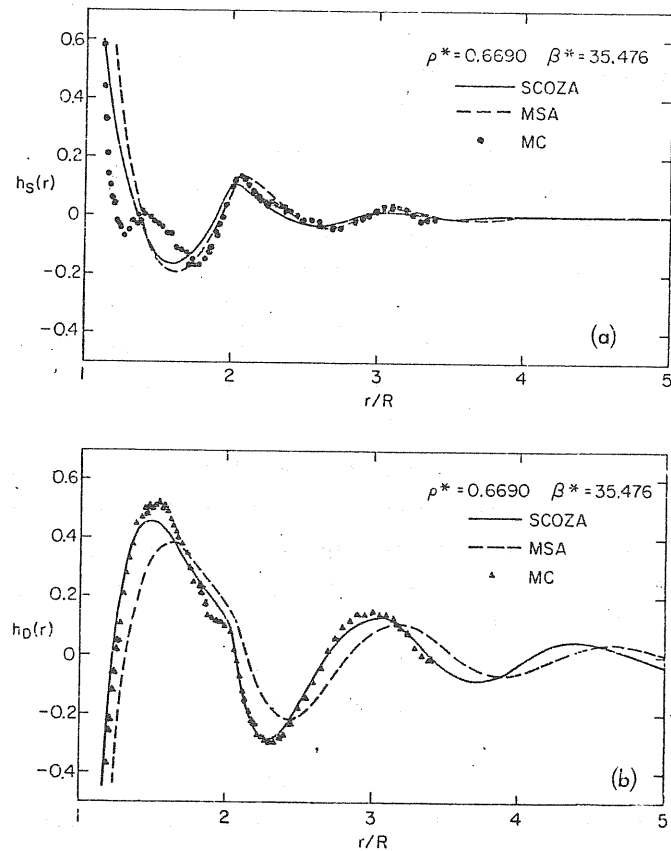
Figure I.5-3: Monte Carlo $(\bullet, \blacktriangle)$ results for $h_S(r) = h_{NN}(r)$ and $h_D(r) = h_{QQ}(r)$ are compared with the predictions of the MSA (---) and of the SCOZA (-) for $\beta^* = 6\eta/4\pi = .669$ and $\rho^* = \chi^2/24 = 35.476$. Data from [44] .

Analytic solutions for the pair correlation function have been also obtained within the MSA [47 , 48] . These results will be used to build up the theory of Chapter III.

On the other hand, the use of the MSA allows a systematic determination of the ionic radii in the molten alkali halides [49] . In Fig. I.5-4) are plotted the ionic radii for these molten salts versus temperature.

Finally, the MSA results for the general case $\sigma_+ \neq \sigma_-$ have been also obtained [50] .
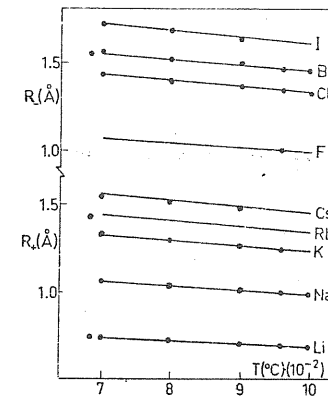
Figure I.5-4: Ionic radii in molten alkali halides as function of temperature. Data from [49] .

CHAPTER II

SURFACE ENERGY OF IONIC CRYSTALS

CHAPTER II

Surface energy of ionic crystals

In this chapter we examine a simple model for the surface energy
of ionic crystals [65] . To this end, much of the content of sections
1 and 2 of Chapter I will be needed here, i.e.: the description of the
Born model of ionic crystals including the discussion of the van der
Waals interaction of closed shell ions and its relative importance
in the surface energy problem, and the introductory survey to the
role of elastic constants in the lattice vibrations of ionic crystals.

Section 1 of this chapter is dedicated to a general introduction
of surface thermodynamic concepts, like the specific surface free energy
F^s and specific surface enthalpy H^s of an ionic crystal. In this
section we also describe some of the experimental techniques to measure
surface thermodynamic functions and discuss some of the practical problems
in their determination. Finally, we report the presently available data
for ionic crystals.

Section 2 examines the theory of the cleavage force in ionic
crystals within the spirit of a universal model for the surface energy
of solids originally applied to metals [63] . A rather drastically different
physical model is clearly involved for ionic materials as opposed to
metals since : (a) optic as well as acoustic phonons enter the problem,
and (b) the van der Waals interactions arise from closed electron shells .

In Section 3 we derive an expression for the surface energy
of ionic crystals from the two limiting behaviours of the cleavage
force in Section 2, by assuming, (as in [63]), a universal scaled
form for this force. There results a simple expression which relates
the surface energy to some bulk properties of an ionic crystal, these
being the elastic constants, the electronic dielectric constant, the
optical band gap and the interplanar spacing. These bulk properties
are known for many materials and this relation should thus be useful
for rough estimates of the surface energy of ionic crystals.

II.1. Thermodynamic definitions and experimental data

We start a brief outline of surface thermodynamics, in order to
introduce the physical quantities which are measured experimentally.
It should be noted that the surface free energy and surface tension,
are in principle different quantities for a solid [51] , the former
being the work spent in forming a unit area of surface, while the latter
involves the work spent in stretching the surface [52] .

(a)   Surface thermodynamics: Surface energy and surface tension
of an ionic crystal

By surface we mean an inhomogeneous boundary region between
a solid and vacuum. The vapour pressure being small for the systems
of present interest at low temperature. One can associate with the
surface such thermodynamic functions as energy and free energy, which
are extensive properties of the surface (in the thermodynamic sense)
provided that the crystal is sufficiently large. In a finite crystal
the surface energy can be decomposed into the face, edge, and corner
energies. To give an example of variation with particle size, let us
consider 1 gr. of NaCl, of density $\rho = 2.2 \ gr/cc$ and with
assumed surface energy per unit area $E^s = 300 \ ergs/cm^2$ and
edge energy per unit length $K = 3 \times 10^{-6} \ ergs/cm$. The

original cube is now considered to be succesively divided into smaller cubes, and the number of such cubes, their area and surface energies, and edge and edge energies are summarized in Table (II.1-1).

L Side cm	cA Total area cm²/g	Lo Total edge cm/g	$cA\,E^s$ Surface energy ergs/g	$Lo\,X$ Edge energy ergs/g
0.77	3.6	9.3	1080	2.8×10^{-5}
0.1	28	550	8.4×10^3	1.7×10^{-3}
0.01	280	5.5×10^4	8.4×10^4	0.17
0.001	2.8×10^3	5.5×10^6	8.4×10^5	17
10^{-4} (1μ)	2.8×10^4	5.5×10^8	8.4×10^6 (0.2 cal)	1.7×10^3
10^{-6} (100 Å)	2.8×10^6	5.5×10^{12}	8.4×10^8 (20 cal)	1.7×10^7 (0.4 cal)

Table II.1-1: Variation of surface energy per unit mass with particle size. Data from [53].

It may be noted from the table that for small particles $(L \sim 1\mu)$ the surface energy becomes significant $(\sim 0.2 \text{ cal})$ while only for very small particles $(L \sim 100 \text{ Å})$ the edge energy becomes important $(\sim 0.4 \text{ cal})$.

From a theoretical point of view one can avoid the size effects by considering a semi-infinite ionic crystal. In order to appropriately define all the surface quantities, let us consider a finite cylindrical

portion G of the semi-infinite crystal to have a volume V and an area cA in the surface. Let N be the total number of molecules contained in this portion of the crystal. The specific* surface energy E^s is defined by the relation:

$$E = N E^0 + cA\,E^s ,$$
(II.1-1)

where E is the total energy of the portion G and E^0 is the bulk molecular value of the energy. The second term in Eq. (II.1-1) represents the excess value of the energy due to the presence of the surface. Similar equations to Eq. (II.1-1) can be written for the total entropy S and the total Helmholtz free energy F of the system G. From this fact follows the definition of the specific surface free energy F^s to be:

$$F^s = E^s - T S^s .$$
(II.1-2)

An equivalent definition of F^s is obtained from the knowledge of F itself, i.e.

$$F^s = \left. \frac{\partial F}{\partial cA} \right)_{V,T,N} .$$
(II.1-3)

*Hereafter specific means 'per unit area'

An analogous expression to Eq. (II.1-3) is obtained from the Gibbs free energy [54] .

Besides the surface free energy, the specific surface enthalpy, H^s , presents also an experimental interest. The total enthalpy may also be written as a sum of 'bulk' and 'surface' contributions, therefore we find,

$$H^s = E^s + p V^s \qquad \text{(II.1-4)}$$

where V^s is defined by the relation:

$$V = N V^0 + \mathcal{A} V^s . \qquad \text{(II.1-5)}$$

In Eq. (II.1-4) p is the pressure applied on the system.

One last remark about the surface properties defined above must be done, i.e. these quantities represent net variations in the properties of bulk matter as a consequence of the presence of the surface and are not the characteristics of some two-dimensional phase or film [55] .

Let us consider finally the problem of surface work. The work done on a system is equal to the increase in the Helmholtz free energy of the (closed) system for a reversible isothermal infinitesimal change.

Then, for independent deviations in both volume and area we can

write,

$$dF\big)_T = \frac{\partial F}{\partial V}\bigg)_{T,\mathcal{A}} dV + \frac{\partial F}{\partial \mathcal{A}}\bigg)_{T,V} d\mathcal{A} \qquad \text{(II.1-6)}$$

where we can identify the second term as the work done on the system for an increase $d\mathcal{A}$ in the surface area, to be written as follows,

$$dW^s = \left[F^s + \mathcal{A} \frac{\partial F^s}{\partial \mathcal{A}}\bigg)_{T,V} \right] d\mathcal{A} . \qquad \text{(II.1-7)}$$

Now, there are two different ways of increasing the surface area of a solid: (i) by reversibly "cutting" the crystal (cleavage) producing an area $d\mathcal{A}$ of new surface, or (ii) by "stretching" the existing surface and therefore altering its state of strain. In the first process the number of surface atoms is increased while in the second it remains unchanged.

The specific surface free energy for (i) is independent of $\mathcal{A}$ and hence,

$$dW^s = F^s d\mathcal{A} . \qquad \text{(II.1-8)}$$

In method (ii) for an isotropic solid subjected to a homogeneous change in strain (without creating shear strains), the differentials can be written as

$$dW^S = \gamma\, d\mathcal{A} \qquad (\text{II.1-9})$$

where γ is the surface tension. Comparing Eq. (II.1-7) and Eq. (II.1-9) one finds,

$$\gamma = F^S + \mathcal{A}\left.\frac{\partial F^S}{\partial \mathcal{A}}\right)_{T,V} . \qquad (\text{II.1-10})$$

This equation illustrates the way γ relates to F^S . It is noted that for a liquid F^S is indipendent of $\mathcal{A}$, so that
$\gamma = F^S$.

b)   Experimental techniques

The experimental determination of the surface thermodynamic functions is subject to a number of uncertainities. Besides the crystal

cleavage method, we will also describe to some extent the calorimetric and solubility techniques.

b. 1)   The cleavage method

Measurement of the isothermal work needed to increase the surface by unit area is the most direct method of determining the surface free energy. This measurement is performed by some form of cleavage. In practice, it is frequently important, and difficult, to correct for dissipative effects which occur simultaneously with the increase in area. For example, in the case of impact cleavage by a falling blade, it is necessary to consider, in addition to the rebound of the weight, energy losses in the form of heat, sound and plastic deformation of the crystal. Since neglect of such effects leads to high values, it is usually assumed that the lowest observed result provides the best estimate of the surface free energy [56] .

A slow cleavage technique which avoids some of the dissipative effects mentioned above has been used [57] .

In this technique, a crystal in the shape of a bar with rectangular cross section (thickness 2t, width w) is partially cleaved from one end to form a crack at depth t extending a distance L along its length (see Fig. II.1-1). The critical force F needed to reinitiate the fracture is then measured on a tensile-testing machine. The surface free energy is calculated from the formula [54] ,

$$F^S = 6F^2 L^2 / \gamma\, w^2 t^3 \qquad (\text{II.1-11})$$
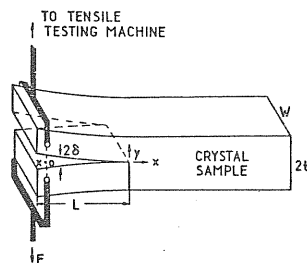
Figure II.1-1:   Propagation of wedge-induced crack in a cleavage experiment. The force F required to extend the crack is measured on a tensile-testing machine. From ref. [54] .

where Y is the Young's modulus in the direction of crack propagation. In deriving Eq. (II.1-11) isotropic elasticity is used. It has been noted, however, that Eq. (II.1-11) is reliable only if L is large with respect to t [58] . A reconsideration of the mechanics of the problem, taking into account the effects of shearing forces and end conditions, leads to:

$$1/F_{app}^{s} = 1/F^{s} + c\,(t/L)^{2}, \qquad \text{(II.1-12)}$$

where F_{app}^{s} is the apparent value of F^{s} as determined from

Eq. (II.1-11) and C is a constant factor for the crystal studied. A plot against $(t/L)^{2}$ is then made, and the value of F^{s} is obtained by extrapolation at $(t/L)^{2} = 0$.

b. 2)   Calorimetric techniques

The determination of surface thermodynamic functions from calorimetric measurements requires a study of the properties of a bulk system as a function of the extent of its surface. Since the values of the surface functions are obtained as differences between nearly equal quantities, their accurate evaluation demands the use of precise experimental techniques.

Calorimetric techniques are applied in the determination of the surface enthalpy H^{s} and the surface enthropyy S^{s} [55] . When a finely divided solid sample is dissolved in a suitable solvent, the normal heat of solution (i.e., ΔH) is decreased by the extra enthalpy associated with the surface. If the particles are identical, the effect (per gram) will vary inversely with the particle size (see the Table (II.1-1)), and will become detectable for particles having a size of about 1μ , as we have shown above (see discussion of Table (II.1-1) in section (II.1-a)). Thus, it has been suggested [59] that some of the scatter to be found in the heat of solution data reported in the literature may be attributed to an unsuspected dependence on particle size.

b. 3)   Solubility techniques

The solubility of a solid in a liquid depends upon its particle size. The relation governing the dependence was formulated originally for spherical particles [60] .

The surface free energy of an ionic crystal, F^S , can be obtained [61] through the equation,

$$F^S = F^S_{SL} + \gamma_{LV^0} \cos \theta + RT \int_0^{p^0} \Gamma \, d\ln p \, , \qquad (II.1-13)$$

where F^S_{SL} is the surface free energy for the interface between the solid and a saturated solution, γ_{LV^0} is the surface tension of the solution and θ is the contact angle of the solution with the solid. The last term in Eq. (II.1-13) represents the difference between the free energies of the clean solid surface and of the solid covered by adsorbed solvent vapor in equilibrium at the saturated pressure p^0 , calculated by integrating the adsorption isotherm in which Γ is the number of moles of adsorbed vapor per unit area.

c)   Experimental values of surface thermodynamic functions

The experimental values of surface thermodynamic functions are summarized in Table (II.1-2). The present available data are very

scanty, as can be seen from Table (II.1-2).

Property	Method	LiF {100}	NaCl {100}	KCl {100}	MgO {100}	CaO {100}	CaF₂ {111}	BaF₂ {111}
A^* (ergs/cm²)								
	Slow cleavage[b]	340			1200		450	280
	Slow cleavage[c]			110 ± 5				
	Slow cleavage[c]				1150 ± 80			
	Solubility		227					
H^* (ergs/cm²)								
	Heat of solution	276 ± 5						
	Heat of solution			252 ± 2				
	Heat of solution				1090			
	Heat of solution					1310 ± 200		
S^* (ergs/cm² deg)								
	Heat capacity				0.28			
	Heat capacity		0.084					
$H^*(T) - H^*(0)$ (ergs/cm²)								
	Heat capacity				50			
	Heat capacity	5						

Table II.1-2:   Experimental values of surface thermodynamic functions. All results are for 298°K unless otherwise indicated. (b) in liquid $N_2 (78°K)$, (c) in air. Data from ref. [55] .

A brief discussion of the surface thermodynamic function values given in Table (II.1-2) is necessary to understand the (rather sensible)

scatter of the data.

For what concerns the slow cleavage experiments, none of them were carried out in vacuo. It seems likely that the free energies obtained in these experiments refer to the interface with liquid N_2 [57] and to the surface covered with adsorbed air [58] , and that the values for clean surfaces should be somewhat larger. This effect is, however, not easy to evaluate.

The results obtained from measurements on powders of NaCl, MgO, and CaO are tentatively associated with the (100) face. Electron micrographs support this identification but in the case of KCl many spherical particles were observed. It is also necessary to use powders with different specific surface areas in order to establish a true surface effect. This was done for NaCl and KCl in the determination of H^S and for NaCl in the solubility experiment. However, for both MgO and CaO, the enthalpy results were derived using only one fine powder.

In discussing the results in Table (II.1-2) the difference between H^S and E^S , as in Eq. (II.1-4), is neglected. Since the surface entropy S^S is usually positive, the surface enthalpy at room temperature should exceed the surface free energy F^S .

Thus for NaCl and KCl these quantities are consistent with the expected result.

The two cleavage values of F^S for MgO agree well but are larger than H^S . This may be due to the uncertainty regarding the area of the powder used in the calorimetric work [62] .

II.2   Theory of the cleavage force

The specific surface free energy F^S (or surface energy σ) can be regarded as the work done to form unit area of new surface by reversibly cleaving the crystal, as discussed in the preceding section. This reversible work can be calculated from the knowledge of the cleavage force. A theory of the cleavage force for an ionic crystal is examined in this section within the spirit of a universal model for the surface energy of solids originally applied to metals [63] .

T he cleavage force is evaluated at small and large separations of the two crystal halves from phonom dispersion curves and from van der Waals interactions, respectively. In a later section it is shown how this two limiting behaviours can be connected by a scaling hypothesis.

a)   Cleavage force at small distances

We consider for definiteness the cleavage of a crystal with the NaCl structure along a (100) plane. Recalling the introductory discussion of the lattice vibrations in ionic crystals (section I.2) one expects the cleavage force, for a small relative displacement z from equilibrium of the two crystal halves, to be linear in z . We are going to evaluate the coefficient of proportionality (a force constant per unit area) A which determines the cleavage force F

for small displacements z of the two crystal halves,

$$F = A z \qquad (z \ll d) \qquad \text{(II.2-1)}$$

where d is the equilibrium distance between neighbouring planes in the bulk. It is now shown how A relates to the dynamical matrix of the ionic crystal as introduced in section (I.2).

We can write down the equations of motion of the planes, for the longitudinal vibrations along the (100) direction, from the equations of motion of the ions in the crystal as shown in Appendix A.

Denoting by an index ℓ the successive lattice planes of this family, we apply to the planes $\ell = 0$ and $\ell = 1$ weak external forces along the (100) direction of magnitude $-F$ and $+F$ per unit area, respectively (see Fig. (II.2-1)).

The equation of motion of the plane ℓ , built up of alternating positive and negative ions having masses m_1 and m_2. respectively, under the action of an external force per unit area F_ℓ can be written as

$$M_1 \ddot{u}_1(\ell) = -\sum_{\ell'} \left[V_{11}(\ell,\ell') \, u_1(\ell+\ell') + V_{12}(\ell,\ell') u_2(\ell+\ell') \right] + \tfrac{1}{2} F_\ell ,$$

$$\text{(II.2-2)}$$

$$M_2 \ddot{u}_2(\ell) = -\sum_{\ell'} \left[V_{21}(\ell,\ell') \, u_1(\ell+\ell') + V_{22}(\ell,\ell') u_2(\ell+\ell') \right] + \tfrac{1}{2} F_\ell ,$$

Here $u_{1,2}(\ell)$ are the displacements from equilibrium of the two subplanes ($1,\ell$) and ($2,\ell$) in the plane ℓ having masses M_1 and M_2 per unit area respectively, and $V_{ij}(\ell,\ell')$ is the effective force constant per unit area between the subplanes (i,ℓ) and (j,ℓ').

For this particular case, the (specific) dynamical matrix for longitudinal modes along the (100) direction (see Appendix A) can also be written as follows,

$$D_{ij}(q) = \sum_{\ell} V_{ij}(\ell) \, e^{-iq\ell d} . \qquad \text{(II.2-3)}$$

Introducing the Fourier transforms for $u_j(\ell)$ and F_ℓ ,

$$u_j(\ell) = \sum_{q} u_j(q) \, e^{iq\ell d}$$

$$\text{(II.2-4)}$$

$$F_\ell = \sum_{q} F_q \, e^{iq\ell d} ,$$

we can rewrite Eq. (II.2-2) for static displacements as follows,

$$D_{11}(q)\, u_1(q) + D_{12}(q)\, u_2(q) = \tfrac{1}{2} F_q$$

$$D_{21}(q)\, u_1(q) + D_{22}(q)\, u_2(q) = \tfrac{1}{2} F_q \qquad \text{(II.2-5)}$$

The solution of Eq. (II.2-5) is straightforward and we obtain:

$$u_1(q) = \frac{1}{2} F_q \; \frac{D_{22}(q) - D_{12}(q)}{D_{11}(q)\, D_{22}(q) - D_{12}^2(q)}$$

$$\text{(II.2-6)}$$

$$u_2(q) = \frac{1}{2} F_q \; \frac{D_{11}(q) - D_{21}(q)}{D_{11}(q)\, D_{22}(q) - D_{12}^2(q)}$$

According to Fig. (II.2-1), the relative displacement z of the cleavage position of the two kinds of ions (subplanes) in the two surface planes is therefore given by

$$z = \tfrac{1}{2}\left(u_1(1) + u_2(1) \right) - \tfrac{1}{2}\left(u_1(0) + u_2(0) \right)$$

$$= u_1(1) + u_2(1) \; , \qquad \text{(II.2-7)}$$

while the intraplanar relative displacement δ of the two kinds of ions (subplanes) in each surface plane is given by

$$\delta = u_1(1) - u_2(1) \; . \qquad \text{(II.2-8)}$$

Using Eq. (II.2-4) and Eq. (II.2-6) in Eq. (II.2-7) we obtain,

$$z = \tfrac{1}{2} \sum_q F_q \; \frac{D_{11}(q) + D_{22}(q) - 2 D_{12}(q)}{D_{11}(q)\, D_{22}(q) - D_{12}^2(q)} \; e^{iqd} \; . \qquad \text{(II.2-9)}$$

In our particular case: $F_\ell = F\left(\delta_{\ell,1} - \delta_{\ell,0} \right)$, and imposing periodic boundary after N planes we find,

$$F_q = \frac{F}{N} \left(e^{-iqd} - 1 \right) \; . \qquad \text{(II.2-10)}$$

Figure II.2-1:   Reversible cleavage of an ionic crystal with the NaCl   structure.
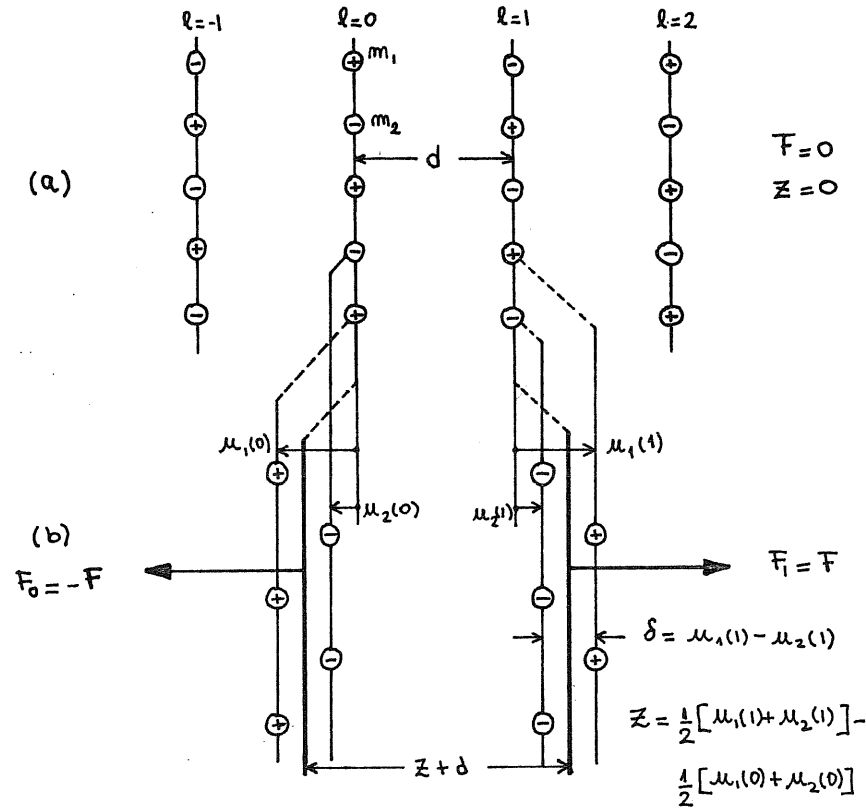
(a) Uncleaved crystal. (b) The crystal during cleavage with a spacing of $Z+d$ between

the two surface planes.

Using Eq. (II.2-10) in Eq. (II.2-9) the latter can be rewritten as

follows:

$$Z = F \frac{d}{2\pi} \int_{-\pi/d}^{\pi/d} dq \; \sin^2\left(\frac{qd}{2}\right) \; \frac{D_{11}(q) + D_{22}(q) - 2\,D_{12}(q)}{D_{11}(q)\,D_{22}(q) - D_{12}^2(q)} \; . \qquad (II.2-11)$$

where the integration extends over the first Brillouin zone for the

[100] direction.

A similar expression is obtained for δ in Eq.(II.2-8)

which reads as follows,

$$\delta = F \frac{d}{2\pi} \int_{-\pi/d}^{\pi/d} dq \; \sin^2\left(\frac{qd}{2}\right) \; \frac{D_{22}(q) - D_{11}(q)}{D_{11}(q)\,D_{22}(q) - D_{12}^2(q)} \; . \qquad (II.2-12)$$

We have obtained in Eq. (II.2-11) a formal expression for

the coefficient A in Eq. (II.2-1) which reads,

$$A^{-1} = \frac{d}{2\pi} \int_{-\pi/d}^{\pi/d} dq \; \sin^2\left(\frac{qd}{2}\right) \; \frac{D_{11}(q) + D_{22}(q) - 2\,D_{12}(q)}{D_{11}(q)\,D_{22}(q) - D_{12}^2(q)} \; . \qquad (II.2-13)$$

Unfortunately the dynamical matrix $D_{ij}(q)$ can not be

expressed in a closed form in terms of the phonon dispersion relations

(see Appendix A) as for the case of a crystal with one atom per unit

cell [63] , therefore one has to resort to some approximations in order to determine $D_{ij}(q)$ from the measured phonom spectrum.

a. 1) The dynamical matrix for a model with nearest-neighbor planes interactions only

An important simplification in the determination of the dynamical matrix $D_{ij}(q)$ arises from the electrical neutrality of the (100) planes. As shown in Appendix B , the Coulomb contribution to the force constants between a plane and its successive neighbors is easily calculated by the Madelung method, with the result that this contribution to the force constant between second neighbor planes is already 1% of that for first neighbor planes. We have therefore adopted a model for the phonom dispersion relations which includes only the force constants between subplanes in two nearest-neighbor planes.

The resulting expression for $D_{ij}(q)$ within this model (Appendix C) are:

$$D_{11}(q) = f_{12}(2+\beta) + 2f_{11}(1-\cos qd)$$

$$D_{22}(q) = f_{12}(2+\beta) + 2f_{22}(1-\cos qd) \qquad \text{(II.2-14)}$$

$$D_{12}(q) = D_{21}(q) = -f_{12}(2\cos(qd)+\beta)$$

Here f_{11} , f_{22} and f_{12} are the effective force constants between subplanes in two nearest-neighbor planes per unit area, and βf_{12} is an effective intraplanar force constant between subplanes in a given plane per unit area.

We can now determine the force constant A using Eq. (II.2-13) and Eq. (II.2-14). The resulting expression for A is the following (Appendix D):

$$A = \frac{2(f_{11}+f_{22}+f_{12})}{b/c + (1-b/c)\sqrt{a/(a-c)}} \qquad \text{(II.2-15)}$$

where

$$a = f_{12}(2+\beta)$$
$$b = 2[f_{12}-(f_{11}+f_{22})]$$
$$c = b + 2\frac{(f_{11}-f_{22})^2}{f_{11}+f_{22}+f_{12}} \quad .$$

In a similar way the coefficient of proportionality B defined through

$$\delta = B F \qquad \text{(II.2-16)}$$

can be calculated using Eq. (II.2-12) and Eq. (II.2-14), to give (Appendix D):

$$B = \frac{f_{22} - f_{11}}{a}\left(\sqrt{b/(b-a)} - 1 \right) \qquad \text{(II.2-17)}$$

where now

$$a = 4\left(f_{12}^2 - f_{11} f_{22} \right)$$

$$b = f_{12}(2+\beta)\left(f_{11} + f_{22} + 2 f_{12} \right).$$

The force constants in Eq. (II.2-14) have been determined by fitting the resulting expressions for the dispersion curves to the measured curves for acoustic and optic longitudinal phonoms in the [100] direction [64] by a least-squares procedure. Figure (II.2-2) compares the fitted and measured phonom curves for NaCl and CaO.

The calculated phonom curves are in general within 5% of the experimental values. The values of the force constants and the comparison between the fitted and experimental phonom curves are shown in Appendix E.

This simple fit to experimental data has the implicit advantage of introducing empirically an account of effects due to electronic

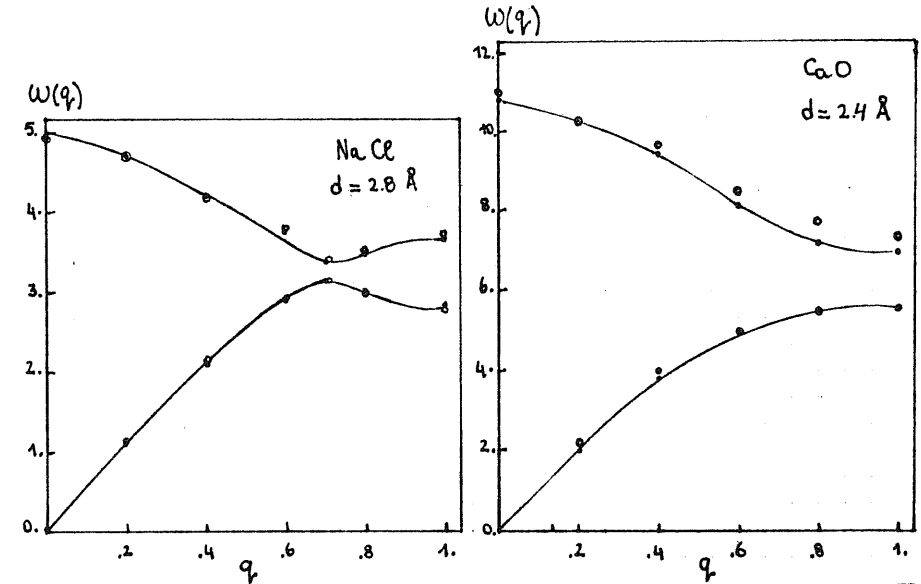Figure II.2-2:   Experimental phonom dispersion curves for longitudinal modes along the (100) direction in NaCl and CaO. The measured values are represented by open dots and were taken from [64] . The fitted dispersion relation are given by the continuous lines. The frequencies are given in 10^{13} rad/sec and the wave vectors in units of π/d .

polarization of the ions. The values for δ/z and A obtained

with this model through Eq. (II.2-17), Eq. (II.2-16), and Eq. (II.2-15) are reported in the first and second columns of Table (II.2-1).

a. 2)   A one-phonom branch approximation to A .

A further simplification of the problem can be achieved if we study the relative role of the two phonom branches in the determination of A .

By inspection of Table (II.2-1) one notices that the value of δ/z is quite small in all the cases considered, indicating that the intraplanar displacement and thus the difference between $D_{11}(q)$ and $D_{22}(q)$ play only a minor role in the initial value of the cleavage force. From this fact we are able to show after few considerations (see Appendix F), that the two-phonom branches problem can be approximately transformed into an effective one-phonom branch problem with a dispersion relation given by

$$\omega^2(q) = \Omega^2 \, \sin^2\left(\tfrac{1}{2}qd\right) , \qquad \text{(II.2-18)}$$

where the frequency Ω can be determined by fitting the measured acoustic branch near the zone center. The corresponding expression for A using Eq. (II.2-18) (Appendix F) is

$$A = \tfrac{1}{4} M \, \Omega^2 , \qquad \text{(II.2-19)}$$

where M is the mass per unit area in the (100) plane. The measured acoustic branch conforms rather closely to Eq. (II.2-18) for those crystals in Table (II.2-1) in which the two phonom branches do not cross. When crossing and splitting of the two branches occur, the value of A is largely determined by contributions from the low frequency branch near the zone center and from the high frequency branch near the zone boundary.

The values of A given by Eq. (II.2-19) are reported in Table (II.2-1) for comparison. These values are substantially the same as those given by Eq. (II.2-15).

In the same approximation we have been able to include in Table (II.2-1) also two ionic crystals with the fluorite structure for which the surface free energy for cleavage along the [111] direction is known experimentally. The effective one-phonon branch has been fitted to the measured longitudinal acoustic branch along the [111] direction [64] . The details of this calculation are summarized in Appendix G.

a. 3)   The elastic constants in the determination of A

The final simplification in the determination of A is carried out if we recall the discussion about acoustic modes and elastic constants in section (I.2-b).

If we determine Ω in Eq. (II.2-18) by the long wave limit of $\omega(q)$, we obtain:

$$\Omega = \frac{2 v_s}{d} \qquad \text{(II.2-20)}$$

	δ/z	A (10^{13} dyn /cm^3)		
		Eq.(II.2-15)	Eq.(II.2-19)	Eq.(II.2-21)
LiF (100)	0.14	5.96	5.80	5.6
NaCl (100)	0.13	1.91	1.97	1.73
KCl (100)	0.03	1.47	1.41	1.26
KBr (100)	0.11	1.16	1.42	1.05
KI (100)	0.14	0.90	0.90	0.76
MgO (100)	0.07	13.7	13.3	13.6
CaO (100)	0.12	7.46	6.31	8.0
CaF$_2$ (111)	-	-	4.54	4.12
BaF$_2$ (111)	-	-	2.62	2.52

Table II.2-1:   Properties of the cleavage force at small separations in some ionic crystals.

where v_s is the speed of longitudinal sound waves for propagation perpendicular to the cleavage plane.

Using this value of Ω in Eq. (II.2-19) and the fact that v_s can be determined from the values of the elastic constants (section (I.2-b)) the final expression for A is obtained:

$$A = \frac{\mathcal{L}}{d} \qquad (II.2-21)$$

where $\mathcal{L}$ is a suitable elastic constant, given by C_{11} for the (100)   plane and by $\frac{1}{3}\left(C_{11} + 2 C_{12} + 4 C_{44}\right)$ for the (111)   plane.

The corresponding values of A obtained with the values for the elastic constants given in Table (II.2-1) are reported in the fourth column of Table (II.2-1).

b)   Cleavage force at large separations of the crystal halves

The importance of van der Waals interactions in the calculation of the surface energy of an ionic crystal was pointed out in section (I.1-c). These interactions between the ions are in fact responsible for the attractive force between the two crystal halves at large separation

Z. In particular we consider the dipole-dipole induced force f_{ij} between the ions of types i and j derived from Eq. (I.1-7),

$$f_{ij}(R_{ij}) = \frac{6 c_{ij}}{R_{ij}^7},$$

(II.2-22)

where c_{ij} is a van der Waals coefficient for the dipole-dipole interaction. The cleavage force for large values of Z is then calculated by performing the corresponding lattice sums of those terms given in Eq. (II.2-22). These discrete lattice summations are in practice replaced by integrations as discussed in Appendix H. The cleavage force is then written as follows,

$$F = \frac{\pi}{5} n^2 \frac{C_m}{Z^3}$$

(II.2-23)

where n is the number of molecules per unit volume and C_m is an intermolecular van der Waals coefficient given by

$$C_m = C_{++} + C_{--} + 2 C_{+-}$$

(II.2-24)

for NaCl-type systems, and by

$$C_m = C_{++} + 4 C_{--} + 4 C_{+-}$$

(II.2-25)

for fluorite type systems (Appendix H). Eq. (II.2-23) thus defines the coefficient C in the expression of the cleavage force per unit area for large relative separations of the two crystal halves,

$$F = C / Z^3$$

where

(II.2-26)

$$C = \frac{\pi}{5} n^2 C_m.$$

Values of C for several ionic crystals are reported in Table (II.2-2). The van der Waals coefficients between ions where taken from Table (I.1-6). Other contributions to the force between the crystal halves, such as that due to a surface dipole layer, fall off more rapidly with increasing separation (see Appendix J).

In an attempt to find a simple empirical formula for C we can now resort to the approximate expression for the van der Waals coefficients C_{ij} given by Eq. (I.1-8),

$$C_{ij} = \frac{3}{2} \, \alpha_i \, \alpha_j \, \frac{E_i \, E_j}{E_i + E_j} \tag{I.1-8}$$

where α_i are the electronic polarizabilities of the ions and E_i are average excitation energies. Taking these energies as roughly proportional to the optical band gap E_g , i.e. $\bar{E}_i \simeq \beta E_g$ we find from Eq. (II.2-26),

$$C = \frac{3\pi}{20} \, \beta \, E_g \, (\alpha_m \, n)^2 \tag{II.2-27}$$

where α_m is the molecular polarizability and β is an empirical parameter. Use of the Clausius-Mossotti relation then yields

$$C = \frac{27}{320\pi} \, \beta E_g \left(\frac{\varepsilon_\infty - 1}{\varepsilon_\infty + 2} \right)^2 \, , \tag{II.2-28}$$

where ε_∞ is the high frequency dielectric constant of the crystal. This relation is tested in Fig. (II.2-3) by plotting the values of C given by Eq. (II.2-26), and displayed in the first row of Table (II.2-2), against the quantity $E_g \left(\frac{\varepsilon_\infty - 1}{\varepsilon_\infty + 2} \right)^2$. The

relation between C and E_g as stated in Eq. (II.2-28) is seen to be approximately verified with a reasonable value $\beta = 1.3$ for the ratio E_i/E_g. The corresponding values of C are reported in the second row of Table (II.2-2), while the full data on the E_g values and other useful quantities for some ionic crystals is summarized in Appendix K.
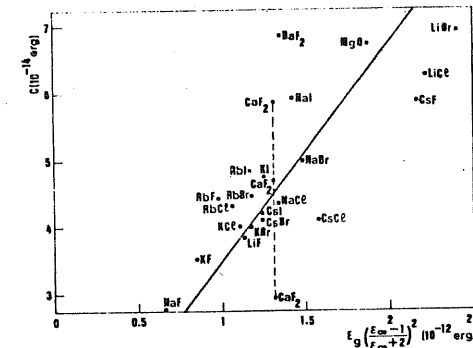
Figure II.2-3: van der Waals coefficient C versus $E_g \left(\frac{\varepsilon_\infty - 1}{\varepsilon_\infty + 2} \right)^2$ for alkali halides, MgO, CaF$_2$, and BaF$_2$. The straight line corresponds to $\beta = 1.3$ in Eq. (II.2-28). From ref. [65] . Values of ε_∞ are from ref. [15, 66, 67, 68] and the values of Eg from ref. [69, 70, 71, 72] .

$C\,(10^{-14}\,erg)$	LiF	NaCl	KCl	KBr	Ki	MgO	CaO	CaF	BaF
Eq. (II.2-26)	3.81	4.37	4.00	4.00	4.76	6.70	-	2.93/5.85	6.85
Eq. (II.2-28)	3.96	4.69	3.88	4.10	4.38	6.54	6.79	4.58	4.72

Table II.2-2:   Properties of the cleavage force at large separations of the two

crystal halves in some ionic crystals.

II.3   Surface energy from the cleavage force.

The surface energy σ can be regarded as the work done in reversibly cleaving the crystal along a crystallographic plane.

We have seen in the preceding section that for small and large separations z of the two crystal halves, the cleavage force behaves, respectively, as

$$
F(z) = \begin{cases} A\,z & (z \ll d) \\[2em] C/z^3 & (z \gg d) \end{cases} \qquad\qquad (II.3\text{-}1)
$$

where the coefficients A and C differ from material to material and can be expressed in terms of bulk properties (elastic constants, intraplanar spacing, electronic delectric constants and optical band gap).

a)   The scaled form of the cleavage force

We interpolate between the two limiting forms in Eq. (II.3-1)

for the cleavage force by assuming, as in ref. [63] , that it has the scaled form,

$$F(z) = F_0 \, f(z/z_0) \,,$$

(II.3-2)

where F_0 and z_0 contain all the dependence on the specific material, while $f(x)$ is a universal function for ionic crystals having the limiting behaviours,

$$f(x) = \begin{cases} x & (x \ll 1) \\ x^{-3} & (x \gg 1) \end{cases} .$$

(II.3-3)

The comparison of Eq. (II.3-2) with Eq. (II.3-1) gives the scaling parameters F_0 and z_0 in terms of A and C

$$z_0 = \left(C/A \right)^{1/4}$$

$$F_0 = \left(A^3 C \right)^{1/4} .$$

(II.3-4)

The surface energy σ is given in terms of $F(z)$ by,

$$\sigma = \frac{1}{2} \int_0^\infty F(z) \, dz \,,$$

(II.3-5)

where the factor $1/2$ accounts for the fact that two surfaces are created during the cleavage process. Use of Eq. (II.3-2) in Eq. (II. 3-5) gives:

$$\sigma = \alpha \left(AC \right)^{1/2}$$

(II.3-6)

where α should be a universal empirical parameter for ionic crystals [65] given by

$$\alpha = \frac{1}{2} \int_0^\infty f(x) \, dx .$$

(II.3-7)

The relation between σ and the quantity $\left(AC \right)^{1/2}$ in Eq. (II.3-6) is tested in Fig. (II.3-1) by plotting the available experimental values of the surface energies of ionic crystals (reported in Table (II.1-2) against the quantity $\left(AC \right)^{1/2}$ as determined from the values of A and C given by Eq. (II.2-21) and Eq.
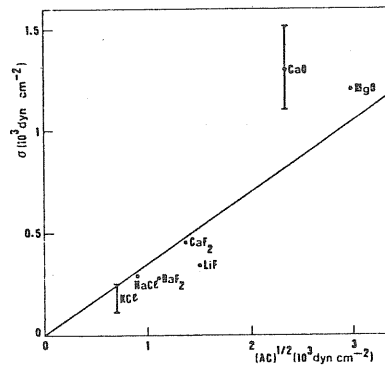
Figure II.3-1: Experimental surface energies versus $(AC)^{1/2}$. The straight line has slope $\alpha \simeq 0.35$. From ref. [65] .

(II.2-28), reported in Table (II.2-1) and Table (II.2-2), respectively. The values for σ and $(AC)^{1/2}$ thus obtained are shown in Table (II.3-1).

Although the available data are unfortunately quite scanty, the relation in Eq. (II.3-6) appears to be approximately satisfied,

	σ	$(AC)^{1/2}$
LiF	340	1490
NaCl	227 - 276	900
KCl	110 - 252	700
MgO	1200-1150-1090	2980
CaO	1310	2330
CaF$_2$	450	1370
BaF$_2$	280	1090

Table II.3-1: Experimental values of the surface energy and the cleavage force parameters ($(AC)^{1/2}$). All values are in dyn/cm^2 .

with a value of α roughly equal to 0.35. The surface energy for an ionic crystal can be written, using Eq. (II.2-21), Eq. (II.2-28) and Eq. (II.3-6) with $\alpha = 0.35$ and $\beta = 1.3$, in the following way:

$$\sigma = \sqrt{\frac{27}{320\pi}\beta\alpha^2}\left(\frac{\varepsilon_\infty-1}{\varepsilon_\infty+2}\right)\sqrt{E_g\frac{c}{d}}, \quad (II.3-8)$$

where c is the effective elastic constant for the longitudinal mode of propagation of elastic waves along the direction of reversible cleavage (see discussion to Eq. (II.2-21) and, e.g. ref. [67]), d is the interpla= nar spacing of the corresponding crystallographic planes, E_g is the optical band gap and ε_∞ the high frequency dielectric

constant of the ionic crystal. The numerical factor in Eq. (II.3-8) is $\sim$ 0.0654.

An important quantity in this simple description of the cleavage force clearly is the scaling length z_0 , which is believed [63,73] to roughly represent the separation at which $F(z)$ passes through its maximum in changing over from its initial linear increase into its final z^{-3} decay. The values of this length, which are reported in Table (II.3-2), are seen to be a remarkably constant fraction of the intraplanar spacing d , with a possible indication of a slight dependence on the cleavage plane in different structures.

	LiF	NaCl	KCl	KBr	KI	MgO	CaO	CaF	BaF
z_0/d	0.25	0.25	0.24	0.24	0.25	0.22	0.22	0.18	0.18

Table II.3-2:   Values of the scaling length z_0/d for some ionic crystals.

b)   Variation of the surface energy with the crystallographic plane

The dependence of the surface energy on the crystallographic plane enters the present approach through the value of A , i.e., through the elastic constants and the interplanar spacing (Eq. (II.3-8)).

It is easily checked form the available values of the elastic constants (see Table (I.2-1)) that it predicts $\sigma(100) < \sigma(110)$ for NaCl-type crystals, in accord with experiment. In Table (II.3-3) are compared the present results of $\sigma(100)$ and $\sigma(110)$ for NaCl according to Eq. (II.3-8) with another theoretical calculation [7] .

	experiment	(a)	(b)
$\sigma(100)$	227.-276	315	189
$\sigma(110)$	–	352	445

Table II.3-3:   Calculated surface energies for NaCl according to: (a) present work, Eq. (II.3-8); (b) From ref. [7] . All values in ergs/cm^2.

The values of $A(100) = C_{11}$ and $A(110) = \frac{1}{2}(C_{11}+C_{12}+4C_{44})$ were used in Eq. (II.3-8) to determine the surface face energies $\sigma(100)$ and $\sigma(110)$, respectively. These simple results in terms of elastic constants are not applicable, on the other hand, to charged planes such as the (111) plane in NaCl-type crystals, where the optic phonoms should be much more relevant in determining the initial value of the cleavage force.

CHAPTER III

STATES OF EXTRA ELECTRONS IN MOLTEN SALTS

CHAPTER III

States of extra electrons in molten salts

In this chapter , properties of solvated electrons at high dilution in molten alkali halides are studied theoretically [126] . For this purpose, much of the material contained in section 3 , 4 and 5 of Chapter I will be needed here . Special emphasis will be given to well known defect in ionic crystals such as the F center , discussed in section (I.3) . The discussion of the structural changes on melting of ionic crystals in section (I.4) and the theory of the structure of molten alkali halides in section (I.5) , con-stitute basic ingredients of the theory developed in this chapter .

Section (III.1) is an overview of the experimental situation regarding solutions of alkali metal (M) in molten alkali halides (MX). Thermodynamic properties, electrical conductivity experiments and optical studies of M-MX systems are recorded in this section .

Section (III.2) presents recent experimental studies on M-MX systems . Optical absorption data show new bands both in the infrared and near ultraviolet regions of the spectra . NMR experiments have added new useful information regarding the states of the extra electrons in the solution at high metal dilution . Concentration dependence studies are available for some metal--molten salt solutions .

Section (III.3) presents the theoretical model for the ground state of the solvated electron [126] . A critique of the point-like ion model previously applied to the solvated electron in molten KCl [122] is given in this section .

Section (III.4) reports the results for various properties of electronic states in the equilibrium potential well , contact with experimental data being made for ground state properties .

The main test of the present model is the calculation of the optical absorption by the solvated electron in section (III.5) . Systems other than KCl and transition to higher excited states are studied .

Ionic relaxation in the excited states and lifetime of the bound state are discussed in section (III.6) . An estimation of the electronic mobility is given .

Section (III.7) is devoted to the calculation of the modifications induced by a solvated electron in the fundamental absorption of the molten salt .

Finally , some concluding remarks are given in section (III.8).

III.1   Metal-molten salt solutions in the salt rich-region of concentration

(a)   Phase diagrams of metal-molten salt solutions.

Alkali metals dissolve in molten alkali halides to give true solutions over the whole concentration range above a certain temperature (either a consolute critical temperature or the melting temperature of the molten salt) [74] . The phase diagrams for these systems can indeed be classified into two types according to whether the critical point lies above or below the melting temperature-
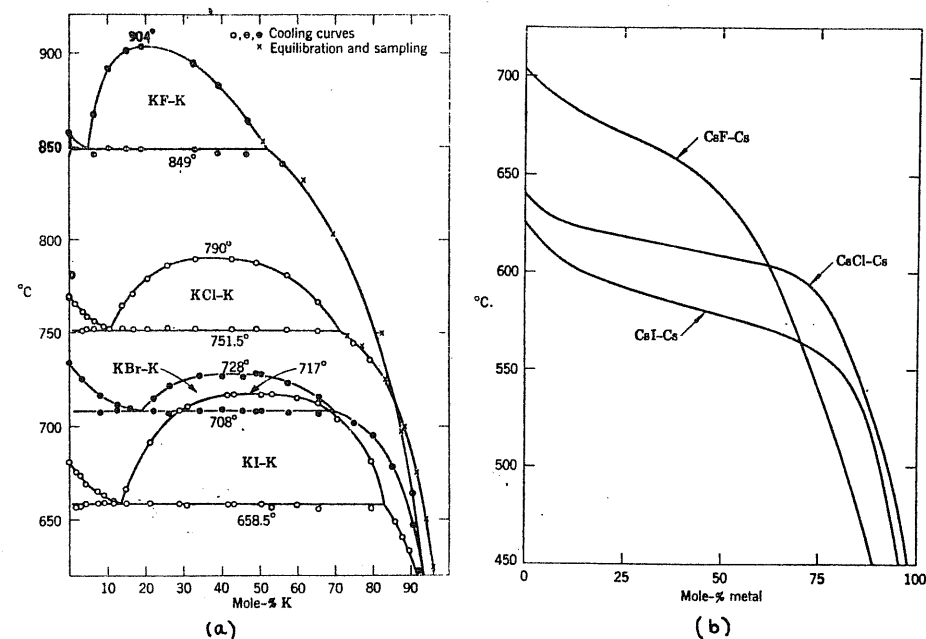

(a)   (b)

Figure III.1-1 :   Phase diagrams for (a) K - K halide and (b) Cs - Cs halide - systems .
Data from [74] .

ture of the pure salt. In the first case a miscibility gap appears up to the consolute temperature; examples being the Li, Na and K halide systems [75-80] (Fig.(III.1-1(a))). In the second case no miscibility gap is present, as in Cs-Cs halide systems (Fig.(III.1-1(b))). The Rb-Rb halide systems show an intermediate behavior [74] .
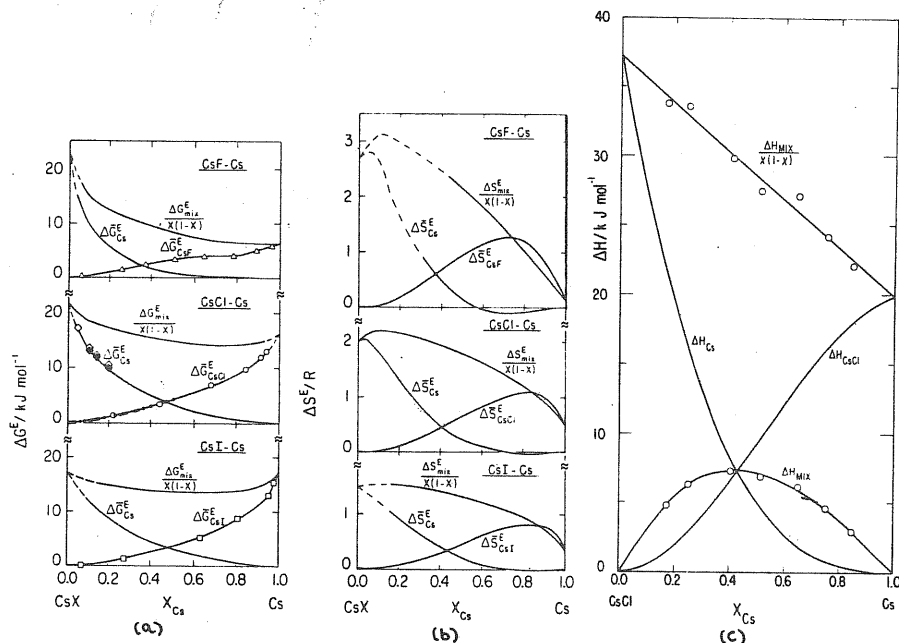

Figure III.1-2 : (a)Excess Gibbs energies of liquid Cs-CsCl mixtures at 918 °K. (b) Excess entropies of liquid Cs-CsCl mixtures at 918 °K. From 96 . (In (a): (●) from [80] and (o) from [95]). (c) Enthalpies of Cs-CsCl mixtures at 925 °K. [97] .

Excess thermodynamic quantities have been determined recently in Cs-Cs halide systems [96,97] , e.g., the enthalpies, excess Gibbs

energies and excess entropies of mixing (Fig.(III.1-2)). Measurements have also been made of metal partial vapor pressure [94] .

A remarkable point here is that the excess thermodynamic quantities of these systems exhibit rather large positive and unsymmetrical values. The only exception is the metal excess entropy near the metal-rich region of concentration ($X_M \sim 0.8$ in Cs-CsCl, Fig.(III.1-2(b))) which takes negative values, indicating a kind of local ordering of the cesium ions around the chlorine ions. The total excess entropy of mixing is, however, positive for the whole range of concentration.

A detailed analysis of the phase diagrams, for the salt-rich region of concentration [104] , shows that the orders of magnitude of the partial enthalpies and entropies are consistent with an F-center-like electron model [104] . The calculations of the excess chemical potential based on this model show, in fact, that the valence electrons from the alkali metal atoms in the solution may be considered to be a negative ion species much like the halide ions themselves. The formation of such a solution may be considered in two steps : first, the conversion of the metal to a hipothetical ionic lattice of positive ions and F-centers, and second, the random mixing with the metal halide. The energy change in the second step would be expected to be small, consequently the observed energy of mixing can be related to the excess energy of the hypothetical alkali electronide. These conclusions are consistent with the small excess enthalpies of mixing of molten alkali halides having a common cation and different anions, observed in calorimetric studies [105] . On the basis of the F-center model for the valence electron, in the infinite dilution limit of metal concentration, a value for the excess enthalpy $\Delta H_{Cs}^E = 38 \, KJ \, mol^{-1}$ is estimated for Cs in CsCl [104] ; this is in remarkably close agreement with the experimental value $\Delta H_{Cs}^E = 36.42 \, KJ \, mol^{-1}$ [97] .

(b)　　　Electrical properties of metal-molten salt solutions.

The metal-molten salt solutions above their critical points exhibit a continuous variation in the electrical conductivity with concentration. A nonmetal-to-metal transition is another interesting feature of these systems. Measurements of the electrical conductance of alkali metal-molten salt solutions [81] have been performed as a function of temperature and composition. The magnitude of the specific conductance rapidly exceeds that of the pure molten salts implying that some kind of electronic motion is superimposed on ionic conduction [78,81]. An electronic equivalent conductance, Λ_M , can be defined from the values of the equivalent conductances of the solution, Λ_{soln} , and the pure salt, Λ_{salt} , as follows [81]

$$\Lambda_M = \frac{1}{N_M} \left[\Lambda_{soln} - (1 - N_M) \Lambda_{salt} \right] , \qquad \text{(III.1-1)}$$

where N_M is the equivalent fraction of metal. Λ_M represents the change of the conductance caused by addition of one equivalent of metal to an amount of salt contained in the solution of given composition which is between two electrode plates one centimeter apart. Values of Λ_M according to Eq.(III.1-1) are plotted in Fig.(III.1-3) . Two different behaviors are displayed by these systems, with a initial drop in Λ_M for N_a systems followed, however, by a subsequent rise of Λ_M with increasing metal concentration. A relevant point here is that Λ_M
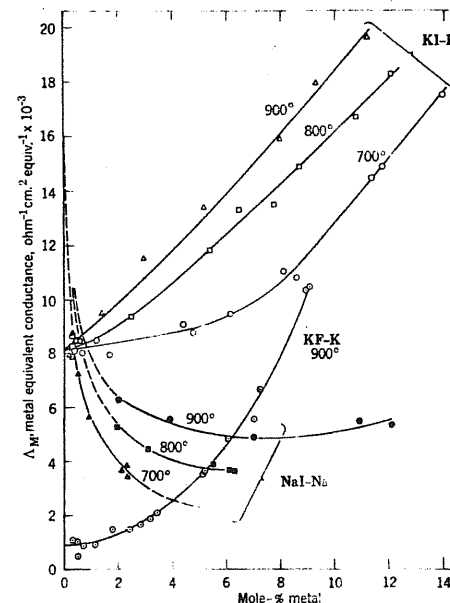
Figure III.1-3 : Apparent equivalent conductance of alkali metal dissolved in alkali halides. From ref. [74] .

takes finite values at high dilution of metal in both systems, indicating that electrons are in a state in which they can contribute to the current in the solution. The fact that Λ_M increases with temperature suggests thermally activated hopping process for the observed electronic conductivity near the salt-rich region of concentration. The values of Λ_M are found to vary continuously within the whole range of concentration.

The observed electrical conductivity in solutions of alkali metal in its molten salt (Fig.(III.1-3)) has been examined against a free-electron model for the valence electrons of the added metal [98] at low metal concentration. The mean free paths that had to be assumed to fit the experimental data [78,81] are, however, considerably less than the de Broglie wavelength. Moreover, the temperature dependence of the conductivity has the wrong sign [99].

An alternative approach takes the less implausible point of view that electrons are localized on cations [101], and that electronic conduction proceeds by a thermally activated hopping process in a random walk of the electron between atom and metal ions. The starting point is the Einstein-Nerst equation (see Eq.(I.3-1)) and Eq.(I.3-2)),

$$\mu_e = \frac{1}{6} \frac{e}{K_B T} \langle \nu R^2 \rangle = \frac{e}{6 K_B T} \int_0^\infty dR \, R^2 \, \nu(R) \, e^{-\Delta g / K_B T} P(R) , \qquad \text{(III.1-2)}$$

where Δg is the free-energy barrier associated with a composition fluctuation that leads to electron transfer, and $P(R)$ is a probability density function for finding a cation at an internuclear distance R from the metal atom. This probability function is then expressed in terms of the metal-cation pair correlation function [101]. By assuming $\Delta g \approx 4 K_B T_b$ (where T_b is the boiling point of the pure salt), for $P(R)$ a delta function centred at $R \approx 5.3 \, \text{Å}$ and $\nu(R) \sim 5 \, 10^{15} \, \text{sec}^{-1}$, it is found that $\mu_e \approx 0.08 \, \text{cm}^2/(\text{Volt sec})$, which is in order-of-magni-

tude agreement with the limiting mobilities measured [78] at infinite dilution of metal in molten salt : $\mu_e \approx 0.05, 0.06$ and $0.12 \, \text{cm}^2/(\text{Volt sec})$ for K-KCl, K-KBr and Na-NaCl, respectively. It is important to note that this hopping theory assumes that the ground state of the system is an atom in local equilibrium with anions and cations, but other possible electron traps are conceivable, such as the F-center (see section (I.3-b)) to which the essential concept of thermally activated electron transfer would apply .

A rather different model for the electronic states in solutions of metal in molten salt has been proposed which puts emphasis on the disorder of the potentials in the system [102]. The observed electronic conductivity in metal-molten salt mixtures (see Fig.(III1-3)) is then viewed as consistent with Anderson localization [103]. A consequence of this model is that fluctuations in potential associated with irregularity in the positions of the ion cores lead to localization. The essential feature of this multisite state model is based on the concept that the density of electronic states changes with increasing disorder in the system, as illustrated in Fig.(III.1-4). The energy E_c (or mobility edge) divides the regious of localized and extended states and its value depends on the amount of disorder. The electronic conductivity, σ, is then characterized by a mobility edge in these systems; this fact being consistent with the experimental results (Fig.(III.1-3)). This model is characterized by the following general hypotheses : (1) in the melt there is a low energy tail of localized states in the density of states ; (2) in the low metal concentration region only patr of the low energy region is occupied.
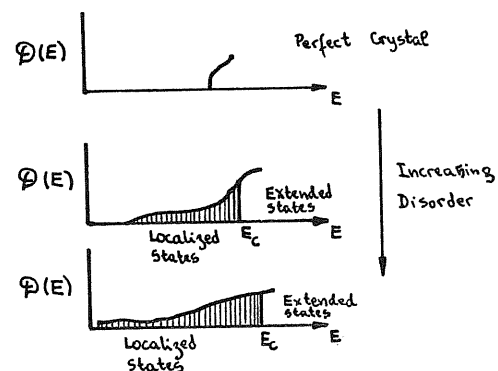
Figure III.1-4 : Change in the density of states with increasing disorder (schematic).

There is actually no obvious contradiction between the F-center

model for the very dilute region and the multisite model for the more

concentration region. Indeed, the F-center bound states may well be the

lowest electronic states in the Anderson tail below the conduction band

of the solution, and these, of course, are the only occupied states at

high metal dilution [122] .

(c)   Optical properties of metal-molten salt solutions in the

    salt-rich region of concentration.

At very low metal concentration broad optical absorption bands

have been found in spectrophotometric studies of metal-molten salt solutions

[82-90] . The results of measurements on the Na-NaCl system are shown in

Fig.(III.1-5) .
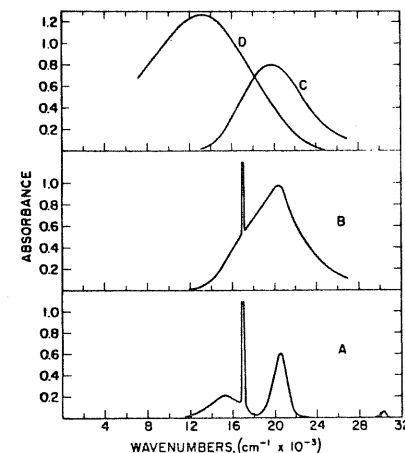
Figure III.1-5 : Absorption spectra in Na systems. (A) Na vapor ; (B) Na vapor + F-center in NaCl at 550 °C ; (C) spectrum B corrected for Na-vapor absorption ; (D) dilute solution of Na metal in liquid NaCl at 809 °C . Data from [85] .

The broad band (D) centred at $13,000 \, cm^{-1}$ $(1.61 \, ev)$ corresponds to the

dilute solution of Na metal in liquid NaCl at 809 °C . In Fig.(III.1-5)

are also plotted for comparison the spectra corresponding to Na vapor and

F-center in solid NaCl systems.

The F-band in alkali halide crystals shows a redshift with

temperature. The temperature dependence of the F-band is illustrated

in Fig.(III.1-6) which summarizes data on K-KBr system as an example .

Extrapolation of the shift of the F-center band maximum with temperature

leads to the value $1.75 \, ev$ at melting, wich is about $0.5 \, ev$

larger than the measured value $1.27 \, ev$ in the liquid. This result
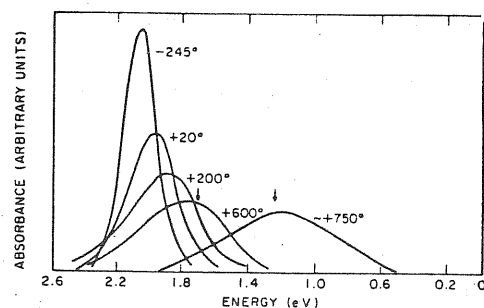
Figure III.1-6 : Temperature variation of F-center absorption in KBr. The curve at 750°C is for a solution of K in KBr. Data from ref. [82] .

is , however, consistent with the structural changes that the crystal undergoes on melting as discussed in section (I.4) . Correlation of absorption band widths and total heat content of crystalline alkali halide [106] containing F-centers and alkali metal-alkali halide melts have been discussed in the literature [100] .

Measurements have been made of the electron spin resonance [91] and magnetic susceptibility [91-93] of metal-molten salt solutions. Magnetic susceptibility studies in K-KBr [92] , Na-NaCl [93] and Cs-CsCl [108] , indicate that the molar electron susceptibility of these systems is paramagnetic and decreasing rapidly with increasing metal concentration. Estimations of the electron paramagnetic susceptibility for a localized state in the high dilution limit [107] are consistent with the experimental results [93] .

III.2   Recent data on optical absorption and magnetic properties of dilute metal-molten salt solutions

(a)   Optical absorption data.

Accurate spectroscopic studies have have been made recently on solutions of electrons in molten CsCl prepared by electrolysis or by direct addition of metal [109] . A typical spectrum before baseline correction is shown in Fig.(III.2-1) . The observed structure in the
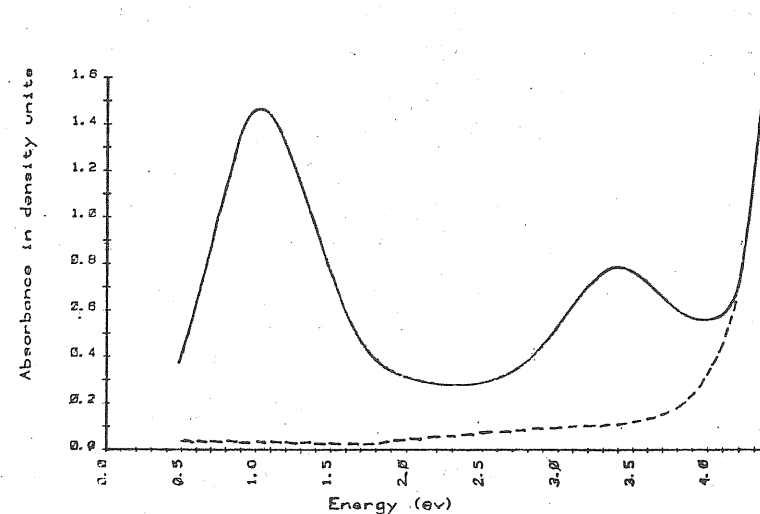
Figure III.2-1 : Absorption spectrum of electron-CsCl melt without baseline correction. The dashed line corresponds to the absorption spectrum of pure CsCl melt (baseline) . Data from ref. [109] .

spectrum is best obtained with the steady state electrolysis method of electron injection which allows good resolution in the ultraviolet. On the contrary, the UV band $(\sim 3.5\,eV)$ has not been observed in solutions prepared by direct metal addition, because the transmittance is greatly reduced in the visible and UV due to the diffusion of excess cesium into the walls of the experimental quartz cell. Boths methods, however, give the same result regarding the band in the infrared [109] . The steep rise at shorter wavelength is seen to be the long wavelength tail of the fundamental absorption band (see section (I.4-b)) of pure molten CsCl. The long wavelength edge of this band shifts to lower energies with increasing temperature as is observed in the solid state, but neither the position of the band maximum nor the band shape are reported in this experiment [109] . More recent optical studies in Na-NaBr [110] show that the fundamental absorption shift on melting is consistent with the structural changes of the system (see section (I.4-b)).

(a.1)   Mollwo-Ivey law in metal-molten salt solutions.

The energies of the band maxima (IR bands) observed in solutions of alkali metal in their molten halides plotted versus $(R_+ + R_-)^{-2}$ where $R_\pm$ are the ionic crystal radii, in Fig.(III.2-2), show remarkably accord with a Mollwo-Ivey law for the F-center band maximum in the crystal case (cf. Eq.(I.3-4)) . This simple correlation appears to provide strong support for the view that the electron has an F-center-like local environment in the molten salt . An approximate relation
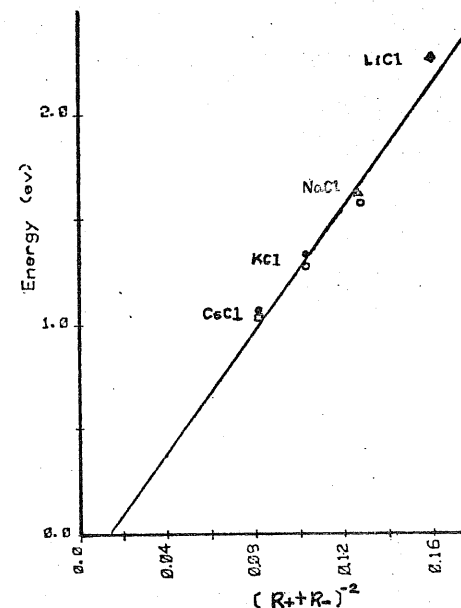
Figure III.2-2 : Absorption band maximum (Infrared bands) versus $(R_+ + R_-)^{-2}$ for alkali-alkali halide melts . (•) ref. [84] ; (o) ref. [82] ; (▲) ref. [83] ; and (□) ref. [109] . $R_\pm$ are crystal ionic radii.

can be written for the energies of the band maxima, ω_m , in terms of $(R_+ + R_-)^{-2}$ as follows,

$$\omega_m \,(eV) \simeq 13. \,(R_+ + R_-)^{-2} \,(\text{Å}) . \qquad \text{(III.2-1)}$$

In the crystal case the proportionality factor turns out to be $\sim 21. \, ev\text{-}\AA^2$ (see section (I.3-(b))).

(a.2)   The K-band.

The near infrared absorption band in CsCl is asymmetric, with a tail on its high energy side . On the low energy side, this band is well fitted by a gaussian and a progressive deviation from this shape becomes apparent for energies above about 1.35 ev (Fig.(III.2-3)) .
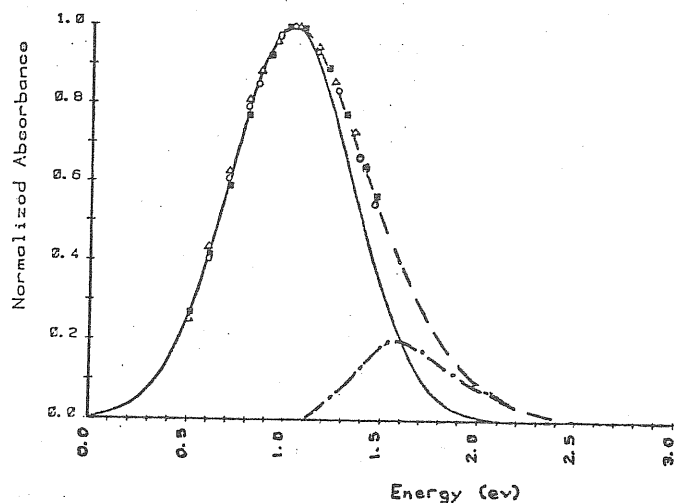
Figure III.2-3 : Resolution of the normalized infrared spectrum at 695±6 °C at low concentration into two bands . Data from [109] .

Similar deviations are found for the F-center in alkali halide crystals. In the solid case, this deviation has been attributed to higher optical transitions $(1s \rightarrow np = 3,4,\ldots)$ of the F-center (see Fig.(I.3-4)). The same kind of analysis has been applied to metal-ammonia spectra [111] .

A suggestive conclusion is attempted from Fig.(III.2-3) , in which the full measured band is resolved into two gaussian curves centred at 1.0 ev and 1.55 ev respectively . The band centred at 1.55 ev (Fig.(III.2-3)) may then be interpreted as the corresponding K band for the Cs-CsCl melt [109] . The optical data for Cs-CsCl melt are summarized in Table (III.2-1) .

Temperature (°C)	F-like band		K-like band		Area ratio (K/F)
	ω_m (ev)	$\Delta\omega$ (ev)	ω_m (ev)	$\Delta\omega$ (ev)	
695±6	1.03±0.13	0.77±.01	1.55±.02	0.63±.02	0.121
781±8 831±10 }	1.00±.015	0.79±.01	1.58±.02	0.70±.02	0.162

Table III.2-1 : Optical data for the F-like band and K-like band in dilute electron-CsCl solutions . From ref. [109] .

An estimation of the extinction coefficient of the solvated electron through a detailed analysis of Ba-doped samples of Cs-Cl was performed [109] on the assumption that each barium atom furnished two electrons to the solution . From Beer's law, a lower limit of 0.338 for the oscillator strength was obtained .

(a.3)   Temperature dependence and band width.

In Fig.(III.2-4(a)) are plotted the values of ω_m versus temperature. It is apparent that ω_m decreases with increasing temperature (redshift) and with increasing size of the cations (compare line 1,4 and 6 or 2,5 and 7) and less pronouncedly with increasing

(a)   (b)
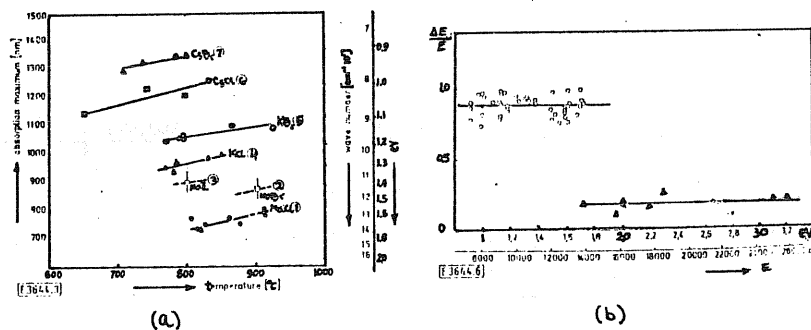
Figure III.2-4 : (a) Temperature dependence of the position of the F-band in excess alkali metal-molten salt solutions; (b) Relative band width at half maximum of the F-bands in the crystal (▲) and in the liquid (○) . Data from ref. [87] .

size of the anions (compare line 1,2 and 3 or 4 and 5 or 6 and 7 of Fig.(III.2-4(a))). In Fig.(III.2-4(b)) are displayed the relative half width at half maximum of the F-bands, $\Delta\omega / \omega_m$, in molten and solid alkali-alkali halide systems. The ratio $\Delta\omega/\omega_m$ shows a remarkable approximate constancy both in the crystal and in the liquid

case, with a value three to four times larger in the latter; this being consistent with the larger fluctuations of the ionic positions in the liquid.

(a.4)   Concentration dependence of the absorption spectra.

The NM-M transition.

The variation of the electron-CsCl spectra with electron concentration shows a number of particular features [109] . As shown in Fig.(III.2-5), the IR band shape remains unchanged at low concentration
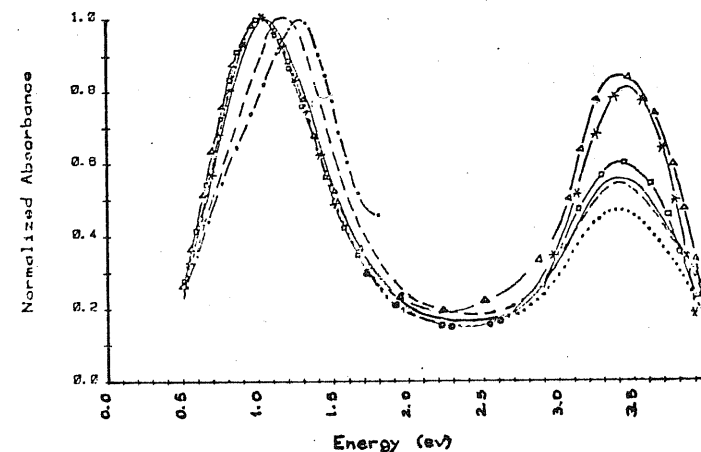
Figure III.2-5 : Absorption spectra of electron-CsCl solutions prepared by electrolysis at 695 °C with IR band normalized to unity, at different concentration. Data from [109] .

(peak absorbances below 1.5), at 695 °C . The same is found at 781°C

and 831 °C when the peak absorbance does not exceed 0.60 . At low

concentration the F-band maximum shows a redshift with temperature and

a blueshift at higher concentrations (absorbances $\gtrsim 14$).

A recent optical study of the dependence of the absorption

spectra on concentration gives an indication of the nonmetal-metal transition

in K_x-KCl_{1-x} solutions [110] . A band is observed at $\sim 2.3\,\text{ev}$ for

$X \gtrsim 0.02$, which is interpreted as an indication for the formation of

small metal clusters. A strong enhancement of the refractive index is

observed up to $X \approx 0.05$. The dielectric susceptibility calculated from

the latter follows a critical scaling law with a critical exponent which

is comparable to that in highly doped semiconductors near the NM-M

transition [112,113] . A possible analogy between the latter systems

and the M-MX solutions at low metal concentration, proposed in a different

context [114] , is consistent with the above analysis.

(a.5)   The UV band .

As shown in Fig.(III.2-5) the intensity of the UV band

varies with electron concentration, and is found that its intensity grows

with that of the F-band. This fact rules out the possibility that it is

due to impurities other than solvated electrons. It appears on the low

energy side of the CsCl fundamental absorption band, with its maximum

centred at $5.38\,\text{ev}$. This band is ascribed to the perturbation of

the fundamental band of the halide ion by the proximity of an F-center.

This attribution of the near UV band is made by analogy with a similar

band that is present in the spectrum of the alkali halide crystals that

contain F-centers, and is termed the β -band (see section (1.3.c)).

In crystalline alkali halides the ratio of the intensity of the β-band

to the F-center band is very close to unity. For the solvated electron

in CsCl melt the intensity ratio is also near to unity at low electron

concentration, but varies with rising concentration indicating a possible

dependence with the changing structure of the electron center with

concentration [109] .

(b)   Magnetic properties of metal-molten salt solutions.

(b.1)   Nuclear magnetic resonance experiments.

Nuclear magnetic resonance (NMR) studies have been performed

in Cs-CsI [115] and Cs-CsCl [116] solutions. These experiments

exploit the high sensitivity of NMR to local magnetic fields produced

at the nuclei by the spin paramagnetism of excess electrons in the metal-

molten salt solutions. If the excess electrons are not spin-paired, the

hyperfine interaction [117] leads to a time-averaged local field which

is proportional to the paramagnetic spin susceptibility. Dynamic effects,

due to the relative motions of electrons and nuclei, lead to a time-dependent

hyperfine interaction. The nuclear spin-lattice relaxation time T_1

provides an estimate for the electron-nuclei correlation time τ .

A strong peak in the relaxation rate associated with Cs^{133} in

Cs-CsCl and Cs-CsI solutions is found near 5% excess Cs [116] .

The smaller peak observed for I^{127} indicates that the paramagnetism is

most closely associated with the Cs^+ ions. The peak in the Cs rate is striking evidence for electronic localization on or near the Cs^+ ions.

Values of τ near the salt-rich region of concentration (Fig.(III.2-6)) can be estimated within an F-center model for the
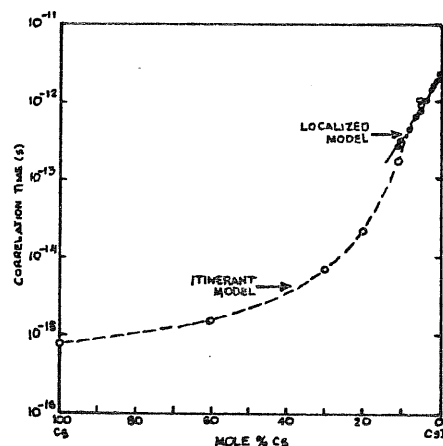
Figure III.2-6 : Experimental values of the hyperfine field correlation times (o) for in liquid Cs-CsI solutions at 640 °C. Data from [115] .

localized electronic states [115] . On the other hand, by assuming a diffusive transport process for the solvated electrons (see section (III.1-b)), with jump time τ and a root mean square jump distance $\langle a^2 \rangle^{1/2} \simeq 18. \text{Å}$ [116] , the observed electronic mobility in Cs-CsCl solutions [116] can be reproduced accurately for low metal concentration. This result shows that the hyperfine correlation time measured in the experiments [115,116] can indeed be interpreted as a jump time for the localized electrons, at low metal concentration. In this regime the electrons are

localized for times on the order of the ionic diffusion times ($\sim 10^{-12}$ sec.), but the addition of excess metal drastically increases the jump rate and leads to rapid delocalization.

Further evidence for the F-center model of localized electronic states in metal-molten salt solutions at low metal concentration, is obtained from the values of the average hyperfine coupling or, equivalently, $\langle |\psi(R_n)|^2 \rangle$. The experimental results for Cs^{133} [116] , normalized to the value $|\psi(Cs)|^2_{atom}$ atom for the $6s^1$ state of atomic Cs [118] , are the following :

$$ \frac{\langle |\psi(R_n)|^2 \rangle}{|\psi(Cs)|^2_{atom}} = \begin{cases} 0.26 & Cs-CsCl \\ \\ 0.22 & Cs-CsI \end{cases} \tag{III.2-2} $$

The average coupling per localized electron is thus much smaller than the atomic value, indicating that the excess metal does not enter the salt as a neutral atom. The above results are not consistent, for instance, with a multi-site localized states due to structural disorder [102] , in which one should expect $\langle |\psi(Cs)^2| \rangle \simeq |\psi(Cs)|^2_{atom}$ [116] , in contradiction to experiment. The results reported in Eq.(III.2-2) are found [116] to correlate with the values of ψ_F^2 determined from ENDOR experiments [119] in the alkali halide crystals containing F-centers.

(b.2)　　　Magnetic susceptibility and electron spin resonance studies.

　　　Electron spin resonance (ESR) experiments have been performed
in a number of metal-molten salt solutions [120,121] . The molar magnetic
susceptibility, $\chi_m (M)$, of dissolved alkali metal in an alkali halide
melt, is plotted in Fig.(III.2-7(a)) versus metal-concentration in the

(a)

(b)
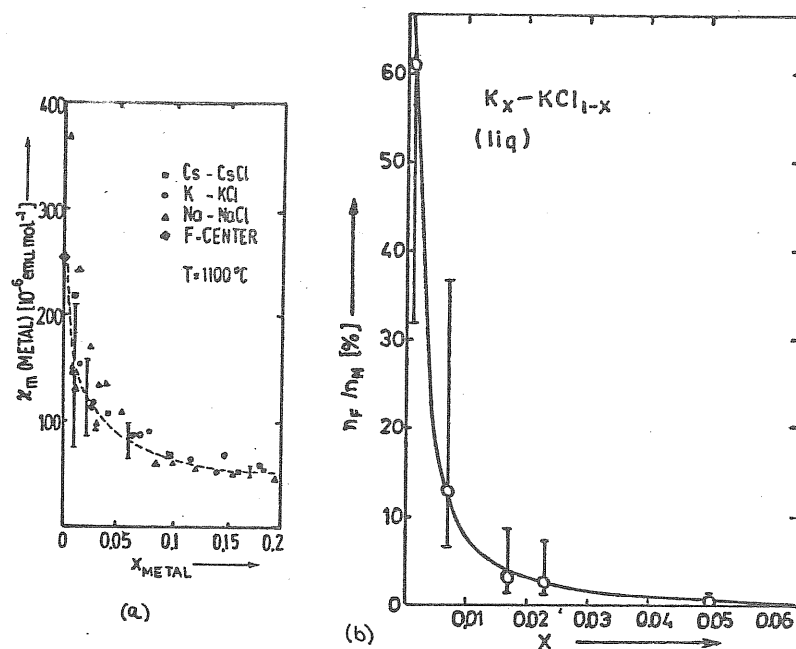
Figure III.2-7 : (a) Molar magnetic susceptibility, $\chi_m(M)$, of dissolved alkali
metal in some M-MX solutions vs. mole fraction of alkali metal, x_M . From ref. [120] .
(b) Ratio of number density of F-centers and number density of dissolved metal vs. metal
mole fraction in $K_x - KCl_{1-x}$ at 860 °C . From ref. [110] .

salt-rich region of concentration. The value for $\chi_m(M)$ according to the F-center
model for a solvated electron in a molten salt [122] , agrees remarkably
well with the experimental data.

　　　The initial drop in $\chi_m(M)$ with increasing metal concentration
is an indication that spin-paired localized states play an important role.
This fact is consistent with the observed decrease in the number of F-centers
with concentration (Fig.(III.2-7(b))), as determined from the absorption
constants [110] and from the Smakula equation (cf. Eq.(I.3-5)).

　　　Finally the magnitude of the g-factor shift, Δg ,observed
in metal-molten salt solutions at low metal concentration [120] is comparable
with that found for the F-center shift in the alkali halide crystals [123] .
Estimates of Δg have been performed for the crystal case considering
the ground state wave function of the F-center to be an admixture of s
and p functions [124] (see also [125]).

III.3   Theory of the ground state of the solvated electron.

(a)   The ground state potential.

The model for the solvated electron in a molten alkali halide has been proposed previously (model I) by taking the structure of the ionic liquid into account [122] . It is considered here, as in model I, a hard bubble of diameter σ in a liquid of charged hard spheres of diameters $\bar{\sigma} = \frac{1}{2}(\sigma_+ + \sigma_-)$, σ_+ and σ_- being ionic diameters determined from the compressibility of the pure molten salt [122] . Let $P_{1S}(r)$ be the probability of finding the electron within a distance r from the centre of the bubble, i.e.

$$P_{1S}(r) = \int d\Omega \int_0^r ds\, s^2 \left| \Psi_{1S}(\underline{s}) \right|^2 , \qquad (III.3-1)$$

where $\Psi_{1S}(\underline{r})$ is the ground-state wave function. A charge $-eP_{1S}(R)$ is then attributed to the bubble, with $R = \frac{1}{2}(\sigma + \bar{\sigma})$ being the distance of closest approach of the ions to the centre of the bubble. A distribution of values of R , around a value R_0 to be determined by minimizing the free energy (see paragraph (b) of this section), is envisaged to account for liquid-state spherosymmetric fluctuations with probability determined by the corresponding increase of free energy.

The potential $V(r)$ felt by the electron, for given R and $P_{1S}(R)$, according to model I , was evaluated by adopting a

polarizable-point-ion approximation for the electron-ion interactions and the mean spherical approximation (MSA) [50] (see section (I.5)) for the structure of a charged-hard-spheres liquid . The potential is estimated by a semicontinuum Hartree-Fock method, in analogy with previous work on the F-center in the crystal [131] . The point-ion potential, $V_{pi}(r)$, is flat within the sphere of radius R , $V_{pi}(r) = V_{in}$ for $r < R$, and is made of two terms : $V_{in} = V_{coul} + V_{pol}$, where V_{coul} is the Coulomb contribution and V_{pol} the core-polarization term . The potential for $r > R$, V_{out} , is taken in the form of a screened Coulomb potential . Fig.(III.3-1) shows a typical plot of $V_{pi}(r)$, taken from [122] for the KCl case .
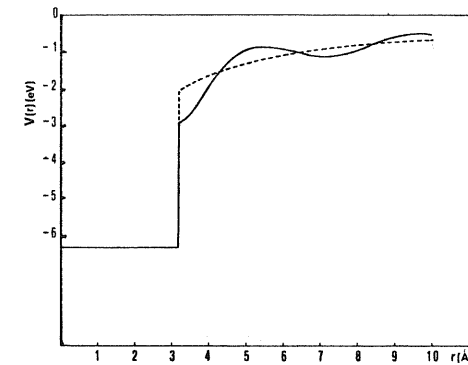
Figure III.3-1 : Potential well for a solvated elevtron in KCl according to the point-ion model . $R = 3.2$ Å and $P_{1S}(R) = 1.$. Data from [122] .

The Coulomb contribution to the potential V_{in} can be written as follows

$$V_{coul} = -e^2 P_{is}(R) \int_R^\infty dr \; 4\pi r \rho \left(g_{+c}(r) - g_{-c}(r) \right), \qquad \text{(III.3-2)}$$

where $g_{+c}(r)$ and $g_{-c}(r)$ are the pair distribution functions between the center of the bubble with unit charge and the two ionic species, and ρ is the number density of the pure molten salt . The core-polarization term, V_{pol} , vanishes if $P_{is}(R) = 1$ and is taken to have the Hartree-Fock expression,

$$V_{pol} = \left(1 - \frac{1}{\varepsilon_\infty} \right) e^2 \int_R^\infty \frac{(1 - P_{is}(r))}{r^2} dr \qquad \text{(III.3-3)}$$

where ε_∞ is the high-frequency dielectric constant of the solvent .

The MSA [50] yields an analytic expression for the quantity given in Eq.(III.3-2) , which in the present case (infinite dilution limit) reads (Appendix L)

$$V_{coul} = -\frac{2e^2 \Gamma}{1 + \Gamma \sigma} P_{is}(R) = -U_0 P_{is}(R), \qquad \text{(III.3-4)}$$

where Γ is a parameter of the solvent determined by Eq.(III.3-14) below . The expression for V_{pol} in Eq.(III.3-3) can be rewritten in the following way

$$V_{pol} = (1 - 1/\varepsilon_\infty) \frac{e^2}{R} \left[(1 - P_{is}(R)) - R P_{r_{is}}(R) \right], \qquad \text{(III.3-5)}$$

where

$$P_{r_{is}}(R) = 4\pi \int_R^\infty \frac{r^2 \, |\psi_{is}(r)|^2}{r} dr . \qquad \text{(III.3-6)}$$

The potential for $r > R$, V_{out} , is written in terms of the pair correlation functions $g_{\pm c}$ as

$$V_{out} = -\frac{e^2}{\varepsilon_\infty} \rho \, P_{is}(R) \int d\underline{s} \left[g_{+c}(s) - g_{-c}(s) \right] \frac{1}{|\underline{r} - \underline{s}|} . \qquad \text{(III.3-7)}$$

The MSA gives again an analytic expression for V_{out} [48] which can be shown (Appendix L) to read

$$V_{out} = -\frac{U_0}{\varepsilon_\infty} \frac{(1 + \Gamma \bar{\sigma})}{\Gamma r} P_{is}(R) \; \phi(n \bar{\sigma}) \qquad \text{(III.3-8)}$$

for $(n-1)\bar{\sigma} \leqslant (r-R) \leqslant n \bar{\sigma}$, with $n > 0$,

where $\emptyset(n\,\bar{\sigma})$ is an oscillating function given by Eq.(L.9) of Appendix L.

In summary, the potential $V_{pi}(r)$, according to model I, can be written as follows :

$$V_{pi}(r) = \begin{cases} -U_0\, P_{1s}(R) + \left(1 - \dfrac{1}{\epsilon_\infty}\right) e^2 \displaystyle\int_R^\infty \dfrac{1 - P_{1s}(r)}{r^2}\, dr \; , & (r < R) \qquad \text{(III.3-9a)} \\[3mm] -\dfrac{e^2}{\epsilon_\infty}\, P_{1s}(R) \displaystyle\int d\underset{\sim}{s} \left[g_{+c}(s) - g_{-c}(s) \right] \dfrac{1}{|\underset{\sim}{r} - \underset{\sim}{s}|} & (r > R) \qquad \text{(III.3-9b)} \end{cases}$$

Selfconsistency is achieved through the dependence of $V(r)$ on $P_{1s}(r)$, this latter function being itself to be determined by solving the Schröedinger equation with given $V(r)$. A factor $P_{1s}(R)$ has been made explicit in the potential $V_{pi}(r)$ in Eq.(III.3-9b) , showing that the calculation will selfconsistently allow the disappearance of the long-range Coulomb attraction of the electron to the bubble as the electron becomes delocalized.

The results of model I [122] show that this approach over-estimates somewhat the peak frequency of the $1s \rightarrow 2p$ absorption band in KCl and underestimates greatly the band width, the latter arising in the theory from the fluctuations in the cavity radius . This suggests an overestimate of the depth of the potential well in Eq.(III.3-9a) and of the local rigidity of the system [126] . Likely causes for this are the neglect of non-Coulombic interactions between the electron and the ionic cores and the schematization of the electronic bubble through a hard-sphere boundary condition on ionic fluctuations, these deficiencies concerning mainly the first-neighbor shell of alkali ions.

In order to remedy these defects in a still viable self-consistent

calculation, a constant repulsive potential inside the cavity is empirically added to Eq.(III.3-9a) . One thus write $V(r)$ [126] as

$$V(r) = V_{pi}(r) + V_{rep}\, \theta(R-r) \; , \qquad \text{(III.3-10)}$$

where $\theta(R-r)$ is the Heaviside step function and V_{rep} is a parameter to be determined from experimental data on the solvated electron. One can see from the foregoing discussion a strong dependence of this parameter on the positive ion .

As will be discussed more fully in section (III.5) below, it is estimated from the optical absorption data a value $V_{rep} \simeq 0.7$ ev for KCl , rising to $V_{rep} \simeq 1.1$ ev for CsCl through a dependence on the alkali ion roughly of the type $V_{rep} \propto \sigma_+^{-3}$. At the present time there is not an independent test of these magnitudes, although they do not seem unreasonable in the light of all the following calculations .

(b)   The free energy.

An analytic expression for the Helmholtz free energy of an n-component mixture of charged hard spheres is yielded by the MSA . It consists of a hard-sphere contribution and a Coulomb contribution:

$$F(V,T) = F_{hs} + F_{coul} \; . \qquad \text{(III.3-11)}$$

The expression for F_{hs} is obtained by integrating the virial pressure for a neutral-hard-sphere fluid,

$$F_{hs} = F_{id} + \frac{6}{\pi} V K_B T \left[\frac{3 \xi_1 \xi_2}{\Delta} + \frac{3 \xi_2^3}{\xi_3 \Delta} + \frac{3 \xi_2^3}{\xi_3^2} \ln \Delta - \xi_0 \ln \Delta \right], \qquad (III.3-12)$$

with $\xi_n = \frac{\pi}{6} \sum_\alpha \rho_\alpha \sigma_\alpha^m$ and $\Delta = 1 - \xi_3$, and for F_{coul} by integrating the excess internal energy [50] ,

$$F_{coul} = V K_B T \frac{\Gamma^3}{3\pi} - V e^2 \left(\Gamma \sum_\alpha \frac{\rho_\alpha z_\alpha^2}{1 + \Gamma \sigma_\alpha} + \frac{\pi}{2\Delta} \Omega P_n^2 \right). \qquad (III.3-13)$$

Here the charges, partial densities and diameters of the component species are $z_\alpha |e|$, ρ_α and σ_α respectively; Γ is to be determined by solving the algebraic equation

$$\Gamma = \left(\frac{\pi e^2}{K_B T} \right)^{1/2} \left[\sum_\alpha \rho_\alpha \left(\frac{z_\alpha - \frac{1}{2}\pi P_n \sigma_\alpha^2 / \Delta}{1 + \Gamma \sigma_\alpha} \right)^2 \right]^{1/2}, \qquad (III.3-14)$$

and the quantities Ω and P_n have simple expression in terms of the quantities defined above [50] ,in particular $P_n = 0$ for equi-sized ions . In the present case, components 1 and 2 of the fluid represent the alkali and halogen ions, and component 3 represents electronic bubbles

with diameter $\sigma_3 = \sigma$ and valence $z_3 = -\rho_0(R)$.

The relevant σ-dependent term in the free energy, to first order in ρ_3 ,is the chemical potential μ_e of the electronic bubble which can be written [122] as

$$\mu_e(R) = \mu_e^{hs} + \mu_e^{coul} + \mu_e^{pol} + E_0(R). \qquad (III.3-15)$$

Core polarization effects are accounted for through the term μ_e^{pol} and the internal degrees of freedom of the electronic bubble through $E_0(R)$. The latter is the energy of the electronic ground state relative to the bottom of the potential well binding the electron, determined by the solution of the solution of the Schrödinger equation as described in the preceding paragraph . The expressions for μ_e^{hs} and μ_e^{coul} are obtained by differentation of Eq.(III.3-12) and Eq.(III.3-13) in the limit $\rho_3 \to 0$; one thus obtains for equi-sized ions of diameter $\bar{\sigma}$,

$$
\begin{aligned}
\mu_e^{hs} = \mu_{id} &- K_B T \ln \Delta + K_B T \left[\pi \rho \frac{\bar{\sigma}^2}{\Delta} \right] \sigma \\
&+ K_B T \left[4\pi \frac{\rho \bar{\sigma}}{\Delta} + \frac{9}{\bar{\sigma}^2} \ln \Delta \right] \sigma^2 \\
&+ K_B T \left[\frac{\pi}{3} \rho (1 - \frac{6}{\Delta}) + \frac{6}{\Delta^2} (\frac{\pi}{3})^2 \rho^2 \bar{\sigma}^3 - \frac{6}{\bar{\sigma}^3} \ln \Delta \right] \sigma^3
\end{aligned}
\qquad (III.3-16)
$$

and

$$\mu_e^{coul} = - \frac{e^2 \Gamma}{1 + \Gamma \sigma} P_{15}^2(R), \qquad (III.3-17)$$

where the quantities Γ and Δ now refer to the pure salvent . In particular, $\Gamma = \frac{1}{2\bar{\sigma}}\left(\sqrt{1+2x^2} - 1\right)$ with $x^2 = 8\pi e^2 \rho \bar{\sigma}^2/K_B T$ and $\Delta = 1 - \frac{\pi}{3} \rho \bar{\sigma}^3$.

The core polarization term μ_e^{Pol} can be estimated by considering the polarization work involved in replacing a halogen ion by the electronic bubble in an adiabatic process [122] . A continuous dielectric calculation yields

$$\mu_e^{Pol} = \left(1 - \frac{1}{\varepsilon_\infty}\right) e^2 \int_R^\infty \left[1 - \frac{1}{2} P_{1s}(r)\right] P_{1s}(r) \; \frac{dr}{r^2} , \qquad (III.3-18)$$

which represents the polarization work involved in bringing $P_{1s}(R)$ adiabatically from zero to its actual value in the polarization potential of the medium .

The equilibrium value of R , denoted by R_0 , will be determined by minimizing $\mu_e(R)$ in Eq.(III.3-15) .

III.4   Equilibrium ground states and energy levels.

The radial Schröedinger equation with a potential $V(r)$ given by Eq.(III.3-10) was solved selfconsistently for several values of R and for four molten alkali halides (NaCl, KCl, KBr and CsCl) . Table (III.4-1) presents the imput parameters of the calculation for the four molten salts and the values of R_0 which correspond to the minimum of the free energy (cf. Eq.(III.3-15)) in these systems .

	$N_a Cl$	KCl	KBr	$C_s Cl$
$T \; [^\circ K]$	1081	1049	1013	973
$\rho \; (10^{-2} \mathring{A}^{-3})$	1.60	1.23	1.07	0.98
ε_∞	2.34	2.19	2.34	2.62
$\sigma_+ (\mathring{A})$	2.24	2.79	2.80	3.32
$\sigma_- (\mathring{A})$	3.04	3.05	3.31	3.10
$\Gamma \; (\mathring{A}^{-1})$	1.05	0.94	0.89	0.86
$V_{rep} (ev)$	0.34	0.70	0.70	1.10
$R_0 (\mathring{A})$	3.10	3.18	3.29	3.23
$V(0)\big|_{R_0} (ev)$	−4.60	−3.98	−4.02	−3.64

Table III.4-1 : Input parameters and equilibrium values of cavity radius and well depth. Values of ρ from [132] ; ε_∞ from [66] ; σ_+ , σ_- from [122] .

The last row of Table(III.4-1) reports the equilibrium values of the depth

of the potential well $V(o) = V_{p_i}(o) + V_{rep}$. The full result of the calculations

for all the chosen values of R and for the four molten salts are reported

in Appendix M . It contains the corresponding values of $\mu_e(R)$ (cf.

Eq.(III.3-15)) , the selfconsistent quantities entering the potential $V(r)$

(see Eq.(III.3-9)) and the energy levels for the ground state and the

first two excited states (2p and 3p states) .

In Fig.(III.4-1) are plotted the radial probability distributions
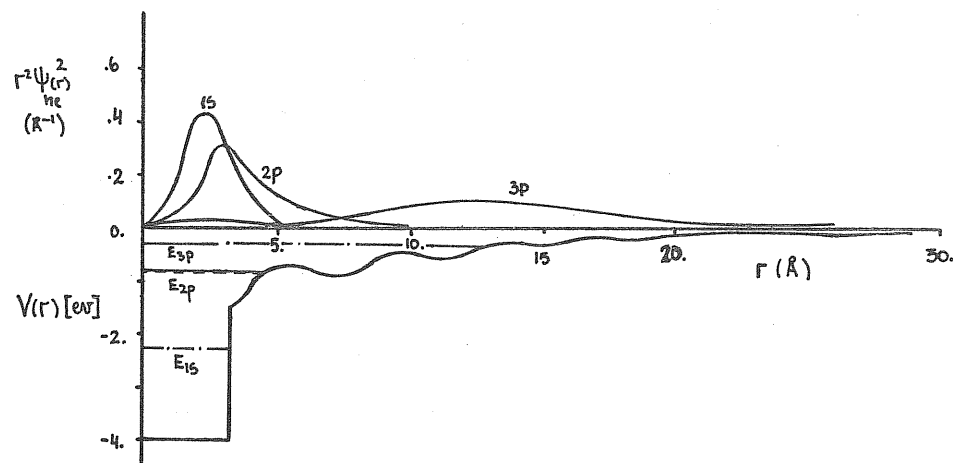
Figure III.4-1 : Radial probability distributions for the ground state ψ_{1s} and the ψ_{2p}
and ψ_{3p} excited states in KCl : $V(o) = -3.98$ ev and $R_o = 3.18$ Å .
The corresponding energy levels (ev) are also indicated .

for the ground state (1s) and for the 2p and 3p excited states obtained

for KCl . All these states were calculated in the ground state selfconsis-

tent potential well (cf. Eq.(III.3-10)) .

Table (III.4-2) presents results for the ground state in the

equilibrium potential well and for the 2p and 3p excited states in the

same potential well . These properties are the probabilities

	N_aCl	KCl	KBr	$CsCl$
$P_{1s}(R_o)$	0.79	0.75	0.78	0.74
$P_{2p}(R_o)$	0.47	0.39	0.45	0.36
$P_{3p}(R_o)$	0.024	0.03	0.025	0.027
$E_{1s}(R_o)$ (ev)	-2.65	-2.24	-2.33	-1.96
$E_{2p}(R_o)$ (ev)	-0.96	-0.79	-0.87	-0.59
$E_{3p}(R_o)$ (ev)	-0.25	-0.24	-0.24	-0.18
$(\langle r^2 \rangle_{1s})^{1/2}$ (Å)	2.58	2.78	2.78	2.85
$(\langle r^2 \rangle_{2p})^{1/2}$ (Å)	3.85	4.39	4.13	4.75
$(\langle r^2 \rangle_{3p})^{1/2}$ (Å)	14.4	15.1	15.0	17.1
$\lvert \psi_{1s}(+)\rvert^2 (10^{-3}Å^{-3})$	2.2	2.2	1.9	2.1
$\lvert \psi_{1s}(-)\rvert^2 (10^{-5}Å^{-3})$	8.0	4.4	4.3	5.3

Table III.4-2 : Properties of electronic states in equilibrium well . From ref. [126] .

of finding the electron within the cavity radius in the various states, the energy levels $E_{n\ell}(R_0)$ and the mean square distances $\langle r^2 \rangle$ of the electron from the center of the cavity . For the ground state are also given the values of $|\psi_{1s}(r)|^2$ at the peak of the first neighbor (cation) and of the second neighbor (anion) distributions .

It is apparent from Table (III.4-2) that the 1s state is rather strongly localized inside the well; whereas the 2p state is appreciably spread out and the 3p state is almost completely delocalized (see Fig. (III.4-1)) . In this sense, the inclusion of a repulsive term of the presently assumed magnitude is not changing the qualitative conclusions obtained with the model I [122] , but is only affecting the quantitative details . On the other hand, it is found in the present calculations that if $P_{1s}(R)$ were to decrease to a value of order 0.6 , the bound state would tend to dissolve in the course of the subsequent steps to selfconsistency . To be more precise, by starting with any input value for $P_{1s}(R)$ ($P_{1s}(R) \sim 1.$,say) the new obtained values of $P_{1s}(R)$ are always smaller than the previous one and finally reach the value $P_{1s} = 0$. This is found to happen, for values of V_{rep} somewhat larger than 1 ev , under relatively large fluctuations of R away from the equilibrium value R_0 . The conclusion here is that large spherosymmetric fluctuations may lead to delocalization of the solvated electron . A more likely cause for finite lifetime of the bound state will be discussed in section (III.6) .

The calculated properties of the ground state in Table (III.4-2) can be brought into contact with experimental data . First of all, one can evaluate from the value of $\langle r^2 \rangle_{1s}$ the diamagnetic contribution to the excess magnetic susceptibility χ of dilute metal-molten salt solutions . If one assumes that the paramagnetic contribution to χ is given by the classical Curie expression, one thus has (see for instance [67]) that

$$\chi(T) = N_0 \left[\frac{g^2 \mu_B^2}{4 k_B T} - \frac{1}{6} \frac{e^2}{m c^2} \langle r^2 \rangle_{1s} \right], \qquad (III.4-1)$$

where g is the electronic g-factor (g =2.0023) , μ_B the Bohr magnetism and N_0 the Avogadro's number . It turns out that the diamagnetic contribution to χ is only of the order of 10-20 % . The total excess susceptibility given by Eq.(III.4-1) is estimated to be $\chi \simeq 250 \cdot 10^{-6}$ emu/mol at 1100 °C for all the systems considered here as is apparent from Table (III.4-3) . This value is consistent with the available

	$NaCl$	KCl	KBr	$CsCl$
Curie term	273.	273.	273.	273.
Diamagnetic	-19.	-22.	-22.	-23.
$\chi(T)$	254.	251.	251.	250.

Table III.4-3 : Excess magnetic susceptibility of dilute metal-molten salt solutions according to Eq.(III.4-1) . χ in $[10^{-6}$ emu/mol$]$.

experimental evidence [120,121] (see Fig.(III.2-7)) .

Contact can also be made with NMR experiments [115,116] on molten CsCl , which through measurements of hyperfine shifts have yielded values for the electron density on a cesium nucleus and on a chlorine nucleus in this system at small concentration of added metal (see section (III.2-b.1)). One needs for this purpose to know the detailed nature of the true wave function of the solvated electron inside the ionic cores . In work on the

crystal it was shown [131] that this function can be constructed by ortho-
gonalizing the smooth wave function $\psi_{1s}(\underline{r})$ to the core orbitals . This
involves, in practice, the multiplication of $|\psi_{1s}(+)|^2$ and $|\psi_{1s}(-)|^2$
by factors determined by the atomic number of the species [133] . These
factors are estimated in Appendix N using new theoretical calculations
regarding the crystal F-center and are compared with those of ref. [133] .
Assuming the same factors for the solvated electron in the liquid, it is
found for the contact electron densities values of order $3. \mathring{A}^{-3}$ for the
cesium nucleus and $0.04 \mathring{A}^{-3}$ for the chlorine nucleus in CSCl . These
values are to be compared with those reported in Eq.(III.2-2) [116] .
A careful analysis of the experimental data, performed in Appendix N ,
shows that the above theoretical estimations of $|\psi_{1s}(+)|^2$ and $|\psi_{1s}(-)|^2$
are of the same magnitude as those extracted from the NMR evidence [116] .

Finally, with regard to the results for excited states in Table
(III.4-2) , their evaluation in the undeformed potential appropriate to the
1s state is clearly aimed at a tratment of optical transitions as Franck-
Condon process . This is the subject of the next section . The effect of
allowing for a relaxation of core polarization in the 2p state was estimated
using model I [122] to be small, of order 0.1 ev in $E_{2p}(R_0)$. This
effect is probably larger in the 3p state but hard to estimate with any
reliability .

III.5   Optical absorption by the solvated electron.

The energy of a Franck-Condon transition between the 1s and the
2p state, for a given value of the cavity radius R , is given by

$$\omega_{1s \to 2p}(R) = E_{2p}(R) - E_{1s}(R) , \qquad \text{(III.5-1)}$$

with a similar expression for the 1s $\to$ 3p transition . These energies
for $R = R_0$ can be obtained from Table (III.4-2) and for other values
of R from results of Appendix M .

It is then assumed that the liquid-state fluctuations determine
a distribution of values for R around its equilibrium value R_0 , with
probability $P(R)$ given by the free energy increase [122]

$$P(R) = \frac{1}{P_0} \operatorname{Exp} \left\{ - \left[\mu_e(R) - \mu_e(R_0) \right] / K_B T \right\} , \qquad \text{(III.5-2)}$$

where P_0 is a normalization factor and $\mu_e(R)$ is given by Eq.(III.3-15).
These fluctuations broaden the transition into a band, with finite width and
shifted peak frequency . The transition probability (by unit volume V and
unit length L) at energy ω by electrons in bubbles with diameter
between R and $R + dR$ is [134,122]

$$dW_{1s \to 2p}(\omega) = \frac{4\pi^2 e^2}{3\hbar} \frac{\omega}{V} |\underset{\sim}{r}_{1s \to 2p}|^2 P(R) \delta(\omega(R) - \omega) \frac{dR}{L} \qquad \text{(III.5-3)}$$

where $|\underset{\sim}{r}_{1s \to 2p}|^2$ is the electric dipole matrix element defined as

$$\underset{\sim}{r}_{1s \to 2p} = \int d\underset{\sim}{r} \; \psi_{1s}(r) \; \underset{\sim}{r} \; \psi_{2p}(r) . \qquad \text{(III.5-4)}$$

Inversion of Eq.(III.5-1) to obtain a function $R(\omega)$ and integration of Eq.(III.5-3) over R together yield the absorption intensity 134

$$I(\omega) = \frac{4\pi^2 e^2}{3\hbar c} \frac{\omega}{V} |\underset{\sim}{r}_{1s \to 2p}|^2 P(R(\omega)) \left| \frac{dR(\omega)}{d\omega} \right| \frac{1}{L} \qquad \text{(III.5-5)}$$

$$= \frac{4\pi^2 e^2}{3\hbar c} I^0(\omega)$$

Using the definition of the oscillator strength $f_{1s \to 2p}(\omega)$ [134]

$$f_{1s \to 2p}(\omega) = \frac{4\pi^2}{3\hbar} \omega |\underset{\sim}{r}_{1s \to 2p}|^2 \frac{m}{2\pi^2 \hbar} \qquad \text{(III.5-6)}$$

Eq.(III.5-5) can be rewritten as

$$I(\omega) = \frac{2\pi^2 e^2 \hbar}{mc V} f_{1s \to 2p}(\omega) P(R(\omega)) \left| \frac{dR(\omega)}{d\omega} \right| \frac{1}{L} . \qquad \text{(III.5-7)}$$

The value of the oscillator strength for the 1s $\to$ 2p transition is obtained [134] by integrating Eq.(III.5-7) over the whole range of energies ω ,

$$\bar{f}_{1s \to 2p} = \frac{mcV}{2\pi^2 \hbar e^2} \int d\omega \; I(\omega) = \frac{1}{L} \int f(\omega) P(R(\omega)) \left| \frac{dR(\omega)}{d\omega} \right| d\omega . \qquad \text{(III.5-8)}$$

Using the definition of $I^0(\omega)$ and Eq.(III.5-6) together in Eq.(III.5-8) one obtains

$$\bar{f}_{1s \to 2p} = \frac{V}{3 R_y a_B^2} \int I^0(\omega) \; d\omega , \qquad \text{(III.5-9)}$$

where $R_y = 13.6 \, ev$ and a_B is the Bohr radius . A similar treatment is given for the 1s $\to$ 3p transition .

The calculated bands for molten CsCl are plotted in Fig.(III.5-1). As become apparent from the figure, the absorption bands have a somewhat asymmetric gaussian-like shape with a high-frequency tail . These results should be compared with the measured spectrum [109] reported in Fig.(III.2-3). There, the 1s $\to$ 2p band is found to be centerd at $\omega_m \simeq 1. \, ev$ ($\Delta\omega = 0.77 \, ev$) while the K-band is estimated to be at $\omega_m \simeq 1.55$ ($\Delta\omega = 0.63 \, ev$).

The calculated values of the peak frequencies ω_m , the full widths $\Delta\omega$ at half maximum, the square dipole matrix elements $|\underset{\sim}{r}_{ke}(R_e)|^2$ and the oscillator strengths for the two bands are reported in Table(III.5-1) for the four molten alkali halides considered here . The oscillator strengths were evaluated by using Eq.(III.5-9) . The ratio between $f_{1s \to 3p} / f_{1s \to 2p}$ gives directly the ratio between the areas under the corresponding bands .
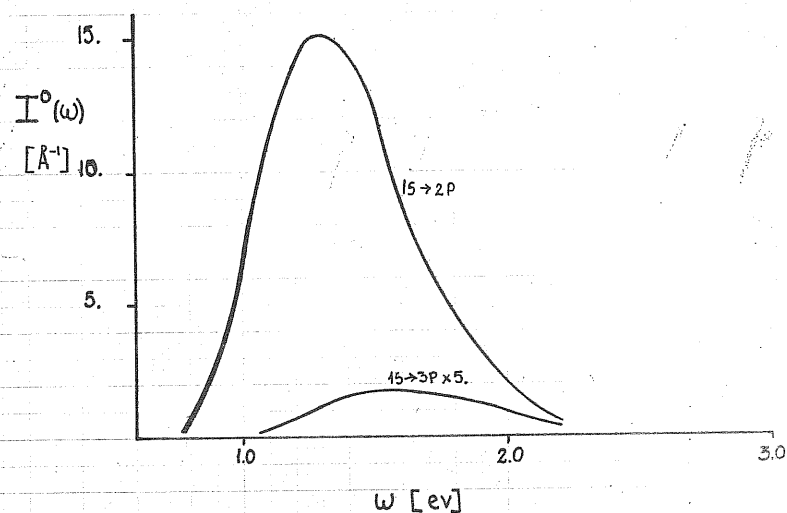
Figure III.5-1 : Optical absorption bands in molten CsCl at T=973 °K . The maximum of $I^0(\omega)$ occurs at $\omega_m = 1.31$ eV for the 1s → 2p transition and at $\omega_m = 1.60$ eV for the 1s → 3p transition . The widths at half maximum are $\Delta\omega = 0.66$ eV and 0.78 eV , respectively .

	NaCl		KCl		KBr		CsCl	
	1s→2p	1s→3p	1s→2p	1s→3p	1s→2p	1s→3p	1s→2p	1s→3p
ω_m (eV)	1.62	2.39	1.37	1.95	1.35	2.00	1.31	1.60
$\Delta\omega$ (eV)	0.47	0.44	0.52	0.58	0.54	0.62	0.66	0.78
$|\Gamma(R_0)|^2$ (Å²)	6.55	0.05	7.46	0.11	7.60	0.06	7.71	0.16
f	0.94	0.011	0.94	0.019	0.94	0.011	0.92	0.026

Table III.5-1 : Optical absorption by the solvated electron .

A value of 0.03 for the latter ratio is obtained for molten CsCl . The experimental value [109] determined by integrating the spectra in Fig.(III.2-3) is found to be 0.12 . The calculated ratio of the areas of the two bands (see Fig.(III.5-1)) is extremely sensitive to the details of the ground state and excited states of the solvated electron .

As discussed in section (III.2-a.2) a lower bound for the oscillator strength is found [109] to be 0.338 for the 1s → 2p transition . The corresponding value for the crystalline F centers lies between 0.7 and 0.8 . The calculated value of 0.9 for this quantity in Table (III.5-1) suggests therefore that the degree of localization of the 2p state is still somewhat overestimated in the present calculations . The assumption of Franck-Condon transitions may also be not quite correct in the liquid .

The choice of the parameter V_{rep} (cf. Eq.(III.3-10)) was performed by requiring that the calculated ω_m for the 1s → 2p transition in KCl should fall in the range $1.3 \div 1.4$ eV , in accord with the available experimental data on this system [84,87] . It was found then $V_{rep} \simeq 0.7$ eV for KCl as reported in Table (III.4-1) . A dependence $V_{rep} \simeq \sigma_+^3$ was then found to yield a reasonable variation of ω_m from salt to salt ,

$$V_{rep}(\sigma_+) \simeq 0.7 \frac{\sigma_+^3}{\sigma_{K^+}^3} \; (eV) \; , \qquad (III.5\text{-}10)$$

where the cation diameters are given in Table (III.4-1) [122] . The qualitative behavior of the experimental data is an appreciable dependence of the absorption peak frequency on the alkali ion for a given halogen ion and insensitivity to the halogen ion for a given alkali ion . Specific measured values reported in the literature for the absorption peak frequency are 1.61 ev

in NaCl [85] , and 1.33 ev , 1.19 ev and 1.07 ev in KCl , KBr , and CsCl , respectively [84] . The calculated band widths are also in reasonable agreement with the data .

A Mollwo-Ivey law can be tested within the present results by plotting the calculated values for ω_m (Table (III.5-1)) against $(\sigma_+ + \sigma_-)^{-2}$ as in Fig.(III.5-2) . This result is to be compared with the plot reported in Fig.(III.2-2) . The present results are consistent with a Mollwo-Ivey law for dilute metal-molten salt solutions .
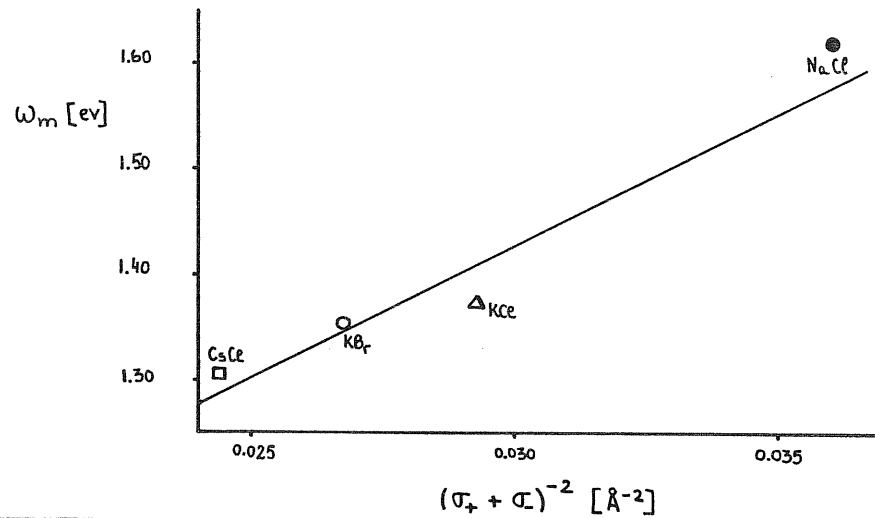
Figure III.5-2 : A Mollwo-Ivey law for the peak frequencies in molten CsCl , KBr , KCl and NaCl .

III.6   Relaxation of excited states and lifetime of the bound state.

It was already remarked (see section (III.4)) , that the bound state disappears during the approach to selfconsistency if the probability of finding the electron inside the well becomes of order 0.6 . It may be therefore expected, from the values of $P_{2p}(R_0)$ and $P_{3p}(R_0)$ in Table (III.4-2) , that the excited states will be unstable against ionic relaxation. This point has been checked by a selfconsistent calculation of the 2p state in a potential $V(r)$ given by

$$
V(r) = \begin{cases} -U_0 \; P_{2p}(R) + V_{rep} + \left(1 - \frac{1}{\epsilon_\infty}\right) e^2 \int_R^\infty \frac{1 - P_{2p}(r)}{r^2} \, dr & (r < R) \\ \\ -\frac{e^2}{\epsilon_\infty} \; \rho \; P_{2p}(R) \int d\underset{\sim}{s} \; \left[g_{+c}(s) - g_{-c}(s) \right] \frac{1}{|\underset{\sim}{r} - \underset{\sim}{s}|} & (r > R). \end{cases}
$$

$$(III.6-1)$$

The calculation converges to $P_{2p}(R) = 0$, irrespectively of the value of V_{rep} and independently of the input value for $P_{2p}(R)$. The calculations were performed for a wide range of values of R (up to $5 \, R_0$(1s)) , using different numerical techniques in order to allow the selfconsistent sequence of the $P_{2p}(R)$ values to change slowly from one step to the subsequent one .

An immediate consequence of an instability of the excited states against ionic relaxation is that the excited electron can rapidly end in a conduction state . This situation is qualitatively different from that of

the excited F center in the crystal at low temperatures, as established

though combined measurements of luminescence and photoconductivity [135] .

The foregoing result seems also relevant in discussing the life-

time of the bound ground state . Symmetry-distorting fluctuations associated

with local diffusive motions of the ions will induce a mixing of a 2p-like

component into the ground state and open a channel for the dissolution of

the bound state . This argument suggests a lifetime on the time scale of

ionic diffusive motions, i.e. of the order of 10^{-12} sec. Lifetimes of this

magnitude have been estimated (see section (III.2-b.1)) [116] from

measured nuclear relaxation rates and shown to be consistent with transport

measurements of electron mobility in these dilute solutions (see section

(III.1-b)) . In fact, the present results are consistent with a thermally

activated hopping process for the electronic conduction in M-MX solutions

[101] . The electronic mobility μ^e can be estimated here by using Eq.

(I.3-1) and Eq.(I.3-2) ,

$$\mu^e = \frac{1}{6} \frac{e}{K_B T} \frac{d^2}{\tau}$$

(III.6-2)

where d is an averaged jump distance and τ is the lifetime of the

trapped electron (or averaged jump time) . A value for d is estimated

in Cs-CsCl solutions [116] to be of ~ 20 Å   , then if one takes

$\tau \sim 10^{-12}$ sec   , at T = 973 °K the electronic mobility μ^e (Eq.(III.6-2)

above) results $\mu^e \approx 0.08$ cm²/V. sec   , which gives the correct

order of magnitude for this quantity determined experimentally [78] in the

limit of high metal dilution .

III.7   Perturbation of the fundamental absorption of the molten salt

by the solvated electron .

A new absorption band in the ultraviolet has been reported for

molten CsCl (cf. Fig.(III.2-1)) [109] . This band is found to have

an intensity nearly equal to that of the infrared band (F band) over the

high-dilution range of electron concentration studied (see Fig.(III.2-5)).

It was then suggested that the UV band may be the liquid-state analogue

of the so-called β band in alkali halide crystals (see section (I.3-c)),

commonly ascribed to the perturbation of the exciton absorption by the

proximity of an F center [22] . A useful reference quantity in this

problem is the position of the unperturbed exciton in the pure system .

The relative separation betweeen the free and bound excitons in these systems

can be estimated theoretically using a change transfer model, already applied

succesfully to the crystal case [30] . No detailed study of the fundamental

absorption in pure molten CsCl , such as that carried out for NaBr [110,112],

seems to be available in the literature . The position of the unperturbed

exciton peak is not therfore knoxn here, but from the experimental data on

the UV band (Fig.(III.2-1)) it appears that the peak of this band in

electron-injected CsCl may be at least 1 ev below the exciton peak energy.

This should be contrasted with the observed β band in the crystal, which is

only about 0.3 ev below the intrinsic exciton .

In an attempt to account for this observation, it is considered

here an adaptation of the charge transfer model [30] to molten salts . In

this simple model of the exciton the differnce $\Delta \nu$ between the frequencies

of the free (unperturbed) exciton and of the β band is viewed as an

electron transfer from a halogen ion to a neighboring alkali ion . It is considered for this purpose a process in which a positive ion and a first-neighbor negative ion are extracted from the crystal and reinserted as atoms after electron transfer, this process being carried out from the neighborhood of a negative ion in the crystal (free exciton) and of an F center (β band) . This leads to an approximate expression for $\Delta \tilde{\nu}$ as the sum of three contributions,

$$h\Delta\tilde{\nu} \equiv h\nu(\text{free exciton}) - h\nu(\beta\text{ band})$$
$$= \Delta E_c - W(r_{+-}) + \Delta E_{POL} \qquad \text{(III.7-1)}$$

where ΔE_c and ΔE_{POL} are the differences in Coulombic and polarization energy between the ionic extraction process in the two configurations, and $W(r_{+-})$ is the overlap repulsive energy of a positive and a negative ion at first-neighbor separation r_{+-} . Taking $r_{+-} = 3.38 \text{ Å}$ in molten CsCl [136] and evaluating ΔE_c from the 1s wave function determined in section (III.4) (see Appendix P) , it is estimated $\Delta E_c = +0.16 \text{ ev}$ and $W(r_{+-}) = 0.07 \text{ ev}$, corresponding to a $\Delta\tilde{\nu}$ of about +0.1 ev in molten CsCl from these terms . As is the case for the crystal [30] , one must therefore look to ΔE_{POL} as the main origin of the perturbation of the fundamental absorption due to the solvated electron .

Following the same approach as for the crystal [30] one can estimate ΔE_{POL} in the liquid by a Mott-Littleton approximation [137],

$$\Delta E_{POL} = g \left(M_F - M_- \right) e^2 / (2r_{+-}) \qquad \text{(III.7-2)}$$

where M_F is given by

$$M_F = \frac{2\alpha_F}{\alpha_+ + \alpha_-} \frac{1}{4\pi} \left(1 - \frac{1}{\epsilon_\infty} \right) \qquad \text{(III.7-3)}$$

in terms of the ionic polarizabilities α_+ and α_- and of the solvated-electron polarizability α_F , and M_- is given by a similar expression with α_F replaced by α_- . The quantity g is a liquid-averaged geometrical factor involving a three-body distribution function which describes a cation and two neighboring anions which are second neighbors of each other . Replacing the liquid average by a triplet of ions at the most probable distances in the liquid ($r_{+-} = 3.38 \text{ Å}$ and $r_{--} = 3.85 \text{ Å}$ in molten CsCl [136]), one can estimate (Appendix P) ,

$$g \simeq 1 - (r_{+-}/r_{--}) + (r_{+-}/r_{--})^4 \simeq 0.7, \qquad \text{(III.7-4)}$$

which is somewhat larger than the value [30] $g = 0.543$ in a NaCl-type crystal . The polarizability α_F of the solvated electron is estimated from the one-level formula

$$\alpha_F = \frac{4 a_0^3 f}{\omega^2_m} \qquad \text{(III.7-5)}$$

where a_0 is the Bohr radius, f is the oscillator strength of the

$1s \longrightarrow 2p$ transition and ω_m is the corresponding peak frequency in Rydbergs . With the values of f and ω_m in Table (III.5-1) and the ionic polarizabilities [66] , it is estimated $\Delta E_{POL} \approx 1.5$ ev .

The conclusion which emerges from this calculation is therfore that the perturbation of a solvated electron on the fundamental absorption in a molten salt may amount to as much as 1 ev or more . This large shift arises essentially from the large value of the polarizability of the solvated electron in the liquid, mainly associated to the lowering of its own absorption frequency relative to the crystal at low temperatures .

III.8   Concluding remarks .

It can be seen in the foregoing that the results of a self-consistent treatment of the solvation process of an excess electron in molten alkali halides are broadly consistent with the available experimental evidence . It would , of course , be too much to ask for detailed quantitative agreement between theory and experiment , but the overall agreement seems reasonable .

It should be remarked that the absorption peak frequencies calculated in Table (III.5-1) for the $1s \longrightarrow 2p$ transition satisfy approximately the relation $\omega_m \propto (\sigma_o + \sigma_+)^{-2}$. Thus the present results are consistent with a Mollwo-Ivey relation which was found to be valid in previous calculations on molten KCl [122] .

One may be tempted , in conclusion , to speculate on the aggregation phenomena that have been reported experimentally with increasing concentration of excess electrons , the most revealing observations being those of spin pairing and spin delocalization in magnetic susceptibility and ESR measurements [120,121] and the related dielectric anomalies [110] . Molecular dynamics studies [128] have shown that there is an attractive long range interaction between two solvated electrons , with the result that a kind of M center , the known defect in alkali halide crystals containing F-centers [127] , can be formed . One may perhaps view the aggregate of two solvated electrons in the molten salt , at the simplest level of approximation , as a stretched alkali molecule surrounded by an ionic dipole layer in a continuum . A molecular viewpoint was found useful in early work [127] on the M center in the crystal . The melting

transition may be a much smaller disturbance on the spectra of such aggregates of F centers than it is for the F center itself [126] . With increasing aggregate size , one may hope to make contact with the evidence [129] on interfaces between liquid-metal electrodes and molten salts .

Finally , the present detailed approach to the states of a single solvated electron should clearly be replaced by a cluster-type approach in dealing with aggregates . This kind of treatment has been succesfully applied in the crystal case [130] . It has the advantage that the wave function of the F-electron can be calculated taking into account the core electrons of the alkali ions forming the cluster , and a direct contact with ENDOR measurements [119] may be made . In the liquid case , however , a rather difficult problem is involved , the a priori unknown position and number of cations entering the shell that surrounds the trapped electrons .

Appendix A:

Longitudinal phonom modes along the [100] direction in an ionic crystal with the NaCl stucture

The equations of motion of the ions in a crystal containing ions per unit cell can be derived from Eq. (I.2-2)

$$
m_j \; \ddot{u}_\alpha(\ell,j) = - \sum_{\ell',j'} \sum_\beta \; \Phi_{\alpha\beta}\begin{pmatrix} \ell & \ell' \\ j & j' \end{pmatrix} u_\beta(\ell',j') \; , \; j=1,2,\cdots s, \qquad (A.1)
$$

where $\ell = (\ell_1, \ell_2, \ell_3)$ labels the unit cells, j refers to the jth ion of mass m_j within the unit cell and $\Phi_{\alpha\beta}\begin{pmatrix} \ell & \ell' \\ j & j' \end{pmatrix}$ is the ionic force constant between ions (ℓ,j) and (ℓ',j') . For longitudinal modes along the 100 direction we can avoid the explicit reference to the indices α,β understanding that all the ionic displacements $\mu(\ell,j)$ are along this particular direction. We can write Eq. (A.1) for the case of an ionic crystal having the NaCl structure (S=2) as follows,

$$
m_1(\ell) \; \ddot{u}_1(\ell) = - \sum_{\ell'} \; \left[\Phi_{11}(\ell,\ell') u_1(\ell') + \Phi_{12}(\ell,\ell') u_2(\ell') \right]
$$

$$
m_2(\tilde{\ell}) \; \ddot{u}_2(\tilde{\ell}) = - \sum_{\ell'} \; \left[\Phi_{21}(\ell,\ell') u_1(\ell') + \Phi_{22}(\ell,\ell') u_2(\ell') \right] \qquad (A.2)
$$

where $\ell = (\ell_1, \ell_2, \ell_3)$ and $\tilde{\ell} = (\ell_1, \ell_2, \ell_3 + 1)$. If we sum over (ℓ_2, ℓ_3) in both sides of Eq. (A-2) and we take into account that ionic displacements $\mu_j(\ell)$ of like ions are independent of their positions in a plane (of index ℓ_1) for longitudinal modes along the $[100]$ direction, we obtain:

$$M_1 \, \ddot{\mu}_1(\ell_1) = - \sum_{\ell_1'} \left[V_{11}(\ell_1, \ell_1') \, \mu_1(\ell_1 + \ell_1') + V_{12}(\ell_1, \ell_1') \, \mu_2(\ell_1 + \ell_1') \right]$$

$$(A.3)$$

$$M_2 \, \ddot{\mu}_2(\ell_1) = - \sum_{\ell_1'} \left[V_{21}(\ell_1, \ell_1') \, \mu_1(\ell_1 + \ell_1') + V_{22}(\ell_1, \ell_1') \, \mu_2(\ell_1 + \ell_1') \right]$$

where

$$V_{ij}(\ell_1, \ell_1') = \mathcal{A}^{-1} \sum_{\substack{\ell_2, \ell_3 \\ \ell_2', \ell_3'}} \mathcal{V}_{ij} \begin{pmatrix} \ell_1, \ell_2, \ell_3 \\ \ell_1', \ell_2', \ell_3' \end{pmatrix} ,$$

and M_j is the mass per unit area of the subplane of $j\underline{th}$ type-ions, i.e. $M = M_1 + M_2$ is the mass per unit area of a (100) plane of total area $\mathcal{A}$, and $V_{ij}(\ell_1, \ell_1')$ is the effective force constant per unit area between subplanes (i, ℓ_1) and (j, ℓ_1').

For this particular case, the dynamical matrix $D_{\alpha\beta}(\vec{q})$ defined in Eq. (I.2-5), can be written as follows,

$$D_{ij}(q) = c\mathcal{A}^{-1} \sum_{\ell_2 \ell_3} \sum_{\ell_1' \ell_2' \ell_3'} \mathcal{V}_{ij} \begin{pmatrix} 0 & \ell_2 & \ell_3 \\ \ell_1' & \ell_2' & \ell_3' \end{pmatrix} e^{-i\, q \cdot \ell_1' d}$$

$$(A.4)$$

$$= \sum_{\ell_1'} V_{ij}(\ell_1') \, e^{-i\, q \ell_1' d} ,$$

where d is the interplanar spacing of the (100) planes. Assuming a plane wave solution for the subplane displacements μ_j we obtain the two phonom dispersion relations by solving the determinantal equation:

$$\begin{vmatrix} D_{11}(q) - M_1 \omega^2 & D_{12}(q) \\ \\ D_{21}(q) & D_{22}(q) - M_2 \omega^2 \end{vmatrix} = 0 \qquad (A.5)$$

The solutions of (A.5) can easily found to be:

$$\omega_{\pm}^2 = \frac{1}{2}\left(\frac{D_{11}(q)}{M_1} + \frac{D_{22}(q)}{M_2}\right) \pm \frac{1}{2}\sqrt{\left(\frac{D_{11}}{M_1} - \frac{D_{22}}{M_2}\right)^2 + 4\frac{D_{12}^2(q)}{M_1 M_2}} \quad (A.6)$$

where $\omega_{\pm}$ are the so called optic (+) and acoustic (−) phonom modes. From (A.6) one can see that it is not possible to express $D_{ij}(q)$ in terms of $\omega_{\pm}^2$ along. If we define:

$$C(q) = D_{22}(q) - D_{11}(q) , \quad (A.7)$$

we can write D_{ij} in the following way:

$$D_{11}(q) = \mu(\omega_+^2 + \omega_-^2) - \frac{\mu}{M_2} C(q)$$

$$(A.8)$$

$$D_{22}(q) = \mu(\omega_+^2 + \omega_-^2) + \frac{\mu}{M_1} C(q)$$

and

$$D_{12}(q) = \eta\,\mu\left[(\omega_+^2 + \omega_-^2)^2 - \frac{M_1 M_2}{\mu^2}\omega_+^2\omega_-^2 + \left(\frac{1}{M_1} - \frac{1}{M_2}\right)C(q)(\omega_+^2 + \omega_-^2)\right.$$
$$\left. - \frac{1}{M_1 M_2}C^2(q)\right]^{1/2}$$

where $\frac{1}{\mu} = \frac{1}{M_1} + \frac{1}{M_2}$ and $\eta(= \pm 1)$ is the appropriate sign of D_{12}. In order to completely determine $D_{ij}(q)$ we have to recourse to a model for the determination of $C(q)$ and η.

Appendix B

A lattice sum method and the Coulomb contribution to the force constants between (100) planes in an ionic crystal with the NaCl structure

The potential $\emptyset(\bar{r},\rho)$ created by a (neutral) plane of alternating positive and negative point charges on a lattice point outside of the plane situated a distance ρ perpendicular to it can be written as follows,

$$\emptyset(\bar{r},\rho) = \frac{e^2}{\Delta_2} \sum_{h}' |K_h|^{-1} e^{-2\pi\rho|K_h| + 2\pi i\, K_h \cdot \bar{r}} \qquad (B.1)$$

where $\bar{r}$ is the component of the position vector of the field point in the plane we are calculating $\emptyset(\bar{r},\rho)$, K_h is the reciprocal lattice vector of the direct plane lattice and Δ_2 is the area of the unit cell of the lattice. The sum in (B.1) extends over all the $K_h's$ different from zero.

For a (100) plane with the NaCl structure the primitive vectors are shown in the figure:
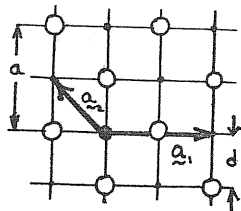
$$a_1 = a(1,0)$$
$$a_2 = \frac{a}{2}(-1,1) \qquad (B.2)$$
$$\Delta_2 = 2d^2$$

The reciprocal lattice vectors are given by:

$$b_1 = \frac{1}{a}(1,1) \quad , \quad b_2 = \frac{2}{a}(0,1) \, . \qquad (B.3)$$

A general reciprocal lattice vector K_h can be written,

$$K_h = \frac{1}{a}(h_1, h_2) \quad , \quad h_{1,2} = 0, \pm 1, \pm 2, \cdots \qquad (B.4)$$

Using the previous result we can evaluate the force constants f per unit area between planes separated a distance ρ due to the Coulomb interaction: by definition

$$f(\rho) = \left. \frac{d^2 \emptyset(\bar{r},\rho)}{d\rho^2} \right|_{equilib.} \qquad (B.5)$$

which can be written using (B.1) as follows:

$$f(\rho) = \frac{4\pi^2 e^2}{2d^2} \sum_{h}' |K_h| e^{-2\pi\rho|K_h| + 2\pi i\, K_h \cdot \bar{r}} \qquad (B.6)$$

Putting $\bar{r} = 0$ and taking K_h as in (B.4), the

following expression is obtained:

$$f(\rho) = \frac{2\pi^2 e^2}{d^5} \sum_{h_1, h_2 = 1}^{\infty} \sqrt{h_1^2 + h_2^2} \; e^{-\pi \sqrt{h_1^2 + h_2^2} \; \rho/d} \quad . \qquad (B.7)$$

The evaluation of $f(\rho)$ for $\rho = d, 2d, 3d$ gives:

$$f(d) = \frac{2\pi^2 e^2}{d^5} \quad 207. \; 10^{-4}$$

$$f(2d) = \frac{2\pi^2 e^2}{d^5} \quad 2. \; 10^{-4} \qquad (B.8)$$

$$f(3d) = \frac{2\pi^2 e^2}{d^5} \quad 2. \; 10^{-6}$$

The force constants between second-neighbor planes are already 1% of that for first-neighbor planes.

Appendix C

The dynamical matrix for the (100) direction with nearest-neighbor planes interaction only

The equation of motion of the (100) planes with nearest-neighbor planes interactions only, are written from the expression (A.3) in this particular case as follows:

$$M_1 \; \ddot{u}_1(0) = \left[u_1(1) - u_1(0) \right] f_{11} + \left[u_1(-1) - u_1(0) \right] f_{11} + \left[u_2(1) - u_1(0) \right] f_{12} +$$
$$+ \left[u_2(-1) - u_1(0) \right] f_{12} + \left[u_2(0) - u_1(0) \right] \beta f_{12} .$$

$$(C.1)$$

$$M_2 \; \ddot{u}_2(0) = \left[u_2(1) - u_2(0) \right] f_{22} + \left[u_2(-1) - u_2(0) \right] f_{22} + \left[u_1(1) - u_2(0) \right] f_{21} +$$
$$+ \left[u_1(-1) - u_2(0) \right] f_{21} + \left[u_1(0) - u_2(0) \right] \beta f_{21} .$$

Assuming a plane wave solution for u_j of the form:

$$\mu_j(\ell) = \mu_j \, e^{-i(\omega t - q\ell d)} \qquad , \qquad \text{(C.2)}$$

we obtain:

$$M_1 \omega^2 \mu_1 = D_{11}(q)\, \mu_1 + D_{12}(q)\, \mu_2$$

$$M_2 \omega^2 \mu_2 = D_{21}(q)\, \mu_1 + D_{22}(q)\, \mu_2 \qquad \text{(C.3)}$$

where:

$$D_{11}(q) = f_{12}(2+p) + 2f_{11}(1-\cos qd)$$

$$D_{22}(q) = f_{12}(2+p) + 2f_{22}(1-\cos qd) \qquad \text{(C.4)}$$

$$D_{12}(q) = D_{21}(q) = -f_{12}(2\cos qd + p).$$

The two phonom branches $\omega_\pm$ are given as in (A.6).

Appendix   D

Calculation of the force constant between nearest-neighbor planes for cleavage at small separations of the two crystal halves, within the force constant model of Appendix   C

a)   A:

The expression of the coefficient   A   for the cleavage force at small separations   Z   of the crystal halves is:

$$A^{-1} = \frac{d}{2\pi} \int_{-\pi/d}^{\pi/d} dq \; \sin^2(\tfrac{1}{2}qd) \; \frac{D_{11}(q) + D_{22}(q) - 2D_{12}(q)}{D_{11}(q)\, D_{22}(q) - D_{12}^2(q)} \qquad (D.1)$$

An analytical result is obtained using the expression of $D_{ij}(q)$ given by (C.4). We then find:

$$D_{11} + D_{22} - 2D_{12} = 4\left[f_{12}(2+\beta) + (f_{11} + f_{22} - 2f_{12}) \sin^2(\tfrac{1}{2}qd) \right]$$

$$(D.2)$$

$$D_{11}D_{22} - D_{12}^2 = 4\left[4(f_{11}f_{22} - g_{12}^2)\sin^2(\tfrac{1}{2}qd) + f_{12}(2+\beta)(f_{11} + f_{22} + 2f_{12}) \right] \sin^2(\tfrac{1}{2}qd)$$

The integral part can be written

$$A^{-1} = \frac{1}{2(f_{11} + f_{22} + f_{12})} \cdot \frac{2}{\pi} \int_{0}^{\pi/2} dx \; \frac{a - b \sin^2 x}{a - c \sin^2 x}$$

$$(D.3)$$

$$= \frac{1}{2(f_{11} + f_{22} + f_{12})} \left[\frac{b}{c} + \left(1 - \frac{b}{c}\right)\sqrt{a/(a-c)} \right]$$

where

$$a = f_{12}(2 + \beta)$$

$$b = 2\left[f_{12} - (f_{11} + f_{22}) \right] \qquad (D.4)$$

$$c = b + 2\frac{(f_{11} - f_{22})^2}{f_{11} + f_{22} + f_{12}} .$$

b)   B:

The expression for the coefficient of the cleavage force in determining the intraplanar spacing δ is:

$$B = \frac{d}{2\pi} \int_{-\pi/\delta}^{\pi/\delta} dq \; \sin^2\left(\tfrac{1}{2}qd\right) \; \frac{D_{22}(q) - D_{11}(q)}{D_{11}(q) D_{22}(q) - D_{12}^2(q)} \qquad (D.5)$$

Using the results in Appendix C:

$$D_{22}(q) - D_{11}(q) = 4\left(f_{22} - f_{11}\right) \sin^2\left(\tfrac{1}{2}qd\right) \qquad (D.6)$$

The integral in (D.5) is now written as:

$$B = \left(f_{22} - f_{11}\right) \frac{2}{\pi} \int_{0}^{\pi/2} dx \; \frac{\sin^2(x)}{b - a\,\sin^2(x)}$$

$$\qquad\qquad\qquad\qquad\qquad (D.7)$$

$$= \frac{f_{22} - f_{11}}{a} \left(\sqrt{b/(b-a)} - 1 \right)$$

where

$$a = 4\left(f_{12}^2 - f_{11} f_{22} \right)$$

$$\qquad\qquad\qquad\qquad (D.8)$$

$$b = f_{12}(2+\beta)\left(f_{11} + f_{22} + 2 f_{12} \right)$$

Appendix E

Fitting of the phonom curves with the model of Appendix C

The model of nearest-neighbor planes interaction studied in Appendix C for the phonom curves $\omega_{\pm}$ can be summarized in the following equations:

$$\omega_{\pm}^2 = \frac{1}{2}\left(\frac{D_{11}}{M_1} + \frac{D_{22}}{M_2}\right) \pm \frac{1}{2}\sqrt{\left(\frac{D_{11}}{M_1} - \frac{D_{22}}{M_2}\right)^2 + 4\frac{D_{12}^2}{M_1 M_2}} \qquad (E.1)$$

where

$$D_{11}(q) = f_{12}(2+\beta) + 2 f_{11}(1 - \cos qd)$$

$$D_{22}(q) = f_{12}(2+\beta) + 2 f_{22}(1 - \cos qd)$$

$$D_{12}(q) = - f_{12}(2\cos qd + \beta).$$

By fitting the experimental phonom dispersion relations with (E.1) we can determine by a least-square procedure the following values of the force constants:

	$d(\text{Å})$	$M_1(+)$	$M_2(-)$	f_{11}	f_{22}	f_{12}	βf_{12}
LiF	2.01	3.88	1.45	-1.66	1.34	3.35	10
NaCl	2.82	2.39	3.69	-0.31	0.114	1.08	1.4
KCl	3.14	4.65	1.61	-0.057	-0.125	0.825	0.88
KBr	3.30	2.98	6.09	-0.005	-0.155	0.67	0.61
KI	3.54	2.61	8.43	-0.125	-0.015	0.525	0.38
MgO	2.105	4.56	3.00	-5.67	-8.52	0.325	32.4
CaO	2.405	5.75	2.30	-2.15	-0.15	5.0	8.6

Force constants (10^{19} dynes/cm^3) and masses (10^{-8} gr/cm^2) for some ionic crystals in the nearest-neighbor planes interactions model (E.1)

Phonon dispersion relations : [100] direction, LA & LO.
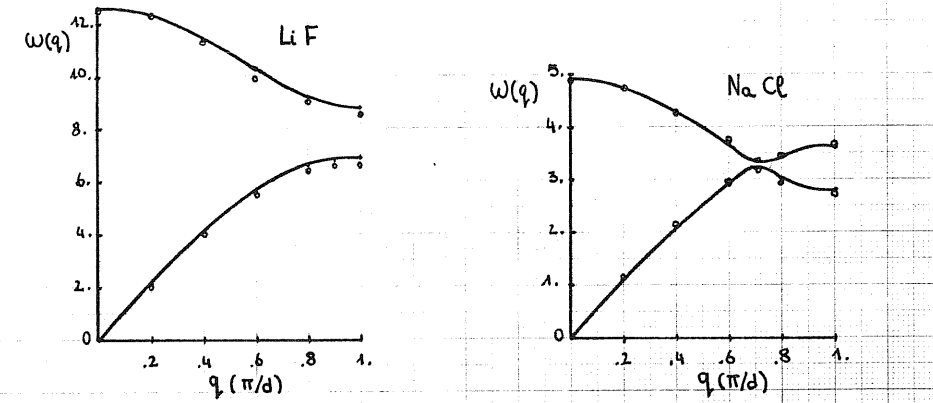
Experimental values (o) : $\omega \left[10^{13} \text{ rad/sec}\right]$; continuous line : Eq. (E.1).

KCl

$\omega(q)$ $q(\pi/d)$

KBr

$\omega(q)$ $q(\pi/d)$

kI

$\omega(q)$ $q(\pi/d)$

MgO

$\omega(q)$ $q(\pi/d)$

CaO

$\omega(q)$ $q(\pi/d)$
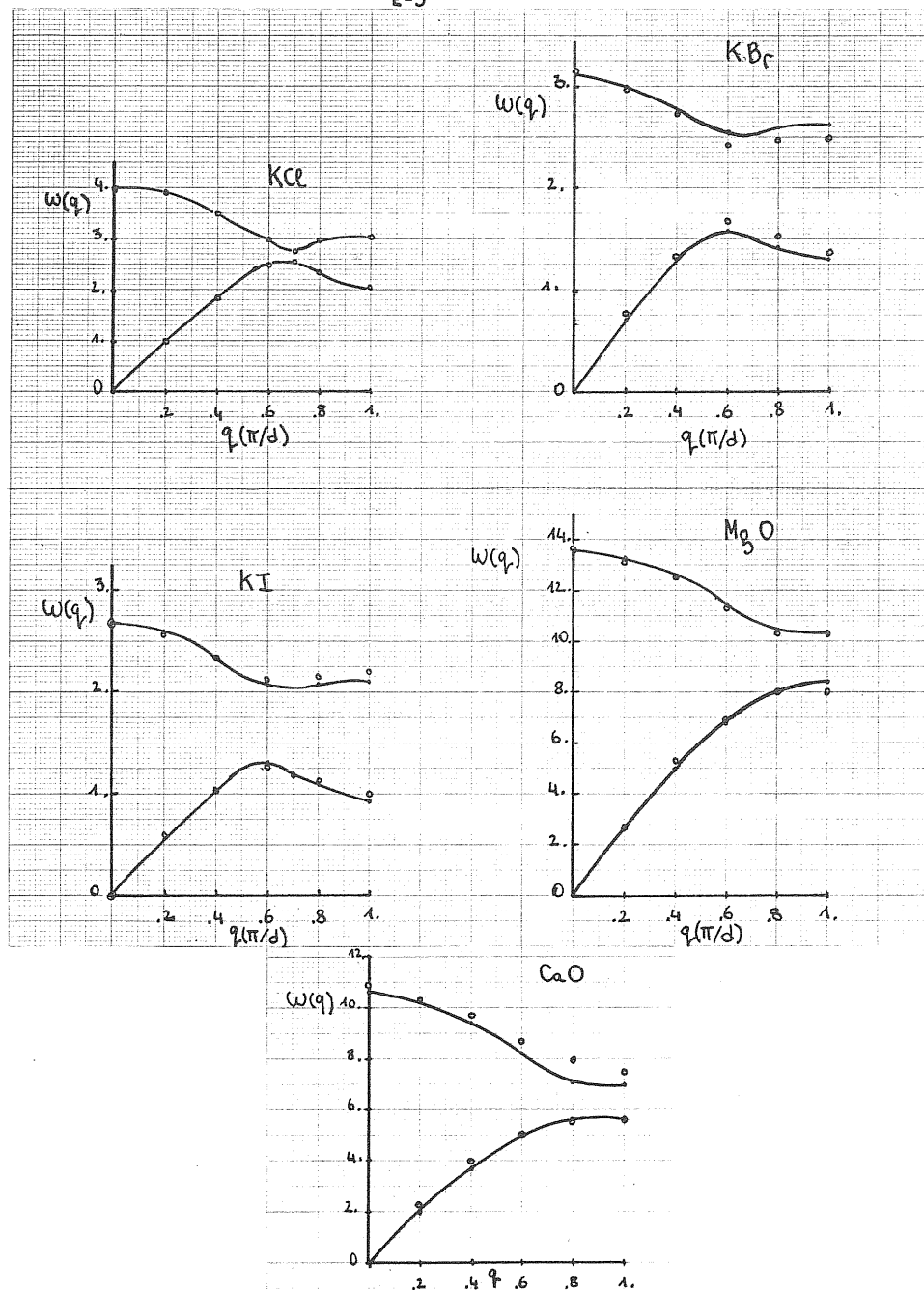
Appendix F

The effective one-phonom acoustic branch in the determination of A (Eq. II.2-13)

a)   Generalities:

The force constant A for the cleavage force at small separations can be written using (A.8) and Eq. (II.2-13) as follows:

$$\vec{A}^{-1} = \frac{d}{\pi}\int_0^{\pi/d} dq\ \sin^2\left(\tfrac{1}{2}qd\right)\frac{2\mu}{M_1 M_2 \omega_+^2 \omega_-^2}\left[(\omega_+^2 + \omega_-^2) + \left(\frac{1}{M_1} - \frac{1}{M_2}\right)\frac{C(q)}{2} - \eta\left(\omega_+^2 - \omega_-^2\right)\Gamma\left(\omega_+^2 \omega_-^2\right)\right] \quad (F.1)$$

where use has been made of the relation:

$$D_{11}(q)\,D_{22}(q) - D_{12}^2(q) = M_1 M_2\,\omega_+^2(q)\,\omega_-^2(q)\ , \qquad\qquad (F.2)$$

and

$$\Gamma\left(\omega_+^2, \omega_-^2\right) = \left(\omega_+^2 - \omega_-^2\right)^{-1}\left[\left(\omega_+^2 + \omega_-^2\right)^2 - \frac{M_1 M_2}{\mu}\omega_+^2 \omega_-^2 + \left(\frac{1}{M_1} - \frac{1}{M_2}\right)C(q)(\omega_+^2 + \omega_-^2) - \frac{C^2(q)}{M_1 M_2}\right]^{1/2}.$$

$$(F.3)$$

Defining $M = M_1 + M_2$ and $\Delta = M_2 - M_1$, (F.1) can be written as follows:

$$A^{-1} = \frac{2}{M} \frac{d}{\pi} \int_0^{\pi/d} dq \; \sin^2\left(\tfrac{1}{2}qd\right)\left[\frac{1}{\omega_+^2} + \frac{1}{\omega_-^2} + \frac{2\Delta}{M^2-\Delta^2}\frac{C(q)}{\omega_+^2\omega_-^2} - \eta\left(\frac{1}{\omega_-^2} - \frac{1}{\omega_+^2}\right)\Pi\right] \quad (F.4)$$

where

$$\Pi = \frac{1}{(\omega_+^2-\omega_-^2)}\left[(\omega_+^2-\omega_-^2)^2 - \frac{4}{M^2-\Delta^2}\left(\Delta^2\omega_+^2\omega_-^2 - \Delta(\omega_+^2+\omega_-^2)C(q)+C^2(q)\right)\right]^{1/2} . \quad (F.5)$$

b)   Approximations:

The first great simplification of the problem, summarized in (F.4) - (F.5), can be achieved by noticing empirically that $\Pi(\omega_+^2,\omega_-^2)\approx 1$. This value for Π is obtained whenever the second term

under parenthesis in (F.5) vanishes, i.e.

$$C^2(q) - \Delta(\omega_+^2 + \omega_-^2)C(q) + \Delta^2\omega_+^2\omega_-^2 = 0. \quad (F.6)$$

The solutions of (F.6) are : $C_\pm = \Delta \cdot \omega_\pm^2$. (F.7) This relation can in fact be tested using the simple model developed in Appendix C and the values of the force constants reported in Appendix E . Within this model it turns out that

$$C(q) = D_{22}(q) - D_{11}(q) = 4\left(f_{22}-f_{11}\right)\sin^2\left(\tfrac{1}{2}qd\right) . \quad (F.8)$$

This relation can be compared with an effective acoustic branch of the type

$$\omega^2(q) = \Omega^2 \sin^2\left(\tfrac{1}{2}qd\right) . \quad (F.9)$$

Using (F.7) with (F.8), (F.9) we obtain

$$C(q) = 4\left|f_{22}-f_{11}\right|\sin^2\left(\tfrac{1}{2}qd\right) \equiv \Delta \cdot \Omega^2 \sin^2\left(\tfrac{1}{2}qd\right) , \quad (F.10)$$

so that

$$\left| f_{22} - f_{11} \right| = \frac{\Delta}{4} \, \Omega^2 \, . \qquad \text{(F.11)}$$

The meaning of (F.7) is the following: whenever the two branches $\omega_{\pm}^2$ do not cross (see figure (a)) we have $\omega(q) \cong \omega_-(q)$ if the branches do cross, opening a gap at $q = q_c$, (see figure (b)) the effective branch is given by $\omega(q) \cong \omega_+$ for $q > q_c$.

(a)   (b)
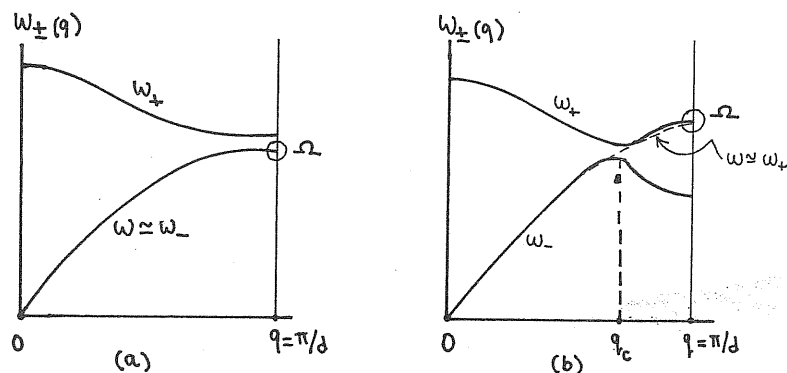
We now need to test (F.11) to see wether this hypothesis is correct. In the following table are reported the values of $\left| f_{22} - f_{11} \right|$ taken from Appendix E and those of $\omega^2(q)$ calculated by fitting $\omega^2(q)$

in (F.9) to the experimental acoustic branch $\omega_-^2(q)$ near the zone center.

	$\left\| f_{22}-f_{11} \right\|$	$\frac{\Delta}{4}\Omega^2$	M	Ω^2
LiF	3.0	2.7	5.33	43.56
NaCl	0.42	0.42	6.09	12.96
KCl	0.068	0.068	6.26	9.00
KBr	0.15	0.31	9.07	6.25
KI	0.11	0.32	11.03	3.24
MgO	2.8	2.5	7.56	70.56
CaO	2.0	2.7	8.05	31.36

Nearest neighbor planes interaction parameters and one-phonon branch model. Force constants are in 10^{19} dynes/cm^3 ; masses in 10^{-8} gr/cm^2 and Ω in 10^{13} rad/sec.

According to the table the relation (F.11) seems to be approximately satisfied. We are now allowed to write A^{-1} in (F.4) as follows:

$$A^{-1} = \frac{2}{M} \frac{d}{\pi} \int_0^{\pi/d} dq \, \sin^2\left(\tfrac{1}{2}qd\right) \left[(1-\eta)\frac{1}{\omega_-^2} + (1+\eta)\frac{1}{\omega_+^2} + \frac{2\Delta}{H^2-\Delta^2} \frac{C(q)}{\omega_+^2 \, \omega_-^2} \right] . \qquad \text{(F.12)}$$

From the expression of $D_{12}(q)$ in (E.1) one finds that:

$$\eta = \begin{cases} -1 & : & q < q_c \\ \\ +1 & : & q > q_c \end{cases} \qquad\qquad (F.13)$$

Due to (F.13) it is now possible to write the following approximate expression using (F.9):

$$\left(1-\eta\right)\frac{1}{\omega_-^2} + \left(1+\eta\right)\frac{1}{\omega_+^2} \simeq \frac{2}{\omega^2(q)} \qquad\qquad (F.14)$$

where $\omega(q)$ is the effective one-phonom branch. Now, neglecting the small contribution of the $C(q)$ term in (F.12) , the final expression for A^{-1} is

$$A^{-1} = \frac{2}{M}\ \frac{d}{\pi}\int_0^{\pi/d} dq\ \ \sin^2\left(\tfrac{1}{2}qd\right)\ \frac{2}{\omega^2(q)}$$

$$= \frac{4}{M}\ \frac{1}{\Omega^2}\ \frac{d}{\pi}\int_0^{\pi/d} dq$$

or equivalently

$$A = \frac{1}{4}\ M\ \Omega^2 \ . \qquad\qquad (F.15)$$

Appendix G

Fluorite structure: Longitudinal phonom modes along the (111) direction

a)   Generalities:

The fluorite structure has a face-centred-cubic translational group. The primitive translation vectors of the fcc as shown in Fig. (G.1) are $\underset{\sim}{a} = \frac{a}{2}(\hat{x}+\hat{y})$, $\underset{\sim}{b} = \frac{a}{2}(\hat{y}+\hat{z})$ and $\underset{\sim}{c} = \frac{a}{2}(\hat{x}+\hat{z})$ (G.1).
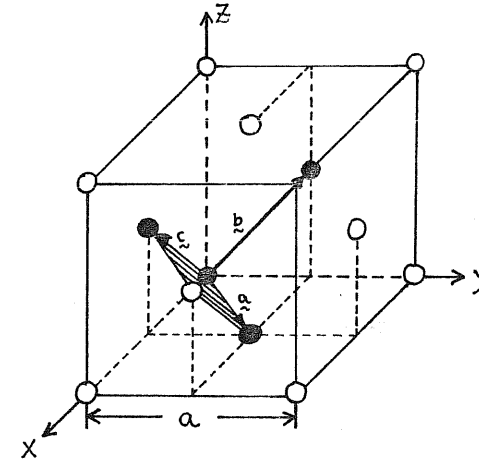
Figure G.1:   Primitive basic vectors of the fcc lattice.

The reciprocal lattice vectors are written in general:

$$\underset{\sim}{G}(h\,k\,\ell) = \frac{2\pi}{a}\left[(h-k+\ell)\,\hat{x} + (h+k-\ell)\,\hat{y} + (-h+k+\ell)\,\hat{z}\right] \quad . \quad \text{(G.2)}$$

The distance d between crystallographic $(h\,k\,1)$ planes is given by:

$$d(h\,k\,\ell) = 2\pi \Big/ \left|\underset{\sim}{G}(h\,k\,\ell)\right| \quad . \quad \text{(G.3)}$$

b)   The (111) planes:

The distance between (111) planes is given by $(G.3)$ as:

$$d(111) = \frac{2\pi}{\left|\frac{2\pi}{a}(1,1,1)\right|} = \frac{a}{\sqrt{3}} \quad . \quad \text{(G.4)}$$

The area per molecule Ar (for CaF_2 or BaF_2) on a (111) plane is given by the shaded area in Fig. (G.1) as follows:

$$A_r = \left|\underset{\sim}{a}\times\underset{\sim}{c}\right| = \begin{vmatrix} \hat{x} & \hat{y} & \hat{z} \\ a/2 & a/2 & 0 \\ a/2 & 0 & a/2 \end{vmatrix} = \left|\frac{a^2}{4}\hat{x} - \frac{a^2}{4}\hat{y} - \frac{a^2}{4}\hat{z}\right| = \frac{a^2}{4}\sqrt{3} \quad \text{(G.5)}$$

The wave vectors (in the first Brillouin zone) along the $[111]$ direction

take the extreme values: $\underset{\sim}{q} = \pm\frac{1}{2}\underset{\sim}{G}(111)$ i.e.

$$\underset{\sim}{q}\,(\text{zone boundary}) = \pm\frac{\pi}{a}(111) \quad \text{or} \quad \left|\underset{\sim}{q}(z.b.)\right| = \frac{\pi}{a}\sqrt{3} \quad . \quad \text{(G.6)}$$

Then, it results from $(G.4)$ and $(G.6)$ that: $\frac{1}{2}q_{zb}\,d = \pi/2$.

The values for the density ρ can be obtained from $\rho = \frac{4M}{a^3}\frac{1}{N_{av}}$ where M is the molecular weight and $N_{av} = 6.022\ 10^{23}$.

The mass per unit area M_r of a (111) plane is obtained from:

$$M_r = \frac{1}{N_{av}}\frac{M}{A_r(111)} = \frac{4}{\sqrt{3}}\frac{M}{a^2}\frac{1}{N_{av}} = \rho d \quad . \quad \text{(G.7)}$$

In the following table are summarized some useful quantities for CaF_2 and BaF_2 .

	$a\ (\overset{o}{A})$	$M(gr/mol)$	$\rho\ (gr/cm^3)$	$M_r\ (10^{-7}\ gr/cm^2)$
CaF_2	5.46	78.08	3.18	10.03
BaF_2	6.20	175.36	4.83	17.49

Parameters for CaF_2 and BaF_2 . The mass per unit area Mr corresponds to the (111) planes. Data from $[15]$.

c)   The effective one-phonon branch for A in the fluorites

According to the model presented in Appendix F, we can write the constant of proportionality A in the expression of the cleavage force at small distances as:

$$A = \frac{1}{4} M_r \Omega^2 .$$
(G.8)

By fitting the acoustic phonom curve with a dispersion relation of the kind: $\omega^2 = \Omega^2 \sin^2\left(\frac{1}{2} q d\right)$, in CaF$_2$ and BaF$_2$ we obtain the following values for Ω and A :

	Ω $(10^{13}$ rad/sec)	A $(10^{19}$ dyn/cm^3)	$A = C_{111}/d$
CaF$_2$	4.25	4.54	4.12
BaF$_2$	2.45	2.62	2.52

Effective one-phonom curve parameters in CaF$_2$ and BaF$_2$.

The value of Ω can be determined from the velocity of sound for elastic waves along the (111) direction:

$$\omega^2(q \to 0) = C_s^2 q^2 \simeq \frac{1}{4} q^2 d^2 \Omega^2 ,$$
(G.9)

from which we can write:

$$\Omega^2 = \frac{4}{d^2} C_s^2 = \frac{4}{d^2} \frac{C_{111}}{\rho}$$
(G.10)

where $C_{111} = \frac{1}{3}\left(C_{11} + 2 C_{12} + 4 C_{44}\right)$. Using (G.10) in (G.8) and the fact that $M_r = \rho d$ we obtain the A values reported in the third column of the table, where $A = C_{111}/d$. (G.11). The values of the elastic constants are reported in Table (I.2-1).

Appendix H

The cleavage force at large separations of the crystal halves.
The dipole-dipole van der Waals interaction

At large separations Z of the two crystal halves, cleaved along a (h k l) plane, the attractive interaction between them is due to the van der Waals forces: $f_{ij} = 6 c_{ij} / r_{ij}^7$, where c_{ij} are the ionic van der Waals coefficients for the dipole-dipole interaction. If $\underset{\sim}{a}$ and $\underset{\sim}{b}$ are the primitive vectors on the crystallographic planes ((100) planes for NaCl-type crystals and (111) planes for fluorite- type crystals), the total force per unit area on a molecule on the surface of the left-half crystal due to the surface plane in the right-half crystal, separated a distance Z is given by

$$\frac{\Lambda}{A_r} \sum_{\ell_1 \ell_2} \frac{6 C_m}{\left[Z^2 + (\ell_1 \underset{\sim}{a} + \ell_2 \underset{\sim}{b})^2 \right]^{7/2}} \qquad (H.1)$$

where A_r is the area per molecule on the plane and C_m is the molecular van der Waals coefficient which reads as follows:

$$C_m = \begin{cases} C_{++} + C_{--} + 2 C_{+-} : \text{NaCl- type} \\[2em] C_{++} + 4 C_{--} + 4 C_{+-} : \text{Fluorite- type} \end{cases} \qquad (H.2)$$

Summing over all the (h k l) planes in the right-half crystal and over all the molecules along the line ([h k l] direction) which ends up on the first molecule at the surface of the left-half crystal, we find the cleavage force F to be given by:

$$F = \frac{6 C_m}{A_r} \sum_{\ell_4} \sum_{\ell_3} \sum_{\ell_2 \ell_1} \left[(Z + \ell_4 d + \ell_3 d)^2 + (\ell_1 \underset{\sim}{a} + \ell_2 \underset{\sim}{b})^2 \right]^{-7/2} \qquad (H.3)$$

where d is the interplanar spacing between the (h k l) planes. Going to the continuous approximation we have:

$$F = 6 \frac{C_m}{A_r} \int_0^\infty \frac{d\zeta}{d} \int_0^\infty \frac{d\zeta'}{d} \int_0^\infty dr \frac{2\pi r}{A_r} \left[(Z + \zeta + \zeta')^2 + r^2 \right]^{-7/2}$$

or

$$F = \frac{6\pi}{A_r^2 d^2} C_m \int_0^\infty d\zeta \int_0^\infty d\zeta' \frac{2}{5} (Z + \zeta + \zeta')^{-5} = \frac{12\pi}{5} \frac{C_m}{A_r^2 d^2} \int_0^\infty d\zeta \frac{1}{4} (Z + \zeta)^{-4}$$

and finally

$$F = \frac{3}{5} \pi \frac{C_m}{A_r^2 d^2} \frac{1}{3 Z^3} = \frac{\pi}{5} C_m \frac{Z^{-3}}{A_r^2 d^2} \qquad (H.4)$$

Taking into account that the number of molecules per unit volume

$$m = 1/A_r d = 4/a^3 \qquad \text{(for both type of crystals)},$$

we can rewrite (H.4) as follows:

$$F = \frac{\pi}{5} m^2 \frac{C_m}{Z^3} \qquad \text{(H.5)}$$

where C_m is given by (H.2).

Appendix J:

The dipole layer contribution to the cleavage force at large

separations of the two crystal halves

The Coulomb potential created at a (large) distance Z from a dipole layer can be calculated using known expressions for the Coulomb potential due to planar distributions of charges [5] , i.e.

$$S(\underset{\sim}{r}, Z) = -\frac{\pi}{d^2} Z + \frac{\pi}{d^2} \underset{\underset{\sim}{K}}{\sum}' |\underset{\sim}{K}|^{-1} e^{-|Z||K|} e^{i \underset{\sim}{K} \cdot \underset{\sim}{r}} , \qquad \text{(J.1)}$$

where $\underset{\sim}{r}$ is the component of the position vector of the field point , d is the lattice spacing and $\underset{\sim}{K}$ are the reciprocal lattice vectors of the plane . It is clear that the force constant associated with (J.1) has an exponential dependence on Z ;

$$f(\text{dipole layer}) \sim e^{-|K| Z} , \qquad \text{(J.2)}$$

which gives a negligible contribution to the cleavage force at large values of Z compared with the van der Waals term $\sim Z^{-3}$.

Appendix K :

Collection of data for some ionic crystals

	$\varepsilon_\infty^{(a)}$	$\varepsilon_0^{(b)}$	$\alpha_m(10^{-24}cm^3)^{(b)}$	$E_g(ev)^{(c)}$	$E_x(ev)^{(a)}$
LiF	1.96	9.01	0.887	~12.	12.9
LiCl	2.78	10.95	2.976	~10.	8.67
LiBr	3.17	13.25	4.120	8.5	7.23
LiI	3.80	16.85	6.145	5.9	5.94
NaF	1.74	5.05	1.148	10.5	10.66
NaCl	2.34	5.90	3.237	8.6	7.96
NaBr	2.59	6.28	4.381	7.7	6.71
NaI	2.93	7.28	6.406	5.8	5.61
KF	1.85	5.46	1.991	10.9	9.88
KCl	2.19	4.84	4.080	8.5	7.79
KBr	2.34	4.90	5.224	7.8	6.71
KI	2.62	5.10	7.249	6.2	5.88
RbF	1.96	6.48	2.537	10.4	9.54
RbCl	2.19	4.92	4.626	8.2	7.54
RbBr	2.34	4.86	5.770	7.7	6.64
RbI	2.59	4.91	7.795	6.1	5.73
CsF	2.16	-	3.601	10.0	9.27
CsCl	2.62	7.20	5.690	8.0	7.85
CsBr	2.42	6.67	6.834	7.0-8.0	6.83
CsI	2.62	6.59	8.859	6.3	5.30
$CaF_2^{(d)}$	~2.04	~6.7	2.816	12.2	11.18
$BaF_2^{(d)}$	~2.16	~7.2	4.216	10.59	10.00

(a) From [134] , (b) [67] , (c) [69] , (d) [71] .

Appendix L :

The ground state potential within the MSA

(a) V_{coul} for $r < R$:

The Coulomb contribution to $V_{pi}(r)$ for $r < R$ is given by (cf. Eq.(III.3-2))

$$V_{coul} = - e^2 \, \rho_{1s}(R) \int_R^\infty 4\pi \, r \, \rho \, \left(g_{+c}(r) - g_{-c}(r) \right) \, dr . \qquad (L.1)$$

Using the known relations between $g_{\pm c}$ and g_{++} given by the MSA [50] , one can rewrite (L.1) as

$$V_{coul} = -8\pi e^2 \, \frac{1 + \Gamma\bar{\sigma}}{1 + \Gamma\sigma} \, \rho_{1s}(R) \, \rho \int_R^\infty dr \, r \, g_{++}(r) . \qquad (L.2)$$

The latter integration can be carried out by using a representation of the pair correlation functions g_{++} for equi-sized ions [48] given by the MSA ,

$$V_{coul} = -8\pi e^2 \, \frac{1 + \Gamma\bar{\sigma}}{1 + \Gamma\sigma} \, \rho_{1s}(R) \, \rho \, . \, \frac{2e^2}{K_0^2 \, K_B T} \, \frac{\Gamma\bar{\sigma}}{1 + \Gamma\bar{\sigma}} \qquad (L.3)$$

with $\quad K_0^2 = \dfrac{8\pi e^2}{K_B T}\, \wp$, one thus obtains

$$V_{coul} = -\ \frac{2 e^2\, \Gamma}{1 + \Gamma\,\sigma}\ P_{1s}(R) \tag{L.4}$$

where Γ is given , in this particular case , by

$$\Gamma = \frac{1}{2\bar{\sigma}}\left(\sqrt{1 + 2\bar{\sigma}\,K_0'} - 1\right). \tag{L.5}$$

(b) V_{out} for $r > R$:

The potential outside the cavity of radius R has the screened Coulomb expression (cf, Eq.(III.3-7))

$$V_{out}^{(r)} = -\ \frac{e^2}{\varepsilon_\infty}\ \wp\ P_{1s}(R)\int d\underline{s}\left[g_{+c}(s) - g_{-c}(s)\right]\frac{1}{|\underline{r}-\underline{s}|}. \tag{L.6}$$

After the integration over angles one gets

$$V_{out}^{(r)} = -\ \frac{4\pi e^2}{\varepsilon_\infty}\ \wp\ P_{1s}(R)\ \frac{1+\Gamma\bar{\sigma}}{1+\Gamma\sigma}\int_0^\infty ds\ s^2\ g_{++}(s)\ I(r,s) \tag{L.7}$$

where $\quad I(r,s) = \begin{cases} 2/s & \text{for } r < s \\ 2/r & \text{for } r > s \end{cases}.$

The relation between $g_{\pm c}$ and g_{++} within the MSA $[50]$ has been

used in deriving (L.7) . Using explicitly the function $I(r,s)$, (L.7) can be rewritten as follows

$$V_{out}^{(r)} = -\ \frac{8\pi e^2}{\varepsilon_\infty}\ \wp\ P_{1s}(R)\frac{1+\Gamma\bar{\sigma}}{1+\Gamma\sigma}\left[\frac{1}{r}\int_0^r ds\ s^2 g_{++}(s) + \int_r^\infty ds\ s\ g_{++}(s)\right]. \tag{L.8}$$

The integrations in (L.8) can be performed exactly by using the representation of g_{++} given by the MSA $[48]$. The final expression for $V_{out}(r)$ then reads

$$V_{out}^{(r)} = -\ \frac{V_0}{\varepsilon_\infty}\ \frac{1+\Gamma\bar{\sigma}}{\Gamma r}\ P_{1s}(R)\ \phi(n\bar{\sigma}) ,\quad \text{for } (n-1)\bar{\sigma} \leq (r-R) \leq n\bar{\sigma} \tag{L.9}$$

where $\quad \phi(n\bar{\sigma}) = 1 + \dfrac{e^{-\Gamma(r-n\bar{\sigma})}}{2}\sum_{i=1}^{n} x^{i-1}\left[\alpha_{n,i}\cos x + \beta_{n,i}\sin x\right]$

with $\quad x = \Gamma(r-n\bar{\sigma})$,while the quantities $\alpha_{n,i}$ and $\beta_{n,i}$ are given by $[48]$

$$\alpha_{n,i} = -2 , \qquad \beta_{n,1} + \alpha_{n,2} = -2$$

$$\left.\begin{array}{l}\beta_{n,i} + \dfrac{i}{2}\alpha_{n,i+1} = \alpha_{n-1,i-1}/(i-1)\\[2mm]\dfrac{i}{2}\beta_{n,i+1} - \alpha_{n,i} = \beta_{n-1,i-1}/(i-1)\end{array}\right\}2 \leq i \leq n-1, \tag{L.10}$$

$$\beta_{nn} = \alpha_{n-1,n-1}/(n-1) , \quad \alpha_{nn} = -\beta_{n-1,n-1}/(n-1).$$

Appendix M :

Calculated values for the solvated electron model in section (III.3)

The calculated values for the solvated electron model in section (III.3) are summarized in Tables (M.1-M.4) for molten NaCl , KCl , KBr and CsCl systems . In Fig.(M.1) are plotted the resulting values of (Eq.(III.3-15)) for CsCl . In the same figure is also plotted the least-square parabola which fits the numerical values of $\mu_e(R)$. In Fig.(M.2)
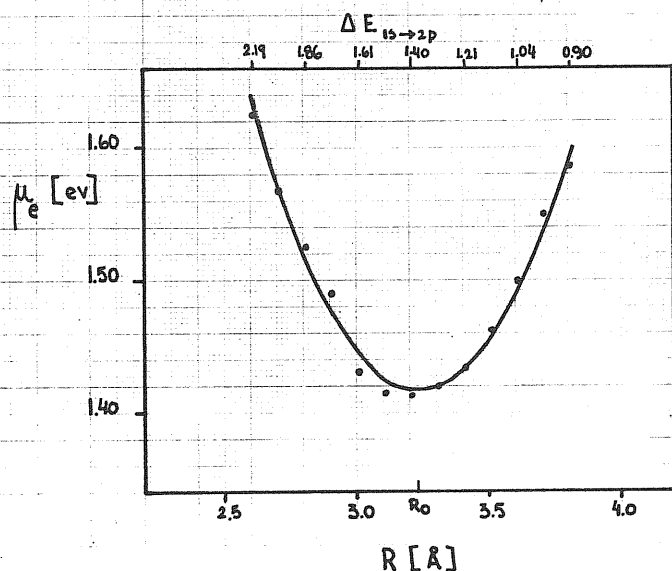
Figure M.1 : Chemical potential of the bubble for CsCl at T = 973 °K . The points are the calculated values of $\mu_e(R)$. The continuous parabola corresponds to a least-square fit.

is shown a similar fit for the square dipole matrix elements $|\Gamma_{1s \to 2p}|^2$ (Eq.(III.5-4)) . These fits , plus the corresponding one for the function $R(\omega)$,were used in Eq.(III.5-5) for the determination of the absorption intensity bands $I^0(\omega)$. This analytic representation for $I^0(\omega)$ allows a systematic calculation of the band parameters $R_0, \mu_e(R_0)$, ω_m and $\Delta\omega$, eliminating the random scattering of the numerical calculations . In Fig.(M.1) are also indicated the corresponding energies for the 1s $\longrightarrow$ 2p transition , showing that the whole range of such values needed for a complete determination of $I^0(\omega)$ (see Fig.(III.5-1)) is scanned by the numerical (and consequently by the least-square fit) results .
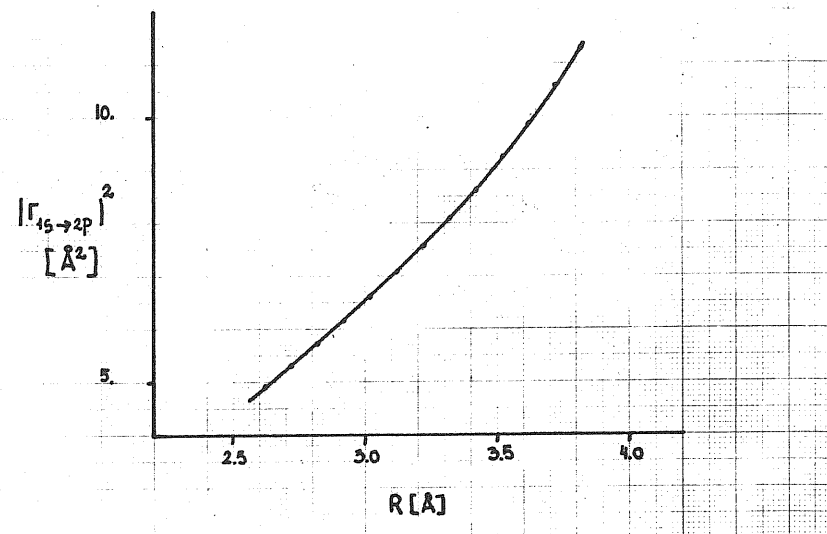
Figure M.2 : Dipole matrix elements for the 1s $\to$ 2p transition in CsCl at T = 973°K . The points are the calculated values of $|\Gamma_{1s \to 2p}|^2$. The continuous line corresponds to the least-square parabola .

(a)

R	$\mu_e(R)$	$|\Gamma_{1s\to2p}|^2$	$|\Gamma_{1s\to3p}|^2$	$\Delta E_{1s\to2p}$	$\Delta E_{1s\to3p}$
2.32	1.34	3.92	0.086	2.64	3.26
2.42	1.22	4.24	0.084	2.47	3.09
2.52	1.12	4.57	0.091	2.31	2.95
2.62	1.03	4.90	0.077	2.18	2.82
2.72	0.966	5.24	0.073	2.05	2.71
2.82	0.918	5.58	0.069	1.94	2.61
2.92	0.855	5.93	0.058	1.85	2.56
3.02	0.842	6.28	0.054	1.75	2.47
3.12	0.844	6.64	0.051	1.67	2.39
3.22	0.860	7.00	0.047	1.59	2.31
3.32	0.890	7.36	0.044	1.51	2.24
3.42	0.934	7.74	0.041	1.44	2.18
3.52	0.992	8.11	0.038	1.38	2.12

(b)

| R	$P_{1s}(R)$	$P_{r_{1s}}(R)$	$P_{2p}(R)$	$P_{r_{2p}}(R)$	$P_{3p}(R)$	$P_{r_{3p}}(R)$	$\langle r^2\rangle_{1s}$	$\langle r^2\rangle_{2p}$	$\langle r^2\rangle_{3p}$	$V(0)$	E_{1s}	E_{2p}	E_{3p}
2.32	0.744	0.090	0.345	0.186	0.021	0.084	4.20	13.0	206.	-6.74	-3.49	-.852	-.234
2.42	0.749	0.084	0.353	0.177	0.022	0.083	4.51	13.3	206.	-6.34	-3.33	-.861	-.235
2.52	0.755	0.080	0.373	0.169	0.022	0.082	4.82	13.5	206.	-6.00	-3.19	-.873	-.237
2.62	0.760	0.075	0.388	0.161	0.023	0.082	5.13	13.8	207.	-5.68	-3.06	-.885	-.239
2.72	0.765	0.071	0.403	0.153	0.023	0.081	5.45	14.1	208.	-5.40	-2.95	-.898	-.240
2.82	0.771	0.067	0.417	0.146	0.023	0.080	5.77	14.3	209.	-5.15	-2.85	-.911	-.242
2.92	0.781	0.062	0.445	0.136	0.023	0.081	6.09	14.2	206.	-4.96	-2.80	-.955	-.247
3.02	0.785	0.059	0.453	0.130	0.023	0.080	6.42	14.5	207.	-4.75	-2.72	-.963	-.248
3.12	0.790	0.056	0.471	0.124	0.024	0.079	6.77	14.9	208.	-4.56	-2.64	-.970	-.249
3.22	0.794	0.053	0.484	0.118	0.024	0.079	7.11	15.3	210.	-4.38	-2.56	-.977	-.250
3.32	0.799	0.051	0.496	0.113	0.024	0.078	7.47	15.6	211.	-4.22	-2.49	-.982	-.251
3.42	0.803	0.049	0.508	0.108	0.025	0.078	7.83	16.1	213.	-4.07	-2.43	-.987	-.252
3.52	0.807	0.046	0.519	0.103	0.025	0.077	8.20	16.5	215.	-3.93	-2.37	-.990	-.252

Table M.1 :   Optical absorption data for NaCl . (a) Chemical potential of the bubble $\mu_e(R)$ [ev] dipole matrix elements $|\Gamma_{ke}|^2$ [Å²] and transition energies ΔE_{ke} [ev] at different cavity radii R [Å] ; (b) parameters for the ground state and 2p and 3p excited states: $P_n(R)$, $P_{r_n}(R)$ [Å⁻¹], $\langle r^2\rangle_n$ [Å²], potential well depth $V(0)$ and eigenenergies E_n [ev] .

(a)

R	$\mu_e(R)$	$|\Gamma_{1s\to2p}|^2$	$|\Gamma_{1s\to3p}|^2$	$\Delta E_{1s\to2p}$	$\Delta E_{1s\to3p}$
2.46	1.45	4.58	0.086	2.31	2.95
2.56	1.37	4.94	0.094	2.15	2.76
2.66	1.30	5.32	0.100	2.00	2.60
2.76	1.25	5.71	0.105	1.87	2.45
2.86	1.21	6.11	0.110	1.75	2.32
2.96	1.18	6.52	0.113	1.64	2.20
3.06	1.13	6.94	0.102	1.56	2.14
3.16	1.13	7.37	0.105	1.47	2.04
3.26	1.13	7.82	0.106	1.39	1.95
3.36	1.15	8.28	0.108	1.32	1.86
3.46	1.18	8.75	0.109	1.25	1.79
3.56	1.22	9.23	0.110	1.18	1.71
3.66	1.28	9.73	0.111	1.13	1.65

(a)

R	$P_{1s}(R)$	$P_{r_{1s}}(R)$	$P_{2p}(R)$	$P_{r_{2p}}(R)$	$P_{3p}(R)$	$P_{r_{3p}}(R)$	$\langle r^2\rangle_{1s}$	$\langle r^2\rangle_{2p}$	$\langle r^2\rangle_{3p}$	$V(0)$	E_{1s}	E_{2p}	E_{3p}
2.46	0.734	0.088	0.352	0.178	0.023	0.085	4.82	13.5	196.	-6.03	-3.21	-.895	-.253
2.56	0.735	0.084	0.354	0.171	0.024	0.083	5.20	14.4	201.	-5.63	-3.01	-.868	-.250
2.66	0.736	0.081	0.357	0.164	0.025	0.082	5.59	15.3	207.	-5.28	-2.84	-.847	-.248
2.76	0.738	0.077	0.360	0.158	0.026	0.080	5.98	16.2	211.	-4.96	-2.70	-.830	-.246
2.86	0.740	0.074	0.365	0.152	0.027	0.079	6.39	17.0	216.	-4.68	-2.56	-.815	-.244
2.96	0.742	0.071	0.370	0.146	0.028	0.078	6.80	17.8	220.	-4.43	-2.45	-.803	-.243
3.06	0.751	0.067	0.390	0.139	0.029	0.078	7.18	17.9	219.	-4.25	-2.38	-.823	-.247
3.16	0.752	0.064	0.394	0.134	0.030	0.076	7.62	18.8	224.	-4.04	-2.28	-.810	-.245
3.26	0.754	0.062	0.399	0.129	0.031	0.075	8.06	19.6	228.	-3.85	-2.19	-.799	-.244
3.36	0.756	0.060	0.404	0.125	0.032	0.074	8.52	20.4	232.	-3.67	-2.11	-.788	-.242
3.46	0.758	0.057	0.409	0.121	0.033	0.073	8.98	21.2	236.	-3.51	-2.03	-.777	-.241
3.56	0.759	0.056	0.413	0.117	0.034	0.072	9.47	22.1	240.	-3.36	-1.95	-.766	-.239
3.66	0.761	0.054	0.417	0.114	0.034	0.072	9.96	22.9	245.	-3.22	-1.88	-.755	-.238

(b)

Table   M.2 : Optical absorption data for KCL. (same as in Table (M.1)).

M-5 Table (a):

R	$\mu_e(R)$	$|\Gamma_{1s\to2p}|^2$	$|\Gamma_{1s\to3p}|^2$	$\Delta E_{1s\to2p}$	$\Delta E_{1s\to3p}$
2.53	1.28	4.64	0.044	2.36	3.15
2.63	1.21	4.99	0.048	2.19	2.95
2.73	1.14	5.36	0.052	2.04	2.77
2.83	1.09	5.73	0.056	1.91	2.62
2.93	1.06	6.12	0.059	1.79	2.48
3.03	1.03	6.51	0.061	1.68	2.35
3.13	1.01	6.92	0.063	1.59	2.24
3.23	1.00	7.34	0.065	1.50	2.14
3.33	0.979	7.75	0.060	1.43	2.07
3.43	0.992	8.19	0.061	1.35	1.98
3.53	1.02	8.64	0.062	1.29	1.90
3.63	1.05	9.10	0.063	1.22	1.82
3.73	1.09	9.58	0.064	1.16	1.75

(a)

M-5 Table (b):

R	$P_{1s}(R)$	$P_{r_{1s}}(R)$	$P_{2p}(R)$	$P_{r_{2p}}(R)$	$P_{3p}(R)$	$P_{r_{3p}}(R)$	$\langle r^2\rangle_{1s}$	$\langle r^2\rangle_{2p}$	$\langle r^2\rangle_{3p}$	$V(0)$	E_{1s}	E_{2p}	E_{3p}
2.53	0.761	0.078	0.419	0.163	0.018	0.086	4.77	11.3	190.	-6.19	-3.40	-1.04	-.249
2.63	0.762	0.074	0.421	0.157	0.019	0.084	5.13	12.1	196.	-5.78	-3.19	-1.00	-.246
2.73	0.764	0.071	0.423	0.151	0.020	0.082	5.50	12.9	201.	-5.42	-3.01	-.970	-.244
2.83	0.765	0.068	0.426	0.145	0.021	0.081	5.88	13.7	206.	-5.11	-2.86	-.944	-.242
2.93	0.767	0.066	0.430	0.140	0.022	0.080	6.27	14.5	211.	-4.82	-2.72	-.922	-.240
3.03	0.769	0.063	0.434	0.135	0.023	0.079	6.67	15.3	215.	-4.57	-2.59	-.902	-.238
3.13	0.771	0.061	0.439	0.130	0.024	0.078	7.08	16.1	220.	-4.34	-2.48	-.885	-.236
3.23	0.773	0.058	0.443	0.125	0.025	0.077	7.49	16.8	224.	-4.13	-2.37	-.869	-.235
3.33	0.779	0.055	0.460	0.119	0.025	0.076	7.90	17.2	225.	-3.96	-2.31	-.880	-.237
3.43	0.781	0.053	0.464	0.115	0.026	0.075	8.33	18.0	229.	-3.78	-2.22	-.864	-.236
3.53	0.783	0.051	0.468	0.111	0.027	0.074	8.78	18.8	233.	-3.62	-2.14	-.850	-.234
3.63	0.784	0.049	0.472	0.107	0.028	0.073	9.24	19.6	238.	-3.46	-2.06	-.835	-.233
3.73	0.786	0.048	0.476	0.104	0.029	0.072	9.71	20.4	242.	-3.32	-1.98	-.822	-.231

(b)

Table M.3 : Optical absorption data for KBR. (same as in Table (M.1)).

M-6 Table (a):

R	$\mu_e(R)$	$|\Gamma_{1s\to2p}|^2$	$|\Gamma_{1s\to3p}|^2$	$\Delta E_{1s\to2p}$	$\Delta E_{1s\to3p}$
2.61	1.62	4.92	0.061	2.19	2.81
2.71	1.57	5.32	0.076	2.02	2.58
2.81	1.53	5.73	0.091	1.86	2.38
2.91	1.49	6.16	0.109	1.72	2.21
3.01	1.43	6.61	0.110	1.61	2.10
3.11	1.42	7.08	0.129	1.50	1.95
3.21	1.41	7.58	0.151	1.40	1.81
3.31	1.42	8.10	0.176	1.30	1.69
3.41	1.44	8.60	0.206	1.21	1.57
3.51	1.46	9.25	0.244	1.12	1.46
3.61	1.50	9.88	0.295	1.04	1.35
3.71	1.55	10.6	0.368	0.958	1.23
3.81	1.58	11.3	0.394	0.899	1.17

(a)

M-6 Table (b):

R	$P_{1s}(R)$	$P_{r_{1s}}(R)$	$P_{2p}(R)$	$P_{r_{2p}}(R)$	$P_{3p}(R)$	$P_{r_{3p}}(R)$	$\langle r^2\rangle_{1s}$	$\langle r^2\rangle_{2p}$	$\langle r^2\rangle_{3p}$	$V(0)$	E_{1s}	E_{2p}	E_{3p}
2.61	0.755	0.077	0.394	0.162	0.017	0.078	5.12	13.2	232.	-5.63	-3.01	-.819	-.198
2.71	0.752	0.075	0.385	0.157	0.019	0.076	5.55	14.7	243.	-5.20	-2.78	-.762	-.193
2.81	0.750	0.073	0.376	0.152	0.021	0.074	6.01	16.3	254.	-4.82	-2.57	-.712	-.189
2.91	0.747	0.071	0.368	0.148	0.023	0.072	6.46	17.9	265.	-4.48	-2.39	-.669	-.184
3.01	0.751	0.068	0.378	0.142	0.023	0.072	6.92	18.6	268.	-4.23	-2.28	-.666	-.184
3.11	0.748	0.066	0.369	0.138	0.025	0.070	7.44	20.4	279.	-3.95	-2.13	-.629	-.180
3.21	0.745	0.065	0.360	0.135	0.027	0.068	7.98	22.3	291.	-3.69	-1.99	-.594	-.175
3.31	0.741	0.064	0.351	0.132	0.028	0.067	8.57	24.4	304.	-3.45	-1.86	-.561	-.171
3.41	0.737	0.063	0.339	0.129	0.030	0.065	8.19	26.8	317.	-3.23	-1.74	-.528	-.166
3.51	0.731	0.062	0.326	0.127	0.032	0.063	9.87	29.5	332.	-3.02	-1.62	-.496	-.161
3.61	0.724	0.062	0.310	0.124	0.033	0.062	10.6	32.9	350.	-2.81	-1.50	-.462	-.155
3.71	0.714	0.062	0.288	0.122	0.035	0.060	11.5	37.4	372.	-2.60	-1.38	-.424	-.147
3.81	0.713	0.060	0.287	0.119	0.036	0.059	12.2	39.5	382.	-2.46	-1.31	-.413	-.145

(b)

Table M.4 : Optical absorption data for CsCl (same as in Table (M.1)).

Appendix N :

NMR   experiments in molten salt

(a) The orthogonalized wave function of the F-center electron.

Within a point-like ion model for the F-center one calculates a smooth electronic wave function Ψ_F (often called the envelope wave function). In hyperfine structure calculations , however , a detailed nature of the F-electron wave function at the nucleus of the ions is required . It was shown [131] that this function may be constructed by orthogonalizing the envelope function to the ion core orbitals . The problem is then one of calculating overlap integrals . The orthogonalization of Ψ_F to the core electrons , Ψ_i , of the jth ion by the Schmidt orthogonalization procedure , where only the first nonvanishing term is kept in an expansion of Ψ_F about the jth ion , gives :

$$\emptyset_F(j) = N\left(\Psi_F(j) - \sum_i \Psi_i \langle \Psi_i | \Psi_F(j)\rangle\right) \simeq N\left(\Psi_F(j) - \sum_i \Psi_i \Psi_F(j) \int \Psi_i \, d\zeta \right) \quad (N.1)$$

which can be rewritten as

$$\emptyset_F^2(j) \simeq | N(1 - \sum_i \Psi_i \int \Psi_i \, d\zeta) \Psi_F(j)|^2 = A_j | \Psi_F(j)|^2 . \quad (N.2)$$

The quantity A_j is an 'amplification' factor which accounts for the larger electric charge the F-electron sees at the nucleus of the surrounding

j^{th} ion . It turns out that A_j roughly depends only on the charge Z of the jth ion . Values of A_j can be estimated from the experimental values for $\emptyset_F^2(j)$ and from the point-like calculations of $\Psi_F^2(j)$. This has been done for a few alkali halide crystals [133] , where was found that

$$A_+(Z) \simeq 4.0 \; Z^{1.5}$$

$$A_-(Z) \simeq 3.4 \; Z^{1.9} \quad\quad (N.3)$$

for the first two shells of surrounding ions . These calculations were repeated here for some alkali halide crystals . The results are plotted in Fig.(N.1) . The present estimations of $A_+(Z)$ are compared with those of Eq.(N.3) in Table (N.1) .

Z	A_+ (Fig.(N.1))	A_+ (Eq.(N.3))
Li ^{3}	23 .	21.
Na ^{11}	149.	146.
K ^{19}	428.	331.
Rb ^{37}	1073.	900.
Cs ^{55}	1400.	1632.

Table N.1 : Comparison between A_+ as given from Fig.(N.1) and by Eq.(N.3) .
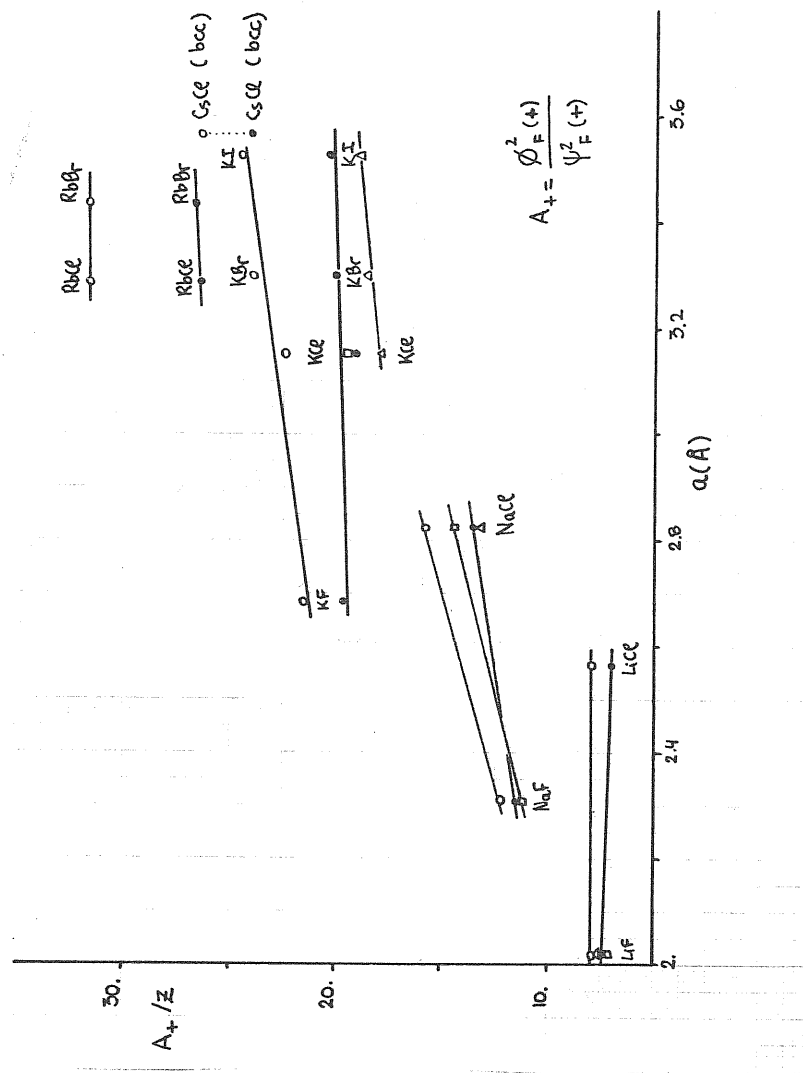
Figure N.1 :   Amplification factor A_+ for some alkali halides.

a is the lattice constant. ($\bullet$) from [138] , ($\circ$) [139] , ($\triangle$) [140] , ($\square$) [141] .

(b) Experimental values of ϕ_F^2 in a molten salt.

Values of ϕ_F^2 for molten Cs–CsCl have been obtained in NMR experiments [116] . It was found for the average hyperfine coupling $\langle |\phi_F(\omega)|^2 \rangle$ a value

$$\langle |\phi_F(\omega)|^2 \rangle_{exp} \simeq 0.26 \, |\phi(\omega)|^2_{atom} \, . \qquad (N.4)$$

The value for $\phi^2(\omega)$ in the atom can be obtained from the hyperfine splitting $\Delta \nu$ measurements [118] ,

$$\Delta \nu = \frac{2}{3} \, \frac{2I+1}{I} \, \mu_m \, \frac{m_e}{m_p} \, \alpha^2 \, \frac{R_y}{\hbar} \, \phi^2(0) \, a_B^3 \, , \qquad (N.5)$$

where I and μ_m are the nuclear spin and nuclear magnetic moment, respectively . For Cs^{55} one has : $\Delta \nu$ = 9197.6 10^6 sec^{-1} , I = 7/2 and μ_n = 2.57 (nuclear magneton units) . The resulting value for $\phi^2(\omega)$ is : $\phi^2(\omega) \simeq 27. \, \text{Å}^{-3}$. To determine the average value of $|\phi_F(\omega)|^2$ in molten Cs–CsCl , the number n_F of positive ions surrounding the solvated electrons is required . If one takes $n_F \approx 4 \div 5$, then

$$\langle |\phi_F(\omega)|^2 \rangle_{exp} \simeq \frac{0.26}{n_F} |\phi(\omega)|^2_{atom} \approx 1.56 \, \text{Å}^{-3} \qquad (N.6)$$

Analogously , a value for $\langle |\phi_F(Cl)|^2 \rangle_{exp} \approx 0.023 \, \text{Å}^{-3}$ [116] is obtained.

Theoretical estimations for these quantities can be obtained from values

of $\psi_F(t)$ in Table (III.4-2) and $A_\pm$ from Eq.(N.3) . These values

are in order-of-magnitude-agreement with the experimental results .

Appendix P :

The charge transfer model for the β exciton in molten salts $(CsC\ell)$

(a) Electrostatic and repulsive energy contributions.

A model for the exciton in a molten salt can be schematically repre-
sented as a charge transfer show in the figure .

(a) free exciton   (b) β exciton
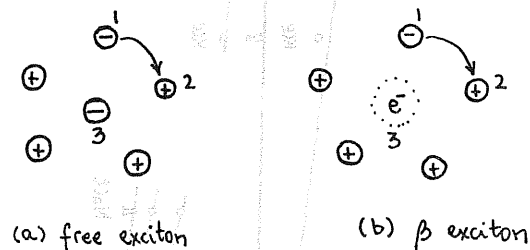
The electrostatic energies required to extract ions (1) and (2) in the

process (a) and (b) are

$$E_e^{(a)} = \frac{e^2}{r_{13}} - \frac{e^2}{r_{23}}$$

$$E_e^{(b)} = \frac{e^2}{r_{13}} - \frac{e^2}{r_{23}} f\left(P_{1S}(r_{23}) \right) ,$$

(P.1)

where $f(P_0(r)) = P_0(r) + r\, P_{r_0}(r)$ is obtained by calculating

$\int \dfrac{|\psi_{1s}(r')|^2}{|\vec{r}-\vec{r}'|} d\tau'$ the potential at position $\vec{r}$ due to the electronic charge distribution $|\psi_{1s}(r')|^2$. The electrostatic contribution to $\Delta \nu$ in Eq.(III.7-1) is therefore

$$\Delta E_c = E_e^{(b)} - E_e^{(a)} \simeq + 0.164 \; eV \; ,\qquad (P.2)$$

where $\quad r_{23} = r_{+-} = 3.38 \, \AA \quad [136] \; , \quad P_{1s}(r_{23}) \approx P_{1s}(R_0 = 3.23 \, \AA) = .745$ and $P'_{r_{1s}}(r_{23}) \approx P'_{r_{1s}}(R_0) = 0.064 \, \AA^{-1}$ were used in Eq.(P.1) .

The repulsive contribution to $\Delta \nu$ can be estimated from the corresponding expressions given by the Born model [2] to be

$$W_{+-}(r_{23}) \simeq b \; e^{(r_+ + r_- - r_{23})/\rho} = 0.067 \; eV, \qquad (P.3)$$

where $\quad r_+ = 1.56 \, \AA \quad , \quad r_- = 1.44 \, \AA \quad [49] \; , \quad \rho = .33 \, \AA \quad$ and $\; b = .211 \, eV \, [2] \; .$

(b) The geometric factor g in molten salts.

According to the charge transfer model [30] , the geometric factor is written as

$$g(r_{23}, r_{13}, \alpha) = \frac{1}{(r_{13}/r_{23})^4} + 1 \; - \; \frac{2 \cos\alpha}{(r_{13}/r_{23})^2} \; , \qquad (P.4)$$

where $\quad \alpha$ is the angle between $(\hat{r}_{13}, \hat{r}_{23})$. In the liquid , α ,as

well as the distances r_{13}, r_{23} , are determined by a three body correlation function . If one assumes the most probable distances between the three ions , with the condition that r_{12} and r_{23} being nearest neighbor distances , the following expression for g is obtained ,

$$g = 1 - (r_{+-}/r_{--}) + (r_{+-}/r_{--})^4 \; . \qquad (P.5)$$

In this particular case , it turns out that $g \approx 0.7$, where $r_{--} = 3.85 \, \AA \; [136].$

REFERENCES:

1. M. Born, 'Atomtheorie des festen Zustandes' (Teubner, Leipzig and Berlin, 1923).

2. M. P. Tosi, Solid State Phys. 16, 1 (Academic Press, New York , 1964).

3. H. Witte and E Wölfel, Rev. Mod. Phys. 30, 51 (1958).

4. E. Madelung, Physik. Z. 19, 524 (1918); P. P. Ewald, Ann. Physik (4), 64, 253 (1921).

5. F. G. Fumi and M. P. Tosi, Phys. Rev. 117, 1466 (1960).

6. M. P. Tosi and F. G. Fumi, J. Phys. Chem. Solids 25, 45 (1964).
M. L. Huggins and J. E. Mayer, J. Chem. Phys. 1, 643 (1933).

7. R. Shuttleworth, Proc. Phys. Soc. (LONDON) A62, 167 (1949).

8. F. London, Z. Phys. Chem. B11, 222 (1930) and Trans. Faraday Soc. 33, 8 (1937).

9. J. E. Mayer, J Chem. Phys. 1, 270 (1933).

10. M. L. Huggins and Y. Sakamoto, J. Phys. Soc. Japan 12, 241 (1957).

11. G. C. Benson and E. Dempsey, Proc. Roy. Soc. (London) A266, 344 (1962).

12. A. B. D. Wood, W. Cochran and B. N. Brockhouse, Phys. Rev. 119, 980 (1960); B. N. Brockhouse, R. Cowley, A. B. D. Woods and W. Cochran, Phys. Rev. 131, 1025 (1963).

13. H. B. Huntington, Solid State Physics 7 (Academic Press, New York, 1958).

14. H. E. Hite and R. J. Kearney, J. Appl. Phys. 38, 5424 (1967).

15. W. Hayes and A. M. Stoneham, ' Crystals with the Fluorite Structure Ed. W. Hayes (Clarendon Press, Oxford, 1974).

16. See, e. g., P. Brüesch, 'Phonons: Theory and Experiments I' (Springer-Verlag, Berlin, 1982).

17. R. P. Lowndes and D. H. Martin, Proc. Roy. Soc. A308, 473 (1969).

18. C. R. A. Catlow, Comments Sol. State Phys. 9, 157 (1978-1980).

19. J. R. Hardy and A. M. Karo, 'The Lattice Dynamics and Statics of Alkali Halide Crystals' (Plenum Press, New York, 1969).

20. H. W. Etzel and R. J. Maurer, J. Chem. Phys. 18, 1003 (1950).

21. J. Bardeen and C. Herring, ' Imperfections in Nearly Perfect Crystals' (Wiley, New York, 1952).

22. F. Seitz, Rev. Mod. Phys. 26, 7 (1954).

23. F. C. Brown, 'The Physics of Solids' (W. A. Benjamin, New York, 1966).

24. A. Smakula, Z. Physik 59, 603 (1930); see also, J. J. Markham , 'F- centers in Alkali Halides' (Academic Press, New York, 1966).

25. for a generalization of Smakula's equation see: D. Y. Smith and G. Graham, J. Physique Colloq. 41, C6-80 (1980).

26. A. J. Dekker, 'Solid State Physics' (Prentice-Hall, Englewood Cliffs, N. Y., 1962).

27. See, e.g., G. Iadonisi and B. Preziosi, Nuovo Cimento B48, 92 (1967).

28. C. C. Klick and M. N. Klaber, Phys. Rev. 131, 1075 (1963).

29. C. J. Delbecq, P. Pringsheim and P. H. Yuster, J. Chem. Phys. 19, 574 (1951).

30. F. Bassani and N. Inchauspé, Phys. Rev. 105, 819 (1957).

31. D. L. Dexter, Phys. Rev. 83, 1044 (1951).

32. H. Reiss, S. W. Mayer and J. L. Katz, J. Chem. Phys. 35, 820 (1961).

33. N. H. March and M. P. Tosi, 'Coulomb Liquids' (Academic Press, in the course of publication).

34. L. Pietronero, Phys. rev. B17, 3946 (1978).

35. H. Ohmo and K. Furukawa, J. Chem. Soc. Faraday Trans. I77, 1981 (1981).

36. S. Biggin and J.E. Enderby, J. Phys. C15, L305 (1982).

37. E. W.J. Mitchell, P.F.J. Poncet and R.J. Stewart, Phil. Mag. 34, 721 (1976).

38. J. Forland, in 'Fused Salts' (Mc Graw-Hill, New York, 1964).

39. D. J. Adams and I. R. Mc Donald, J. Phys. C., 7, 2761 (1964).

40. J. E. Eby, K. J. Teegarden and D.B. Dutton, Phys. Rev. 116, 1099 (1959).

41. C. D. Clark, A. H. Skull and J. S. Wells, in 'Color Center Conference', (Gatlimburg, 1978).

42. M. Parrinello and M. P. Tosi, Riv. Nuovo Cimento, 2, N.6 (1979).

43. M. S. Werthheim, Phys. Rev. Lett. 10, 321 (1963). E. Thiele, J. Chem. Phys. , 39, 474 (1963).

44. B. Larsen, G. Stell and K. C. Wu, J. Chem. Phys. $\underline{67}$, 530 (1977).

45. J. S. Hoje and G. Stell, J. Chem. Phys. $\underline{67}$, 524 (1977).

46. G. Stell and S. F. Sun, J. Chem. Phys. $\underline{63}$, 5333 (1975).

47. D. Henderson and W. R. Smith, J. Stat. Phys. $\underline{19}$, 191 (1978).

48. C. W. Outhwaite and V. C. L. Hutson, Molec. Phys. $\underline{29}$, 1521 (1975).

49. M. C. Abramo, C. Caccamo, G. Pizzimenti, M. Parrinello and M. P. Tosi, J. Chem. Phys. $\underline{68}$, 2889 (1978).

50. E. Weismann and J. L. Lebowitz, J. Chem. Phys. $\underline{52}$, 4307 (1970), $\underline{56}$, 3086 (1972). L. Blum and J. S. Hoje, J. Phys. Chem. $\underline{81}$, 1311(1977).

51. R. Shuttleworth, Proc. Phys. Soc. A $\underline{63}$, 444 (1950).

52. J. W. Gibbs, 'Collected Works', Vol.1 , Longmans, Green, New York, 1931.

53. A. W. Adamson, 'Physical Chemistry of Surfaces' (Interscience Publishers, New York, 1967).

54. See e.g., R. G. Linford, in Solid State Surface Science, Ed. M.Green (Dekker, New York, 1973), Vol.2.

55. G. C. Benson and K. S. Yun, in The Solid Gas Interface, Ed. E. Alison Flood (Dekker, New York 1967).

56. V. D. Kuznetsov, in 'Surface Energy of Solids', Departement of Scientific and Industrial Research, (London, 1957).

57. J.J. Gilman, J. Appl. Phys. $\underline{31}$, 2208 (1960).

58. A. R. C. Westwood and T. T. Hitch, J. Appl. Phys. $\underline{34}$, 3085 (1963).

59. S. G. Lipsett, F. M. G. Johnson and o; Maass, J. Am. Chem. Soc. $\underline{49}$, 925 (1927).

60. W. Ostwald, Z. Phys. Chem. (Leipzig) $\underline{34}$, 495 (1900). See also L. Harburg, J. Phys. Chem. $\underline{50}$, 190 (1946).

61. R. R. Weiler, J. Beeckmans and R. Mc Intosh, Can. J. Chem. $\underline{39}$, 1360 (1961).

62. G. Jura and C. W. Garland, J. Am. Chem. Soc. $\underline{74}$, 6033 (1952).

63. W. Kohn and A. Yaniv, Phys. Rev. $\underline{B20}$, 4948 (1979).

64. H. Bilz and W. Kress, 'Phonon Dispersion Relations in Insulators', (Springer-Verlag, Berlin 1979).

65. E. Roman, G. Senatore and M. P. Tosi, J. Phys. Chem. Solids $\underline{43}$, 1093 (1982).

66. J. Tessman, A. Kahn and W. Shockley, Phys. Rev. $\underline{92}$, 890 (1953).

67. C. Kittel, 'Introduction to Solid State Physics' (Wiley, New York 1967), Third Edition.

68. M. Born and K. Huang, 'Dynamical Theory of Crystal Lattices' (Clarendon Press, Oxford 1954).

69. American Institute of Physics Handbook (Mc Graw-Hill, New York 1972), Third Edition.

70. M. L. Cohen and V. Heine, in 'Solid State Physics', Eds. F. Seitz D. Turnbull and H. Ehrenreich (Academic Press, New York 1970), Vol.24.

71. J. W. Hodby, in 'Crystals with the Fluorite Structure', Ed. W.Hayes (Clarendon Press, Oxford 1974).

72. Handbook of Physics (Mc Graw-Hill, New York 1967), Second Edition.

73. K. S. Singwi and M. P. Tosi, Phys. Rev. $\underline{B23}$, 1640 (1981).

74. M. A. Bredig, in 'Molten Salt Chemistry', ed. M. Blander (Interscience, New York, 1964), p.367.

75. J. W. Johnson and M. A. Bredig, J. Phys. Chem. $\underline{62}$, 604 (1958).

76. M. A. Bredig and H.R. Bronstein, J. Phys. Chem. $\underline{64}$, 64 (1960).

77. M. A. Bredig, J. W. Johnson and W. T. Smith, J. Am. Chem. Soc. $\underline{77}$, 307 (1955).

78. H. R. Bronstein and M. A. Bredig, J. Am. Chem. Soc. $\underline{80}$, 2077 (1958).

79. A. S. Dworkin, H. R. Bronstein and M. A. Bredig, J. Phys. Chem. $\underline{66}$, 572 (1962).

80. M.A.Bredig, H. R. Bronstein and W. T. Smith, J. Am. Chem. Soc. $\underline{77}$, 1454 (1955).

81. H. R. Bronstein and M. A. Bredig, J. Phys. Chem. $\underline{65}$, 1220 (1961). H. R. Bronstein, A. S. Dworkin and M. A. Bredig, J. Chem. Phys. $\underline{37}$, 677 (1962).

82. E. Mollwo, Z. Phys. $\underline{85}$, 56 (1933).

83. J. P. Young, J. Phys. Chem. $\underline{67}$, 2507 (1963).

84. J. F. Rounsaville and J. J. Lagowski, J. Phys. Chem. $\underline{72}$, 1111(1968).

85. D. M. Gruen, M. Krumpelt and I. Johnson, in 'Molten Salt', ed. G. Mamontov (Marcel Dekker, New York, 1969), p.169.

86. I. E. Makarov, T. N. Zhukova and A. K. Pikaev, Red. Eff. $\underline{22}$, 71(1974).

87. W.Schmitt and U. Schindewolf, Ber. Bunsenges. Phys. Chem. 81, 584 (1977).

88. J. Greenberg and I. Warshawsky, J. Am. Chem. Soc. 86, 3572 (1964); 86, 5351 (1964).

89. S. J. Black and D. M. J. Compton, J. Phys. Chem. 69, 4421 (1965).

90. S. V. Volkov and V. S. Naumov, Ukr. Khim. Zh. 46, 794 (1980).

91. N. H. Nachtrieb, C. Hsu, M. Sosis and P. A. Bertrand, in 'Molten Salts', (The Electrochemical Society, Inc., Princeton, N.J.,1976).

92. M. Bettman, J. Chem. Phys. 44, 3254 (1966).

93. R. H. Arendt and N. H. Nachtrieb, J. Chem. Phys. 53, 3085 (1970).

94. R. L. McGraw, 'Thermodynamic Measurements on Metal-Molten Salt System' (Ph.D. Dissertation, University of Chicago, 1979).

95. C. Hsu and N. H. Nachtrieb, submitted to J. Phys. Chem.

96. H. Yokokawa and O. J. Kleppa, J. Chem. Phys. 76, 5574 (1982).

97. H. Yokokawa, O. J. Kleppa and N. H. Nachtrieb, J. Chem. Phys. 71, 4099 (1979).

98. E. G. Wilson, Phys. Rev. Lett. 10, 432 (1963).

99. M. Shimoji and K. Ichikawa, Phys. Lett. 20, 480 (1966). K. Ichikawa and M. Shimoji, Trans. Faraday Soc. 62, 3543 (1966).

100. N. H. Nachtrieb, Adv. Chem. Phys. 31, 465 (1975).

101. S. A. Rice, Discuss. Faraday Soc. 32, 181 (1961).

102. I. Katz and S. A. Rice, J. Am. Chem. Soc. 94, 4824 (1972).

103. P. W. Anderson, Phys. Rev. 109, 1432 (1958).

104 K. S. Pitzer, J. Am.Chem. Soc. 84, 2025 (1962).

105. M. E. Melnichak and O. J. Kleppa, J. Chem. Phys. 57, 5231 (1972).

106. E. Mollwo, Nachr. Ges. Wiss. Göttingen, 1, 203 (1935). See also 82 .

107. P. J. Durham and D. A. Greenwood, Phil. Mag. 33, 427 (1976).

108. P. A. Bertrand, 'Electron Paramagnetic Resonance and Magnetic Susceptibility of Molten Cs-CsCl Solutions' (Ph.D. Dissertation, University of Chicago, 1978).

109. H. J. Yuh, 'Optical spectroscopic studies of solvated electrons in CsCl melts' (Ph.D. Dissertation, University of Chicago, 1981).

110. W. Freyland, K. Garbade, H. Heyer and E. Pfeiffer, J. Phys. Chem. (Submitted).

111. F.-Y. Jou and G. R. Freeman, Can. J. Chem. 57, 591 (1979).

112. W. Freyland, K. Garbade and E. Pfeiffer, to be published.

113. M. Capizzi, G. A. Thomas, F. DeRosa, R. N. Bhatt and T. M. Rice, Sol. State Commun. 31, 611 (1979).

114. E. Roman and N. Majlis, Solid State Commun. 47, 259 (1983).

115. S. Sotier and W. W. Warren, Jr., J. Phys. (Orsay, Fr.) 41, C8, 40 (1980).

116. W. W. Warren,Jr and S. Sotier, in 'Proceedings of the Electrochemical Society Meeting', (Hollywood, FL, 1980).

117. See, for example, A. Abragam, 'Principles of Nuclear Magnetism' (Oxford, London,1961).

118. P. Kusch and H. Taub, Phys. Rev. 75, 1477 (1949).

119. H. Seidel and H. C. Wolf, in 'Physics of Color Centers', (ed. W. B. Fowler, Academic Press, New York, 1968).

120. N.Nicoloso and W. Freyland , J. Phys. Chem. 87, 1997 (1983).

121. N.Nicoloso and W. Freyland, Zs. Physik. Chem., (1983), in press.

122. G. Senatore, M. Parrinello and M. P. Tosi, Phil. Mag. B41, 595 (1980).

123. D. Schmid, Phys. Status Solidi 18, 653 (1966).

124. A. H. Kahn and C. Kittel, Phys. Rev. 89, 315 (1953).

125. A. Carrington and A. D. McLachlan, in 'Introduction to Magnetic Resonance' (Harper and Row, New York, 1967).

126. E. Roman, G. Senatore and M. P. Tosi, (ICTP Preprint, IC/83/157) Nuovo Cimento D (in press).

127. R. Herman, M. C. Wallis and R. F. Wallis, Phys. Rev. 103, 87 (1956).

128. M. Parrinello and A. Rahman, J. Chem. Phys. (in press).

129. A. D. Graves, J. Electroanal. Chem. 25, 349 and 357 (1970).

130. A. T. Kai, J. Phys. Chem. Solids, 42, 41 (1981). See also: N. Rösch, in 'Electrons in Finite and Infinite Structures', (Edited by P. Pharisean and L. Scheise) p.1. NATO Adv. Study Inst. Series B24. Plenum Press, New York (1977).

131. B. S. Gourary and F. J. Adrian, Solid State Phys. 10, 127 (ed. F. Seitz and D. Turnbull; Academic Press, New York 1960).

132.   G. J. Janz, 'Molten Salt Handbook' (Academic Press, New York 1967).

133.   W. C. Holton and H. Blum, Phys. Rev. 125, 89 (1962).

134.   W. B. Fowler, in 'Physics of Color Centers' (ed. by W. B. Fowler, Academic Press, New York and London, 1968).

135.   R. K. Swank and F. C. Brown, Phys. Rev. 130, 34 (1963). See also, C. H. Leung and K. S. Song, Solid State Commun. 33, 907 (1980).

136.   J. Y. Derrien and J. Dupuy, J. Physique 36, 191 (1975).

137.   N. F. Mott and M. J. Littleton, Trans. Faraday Soc. 34, 485 (1938).

138.   F. Dochy, Phys. Stat. Sol. (B) 93, 325 (1979).

139.   W. Renn   , Phys. Cond. Matter 17, 233 (1974).

140.   J. Schmid, Phys. Cond. Matter 15, 119 (1972).

141.   B. S. Gourary and F. J. Adrian, Phys. Rev. 105, 1180 (1957).